

**ADVANCED PIEZOELECTRIC TRANSDUCTION FOR ACOUSTIC SENSING
AND DATA TRANSMISSION**

A Dissertation
Presented to
The Academic Faculty

By

Romain Gerbe

In Partial Fulfillment
of the Requirements for the Degree
Doctor of Philosophy in the
School of Mechanical Engineering

Georgia Institute of Technology

December 2020

Copyright © Romain Gerbe 2020

**ADVANCED PIEZOELECTRIC TRANSDUCTION FOR ACOUSTIC SENSING
AND DATA TRANSMISSION**

Approved by:

Dr. Massimo Ruzzene, Advisor
School of Aerospace Engineering
Georgia Institute of Technology

Dr. Alper Erturk
School of Mechanical Engineering
Georgia Institute of Technology

Dr. Karim Sabra
School of Mechanical Engineering
Georgia Institute of Technology

Dr. Claudio V. Di Leo
School of Aerospace Engineering
Georgia Institute of Technology

Dr. Ihab El-kady
Sandia National Laboratories

Date Approved: September 25,
2020

ACKNOWLEDGEMENTS

I would like to express my appreciation to my advisor, Dr. Massimo Ruzzene, for his guidance and advising during these years while encouraging my research.

I would also like to thank Dr. Alper Erturk, Dr. Karim Sabra, Dr. Claudio Di Leo and Dr. Ihab El-kady for agreeing to serve as my committee members and for their insights that helped me complete this thesis.

I am especially grateful towards Dr. Karim Sabra for his help during the redaction of this dissertation. A special thanks goes towards Dr. Alper Erturk, Dr. Ihab El-kady and Dr. Charles M. Reinke for their support during the last two years and their guidance that helped me to stay on the right track.

TABLE OF CONTENTS

Acknowledgments	iii
List of Tables	ix
List of Figures	x
Summary	xvi
Chapter 1: Introduction	1
1.1 Overview	1
1.2 Background	2
1.2.1 Two-dimensional strain sensing	2
1.2.2 Acoustic data transmission across a barrier	7
1.3 Motivations and objectives	11
1.3.1 Two-dimensional strain sensing	11
1.3.2 Acoustic data transmission across a barrier	12
1.4 Contributions	13
1.5 Organization of the thesis	13
Chapter 2: Design of the Acoustic Wave Rosette	15
2.1 Overview	15

2.2	SAW device for 1D strain sensing	16
2.2.1	Introduction to Interdigital Transducers	16
2.2.2	Introduction to 1D strain measurement	18
2.2.3	Influence of the strain on the SAW velocity	20
2.2.4	Example	31
2.3	SAW device for 2D strain sensing	35
2.3.1	Introduction to bi-dimensional strain sensing	35
2.3.2	Design procedure of the Acoustic Wave Rosette	36
2.3.3	Strain measurements	40
2.3.4	Example	44
2.4	Conclusion	45
Chapter 3: Strain sensor manufacturing and testing		47
3.1	Overview	47
3.2	Material and design selections in 1D	47
3.3	Manufacturing	49
3.3.1	Introduction to microfabrication and photolithography	49
3.3.2	Manufacturing steps	51
3.3.3	Manufactured 1D device	54
3.4	Characterization of the 1D device	54
3.4.1	Experimental setup	54
3.4.2	Experimental frequency filtering capabilities	56
3.4.3	Experimental relation Frequency/Strain	59

3.5	Extension to the 2D device	59
3.5.1	Manufactured device	61
3.5.2	Experimental frequency filtering capabilities	61
3.5.3	Experimental relations Frequency/Strain	62
3.6	Conclusion	64
Chapter 4: Characterization of the acoustic data transmission by piezoelectric transduction		65
4.1	Overview	65
4.2	Description of the electro-mechanical behavior in the frequency domain	65
4.2.1	Structure for data transmission	66
4.2.2	Derivation of an analytical rod model	67
4.2.3	Comparison with finite elements results	73
4.2.4	Mason model	76
4.3	Experimental validation of the analytical rod model	83
4.3.1	Setup and configuration	83
4.3.2	Results for configurations with conductive epoxy bonding layers	83
4.3.3	Results for configurations with vacuum grease bonding layers	85
4.3.4	Results for configurations with solder patches bonding layers	87
4.4	Influence of the bonding layer on the resonances	88
4.4.1	Cases of the epoxy and solder bonding layers	88
4.4.2	Cases of intermediate bonding layers	89
4.5	Conclusion	90

Chapter 5: Wideband acoustic data transmission by piezoelectric transduction	92
5.1 Overview	92
5.2 Limitations of the quality of data transmissions for undamped structures	92
5.3 Reduction of the amplitude variations through backing layers	94
5.3.1 Introduction of backing layers	94
5.3.2 Combination of backing layers and additional electroplated layers	97
5.4 Reduction of the amplitude variations through an electric impedance in a load circuit	100
5.4.1 Introduction of an electric load impedance	100
5.4.2 Combination of an electric load impedance and backing layers	103
5.4.3 Combination of an electric load impedance, backing layers and electroplated layers	104
5.5 Combination of electric impedances on both the actuating and receiving circuits	106
5.6 Conclusion	108
Chapter 6: Wideband acoustic data transmission at high frequencies through staircase piezoelectric transducers	110
6.1 Overview	110
6.2 Wide bandwidth at high frequency	110
6.3 Angled and staircase transducers	112
6.4 Analytical expression of the output	115
6.4.1 Extension of the Mason model	115
6.4.2 Derivation of an analytical expression through Fourier Transform considerations	123
6.5 Strategies for bandwidth enhancements	129

6.5.1	Thickness offsetting between the actuator and the receiver	129
6.5.2	Capacitance compensation with electric impedances	131
6.6	Conclusion	133
Chapter 7: Conclusions and Future work		134
7.1	Summary	134
7.1.1	Acoustic Wave Rosette	134
7.1.2	Acoustic data transmission through a metallic barrier	135
7.2	Contributions	136
7.2.1	Acoustic Wave Rosette	136
7.2.2	Acoustic data transmission through a metallic barrier	136
7.3	Future work	137
7.3.1	Acoustic Wave Rosette	137
7.3.2	Acoustic data transmission through a metallic barrier	137
References		144

LIST OF TABLES

2.1	Table describing a configuration for an ZnO/SiO ₂ SAW strain sensor	29
2.2	Table describing a configuration for an ZnO/Flexible glass SAW strain sensor	33
2.3	Table describing a configuration for an ZnO/Flexible glass SAW 2D strain sensor	44
5.1	Configuration of the channel with backing and two electroplated layers . . .	100
5.2	Configuration of the channel with an electric load impedance	102
5.3	Configuration of the channel with backing and an electric load impedance .	104
5.4	Configuration of the channel with backing, electroplated layers and an electric load impedance	105
5.5	Configuration of the channel with loaded backing and electric actuating and load impedances	107
5.6	Configuration of the channel with unloaded backing and electric actuating and load impedances	108
6.1	Configuration of the channel with staircase transducers, thickness offsets and electric impedances	133

LIST OF FIGURES

1.1	Qualitative schematic of the displacement field associated to Rayleigh waves	3
1.2	Representation of a SAW sensor	4
1.3	Bi-dimensional strain sensing concept	6
1.4	Required setup to transmit the information from a sensor out of a Faraday cage	7
1.5	An elastic plate sandwiched by two piezoelectric transducers	8
2.1	Representation of a SAW device	16
2.2	Representation of the Fourier Transform of the IDTs with different numbers of fingers, centered around 100MHz	18
2.3	Representation of the effects of strains on IDTs	20
2.4	Representation of the propagation of the surface wave in a SAW sensor . . .	21
2.5	Variation of the determinant of G with potential wave velocities	29
2.6	Representation of a SAW strain sensor on a loaded beam	31
2.7	Computed variations of the SAW velocity under the strain ε due to the change in densities, elastic constants and initial stresses	32
2.8	Computed frequency shift under strain ε due to the wavelength and velocity change	33
2.9	Computed frequency shift under strain ε for a ZnO/glass sensor	34
2.10	Representation of a strain rosette and of its associated orientation	35

2.11	Representation of an acoustic device with three sets of IDTs for 2D strain measurement	36
2.12	Schematic of the AWR directivity in the wavenumber domain	38
2.13	Schematic of the envisioned configuration of the AWR	39
2.14	Representation of the change of the coordinate frame as well as the states of strains and stresses with the angle $\theta_0^{(p)}$	44
2.15	Representation of an AWR with the characteristics described in table 2.3	45
2.16	Frequency shifts associated with the AWR described in Table 2.3 on a loaded beam	46
3.1	Representation of the layer structure used for the SAW strain sensor	48
3.2	Layout of the electrodes in the actuator or receiver	49
3.3	Representation of the concept of photolithography and the different steps for electrode patterning	50
3.4	Manufacturing steps for the 1D SAW strain sensor	52
3.5	Pictures and microscopic view of the manufactured 1D device	53
3.6	Representation the resistive strain sensors on the beam (a) and of the Half-Wheatstone bridge (b)	55
3.7	Representation of the measurement setup for SAW and resistive strain gages	55
3.8	Experimental output signal (left) and associated spectrum (right) obtained from the manufactured 1D device	56
3.9	Experimental setup used for strain measurements over a loaded beam	57
3.10	Experimental and theoretical frequency shifts under strain for the 1D strain sensor	58
3.11	Pictures and microscopic views of the manufactured AWR	60
3.12	Experimental output signal (left) and associated spectrum (right) obtained from the manufactured 2D device	62

3.13	Experimental and theoretical frequency shifts for the AWR	63
4.1	Representation of the structure for acoustic data transmission by piezoelectric transduction	66
4.2	Representation of the forces and displacements applied on one element . . .	67
4.3	Representation the displacements, forces, electric potentials and currents for a) an actuator b) a receiver	69
4.4	Representation of a structure of N layers and with their associated stiffness matrices	72
4.5	Comparison of the transmitted power given by the rod model, a COMSOL 2D model and a COMSOL 3D model for a 1-mm-thick transducer bonded to a 1-mm-thick copper plate	74
4.6	2D finite element representation of the normalized longitudinal displacements at 2.15MHz	75
4.7	Representation of the structure for acoustic data transmission by piezoelectric transduction connected to electrical circuits	76
4.8	Representation of a two-port system for a) an air-backed transducer, b) a transducer backed by a layer of acoustic impedance Z_{back}	79
4.9	Equivalent model for n layers sandwiched between two piezoelectric transducers	81
4.10	Equivalent model for the experimental setup	84
4.11	Comparison of the transmitted power obtained from experimental results and the Mason model for 1.7 and 2.7-mm-thick transducers bonded to a 1-mm-thick copper plate by conductive silver epoxy	85
4.12	Comparison of the transmitted power obtained from experimental results and the Mason model for 0.7-mm-thick transducers bonded to a 2-mm-thick aluminum plate by vacuum grease	86
4.13	Comparison of the transmitted power obtained from experimental results and the Mason model for 0.7-mm-thick transducers bonded to a 3-mm-thick aluminum plate by solder patches	86

4.14	COMSOL 2D finite element representation of the normalized longitudinal displacements at resonance frequencies (4MHz) for configurations with a) silver epoxy bonding layers b) solder bonding layers	88
4.15	Comparison of the theoretical transmitted powers for 0.5-mm-thick transducers on a 1-mm-thick copper plate with 100- μm -thick bonding layers (density of 4000 k/m^3 , Young modulus ranging between 10 and 60 GPa)	89
5.1	Transmitted power for 0.5-mm-thick PZT5A transducers bonded to a 3-mm-thick aluminum plate by solder patches	93
5.2	Representation of (a) the structure for acoustic data transmission by piezoelectric transduction and (b) the wave-trapping effect of the backing	94
5.3	Transmitted power for 0.5-mm-thick PZT5A transducers bonded to a 3-mm-thick aluminum plate by solder patches, with epoxy backings of different thicknesses (0, 1, 5, 10 and 20 mm)	95
5.4	Comparison of the transmitted power for 0.5-mm-thick PZT5A transducers bonded to a 3-mm-thick aluminum plate by solder patches, with no backings, with a 10-mm-thick unloaded epoxy backing, and with a 7-mm-thick loaded epoxy backing	96
5.5	Representation of the structure for acoustic data transmission by piezoelectric transduction with (a) a tin electroplated layer, (b) a tin and a nickel electroplated layer	98
5.6	Comparison of the transmitted power for 0.5-mm-thick PZT5A transducers bonded to a 3-mm-thick aluminum plate by solder patches with loaded epoxy backing, without tin layer or with 100/200 μm tin layers	98
5.7	Transmitted power for the structure given in Table 5.1	99
5.8	Variations of the bandwidth at -2dB for different values of resistance and inductance in the load impedance, for 0.5-mm-thick transducers bonded to a 3-mm-thick aluminum plate by solder patches	101
5.9	Transmitted power for for the structure given in Table 5.2	102
5.10	(a) Variations of the bandwidth at -2dB for different values of resistance and inductance in the load impedance and (b) Transmitted power for the structure given in Table 5.3	103

5.11	(a) Variations of the bandwidth at -2dB for different values of resistance and inductance in the load impedance and (b) Transmitted power for the structure given in Table 5.4	105
5.12	Transmitted power for the structure given in Table 5.5	106
5.13	Transmitted power for the structure given in Table 5.6	108
6.1	Transmitted power for 4- μm -thick transducers bonded to a 3-mm-thick aluminum plate	111
6.2	Transmitted power for 100- μm -thick transducers bonded to a 3-mm-thick aluminum plate	112
6.3	Transmitted power for transducers of different thicknesses (70, 72, 74, 76, 78 and 80 μm) bonded to a 3-mm-thick aluminum plate	113
6.4	(a) Representation of the structure for acoustic data transmission by piezoelectric transduction with six channels of different transducer thicknesses and (b) Associated transmitted power	114
6.5	a) Angled, b) Staircase-shaped transducer	115
6.6	Comparison of the theoretical transmitted power for staircase (14 steps) and angled transducers ($L_{min} = 70\mu m$, $L_{max} = 80\mu m$) bonded to a 1-mm-thick aluminum plate with 1-mm-thick loaded epoxy baking layers	116
6.7	Representation of the structure for acoustic data transmission by piezoelectric transduction with staircase-shaped transducers	116
6.8	Electric representation of the staircase-shaped actuator and the connected circuit	117
6.9	Electric representation of one step of the receiving transducer	119
6.10	Electric representation of the staircase-shaped receiver and the connected load circuit	119
6.11	Electric representation of the staircase-shaped receiver and the connected load circuit under the assumption that the acoustic transmission is limited to the i-th step	120

6.12	Comparison of the transmitted power given by the extension of the Mason for staircase transducers with a FEM COMSOL 2D model for a staircase transducer (thickness ranging between 70 and 80 μm over 14 steps) bonded to a 1-mm-thick aluminum plate	121
6.13	Comparison of the transmitted power given by the extension of the Mason for staircase transducers (for 20, 50 and 100 steps) with a FEM COMSOL 2D model for an angled transducer (thickness ranging between 70 and 80 μm) bonded to a 1-mm-thick aluminum plate	122
6.14	Representation of a) $\hat{G}_1(x)$, b) $\hat{G}_2(x)$ for a 70- μm -thick transducer, of c) $\hat{G}_{1t}(x)$, d) $\hat{G}_{2t}(x)$ for transducers with thicknesses ranging between 70 and 80 μm , of e) $G_{1t}(\omega)$, f) $G_{2t}(\omega)$ (in dB) for the same configuration	124
6.15	Comparison of the transmitted power given by $G_{2t}(\omega)$ with the extension of the Mason for staircase transducers (50 steps) for an angled transducer (thickness ranging between 70 and 80 μm) bonded to a 1-mm-thick aluminum plate	127
6.16	Actuator and receiver with a thickness offset L_{add}	129
6.17	Comparison of the transmitted power for a configuration similar staircase actuators and receivers (20 steps, thickness between 70 and 80 μm) and a configuration with a receiver with an additional thickness of 5 μm	130
6.18	Variations of a) the bandwidth at -2dB , b) the transmitted power within the bandwidth, for different values of resistance and inductance in the input circuits	131
6.19	Transmitted power for the structure given in Table 6.1	132

SUMMARY

The work developed in this thesis targets two applications relative to piezoelectric transduction for sensing and data transmission purposes. The first project is based on a Surface Acoustic Wave device measuring strains in two directions along a plane. Such a device has been manufactured using microfabrication methods and tested on a loaded beam to determine its accuracy, while comparing the experimental output with the expected theoretical results.

The second project involves data transmission across a metallic barrier through piezoelectric transduction. A theoretical model has been derived to describe the electric and mechanical behaviors of the channels before comparing it with numerical and experimental results. Different approaches modifying the mechanical structure and the connected electric circuits have been pursued with the objective of reducing the amplitude variations down to 2 dB over large bandwidths for low carrier frequencies (below 10MHz). Transducer designs in the shape of staircases have been proposed for channels with high carrier frequencies (>100 MHz) in order to communicate over bandwidths larger than 100 MHz within which the amplitude variations are limited to 3 dB.

CHAPTER 1

INTRODUCTION

1.1 Overview

This work developed in this thesis will focus on two applications of acoustic transduction for strain sensing and data transmission. Both projects study the reception through a piezoelectric transducer of a wave that has been generated by a similar actuator and has propagated on a substrate (surface wave) or through a barrier (bulk wave).

The first application is an acoustic filter (Interdigital Transducer) measuring the frequency shift of surface waves to provide a strain measurement where the sensor is mounted. While common acoustic strain gages can measure one-dimensional deformations along the sensor, a two-dimensional design called Acoustic Wave Rosette (AWR) enables to provide the two normal strains and the shear strain on a plane with a single device. This thesis explores the theoretical relation between the frequency shifts and the applied strain, as well as the microfabrication and testing of this device.

The second application tackles the transmission of data through an elastic barrier by acoustic energy. By using two transducers bonded on a plate, bulk waves can be generated at a given carrier frequency and received on the other side in order to transmit information. The objective of this thesis will be to study analytically, numerically and experimentally the mechanical behavior of this system in order to optimize the transmission across the wall.

1.2 Background

1.2.1 Two-dimensional strain sensing

Acoustic sensors

Acoustic sensors are made of two transducers (an actuator and a receiver) between which a wave can propagate. When the environment of the sensor changes, the information received from the wave varies. The sensor can then connect the alteration of the physical quantity to the acoustic data and produce a measurement. These sensors have been used commercially for over 60 years because of their robustness and sensitivity. With the emergence of microfabrication techniques, they have also drawn interest because of their small dimensions and therefore low-energy requirements.

Two categories of acoustic sensors can be considered [1]:

- Bulk Wave sensors [2, 3, 4, 5]: They are the oldest devices with a simple configuration where a piezoelectric layer is sandwiched between two electrodes. When a voltage difference is applied on the electrodes, shear deformations generate bulk waves in the piezoelectric layer at the resonance frequency of the system. However, they are sensitive to surface interactions and the resonance frequency linearly depends on the masses applied at the surface. Thus such sensors can be used as mass, deposition rate or vapor sensors. Besides, they have the weakest sensitivity because of their low working frequency (between 5 and 30MHz).
- Surface Acoustic Wave sensors [6]: They are the most recent devices since most of the related research has been carried out in the last 20 years. These devices use Surface Acoustic Waves (SAWs), such as Rayleigh waves, to provide physical measurements. The frequency of the generated wave is filtered and its shift provides the information about its environment changes. The high working frequencies (between 100 and 500MHz) and the high concentration of acoustic energy at the surface can

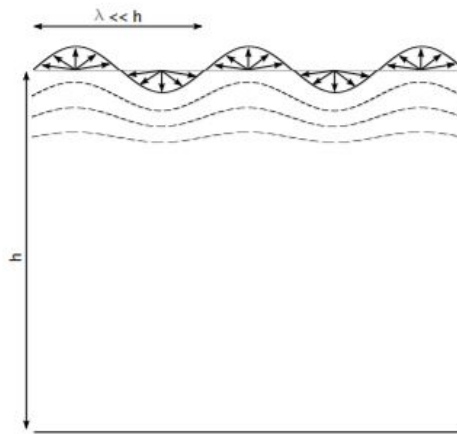


Figure 1.1: Qualitative schematic of the displacement field associated to Rayleigh waves

provide more accurate measurements than the Bulk Wave sensors[1].

The presence of SAWs has first been explained and described by Rayleigh in 1885 [7] (Figure 1.1). However, the design of SAW sensors has been made possible by the discovery of Interdigital Transducers (IDTs) in 1965 [8]. IDTs represent the pattern of a positive and negative electrodes in interlocking comb-shaped lines deposited upon a piezoelectric layer to create acoustic transducers. With such a design, the system acts a pass-band filter that can select a single frequency at both the actuation and the reception of the wave [9].

When a mass is added or the mechanical properties of the materials are modified, the peak at the selected frequency is shifted. Therefore, SAW sensors are sensitive to a wide number of physical quantities and can be used to measure various types of phenomena such as temperature [10], pressure [11], UV light [12], mass variations [13], torques [14], etc.

Configuration of SAW sensors

SAW devices are comprised of three layers (Figure 1.2):

- A thick passive layer (called the substrate) at the surface of which the wave mainly travels. It can be made of a variety of inactive materials, such as metals [15], glasses [12], silicone [16], etc. Its thickness is in the range of hundreds of microns.

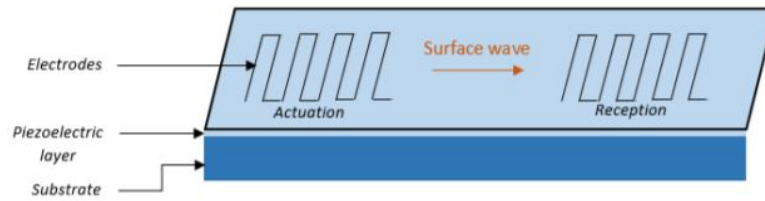


Figure 1.2: Representation of a SAW sensor

- A piezoelectric layer deposited upon the substrate. It acts as a transducer that transforms the electric voltage in a displacement (and conversely). Its thickness is in the range of microns.
- Electrodes in the shape of IDTs. They are metal layers located at the positions where the piezoelectric layer needs to be actuated. They are split between a positive and a negative electrode, whose thicknesses are in the range of hundreds of nanometers.

The whole device can then be bonded to the surface where the measurement is carried out and the electrodes are connected to external devices with wires.

The direct and inverse piezoelectric effects are used to generate and receive the surface waves. When a voltage difference is applied between the positive and negative electrode, a mechanical strain is created. On the other hand, the strain variation between two electrodes generates an electrical field. Therefore, they can be used as both actuator and receiver. The piezoelectric layer needs to be deposited by magnetron sputtering and can be made of various materials such as PZT [17], Aluminum nitride [15], Zinc Oxide [12], Langasite [18], Lithium Niobate [16], etc.

Strain measurement

One of the possible application for SAW sensors is strain measurement. There have been multiple examples of acoustic strain sensors in the literature manufactured with different piezoelectric materials [19, 20, 21, 15, 22]. In addition to the requirement of accurate measurements, there have been attempts to provide particular properties to the sensor such

as transparency [12] and bendability [22], by using specific materials. Given the impact of the temperature on the measurements [23], research has also been oriented towards temperature-compensated strain sensors [24]. Overall, the quality of the strain sensors are mainly characterized by:

- The range of strains over which measurements can be carried out
- The accuracy of the measurements over small strains

Strain measurements are to a key part Structural Health Monitoring (SHM) [25, 26], which refers to the implementation of different sensors detecting damages or the deterioration of a structure. Its objective is to reveal the signs of a structural failure before it happens and optimize the maintenance strategy. The advantages of an efficient SHM is a reduction of labor requirements during structural inspections, therefore limiting maintenance costs, while improving the confidence in the structure soundness. Such a monitoring is necessary in different fields such as aerospace [27] or civil engineering [28].

In a lot of aerospace applications, there are challenges to access the environment of the sensor because of its motion, such as the blades of an helicopter. Because of their small dimensions, SAW devices can work at a low power, which make them suitable for wireless operations [28, 29]. In this configuration, they can be considered as lowly invasive and can be used in moving environments. In addition, their limited size leads to a reduction of the manufacturing costs and their ability to measure deformations in the range of $\mu\epsilon$ has been experimentally shown [30].

Expansion to 2D strain measurements

In a plane, the total deformation state can be described by three distinct strains: two normal strains (ϵ_{xx} and ϵ_{yy}) as well as one shear strain (ϵ_{xy}). A common method to measure all three deformations together is to use a resistive rosette strain gage [32], which provides measurements in three angles defined by the rosette configuration that can be linearly re-

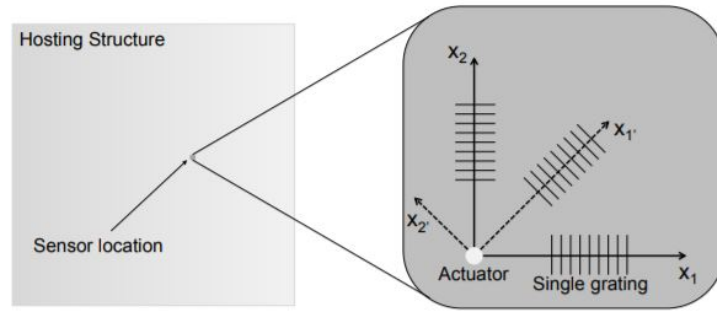


Figure 1.3: Bi-dimensional strain sensing concept [31]

lated to ϵ_{xx} , ϵ_{yy} and ϵ_{xy} . However, these resistive gages cannot work at low power and are not suited for wireless operations.

On the other hand, the current acoustic strain gages can only provide measurements along one direction. Possible 2D measurements could be carried out by associating three SAW strain sensors in distinct directions as an acoustic analogy to the resistive strain rosette (Figure 1.3). However, additional wires would be required, which would make the device more invasive.

A theoretical solution has been brought by Carrara [31] who proposed to design an acoustic device combining in a single sensor the role of three IDTs oriented along three different angles and working at separate frequencies, therefore providing strain measurements in three distinct directions. Such a sensor is called the Acoustic Wave Rosette (AWR).

The AWR relies on the concept of wave steering with a frequency dependence. Simple wave steering has been extensively researched in various fields such as radar, sonar, seismology, oceanology, and medical imaging. The most common method is to use phased arrays [33, 34], which are a group of sensors located in a pattern such that the relative phase of each transducer enables the propagation in a desired direction while inhibiting it in the undesired ones. IDTs are the most prevalent method to steer waves in one direction for SAW sensors while operating at a single frequency [35]. The slanted IDT [36] and the annular IDTs [37] are other alternative configurations that can achieve novel functionalities such as wide-band operations and acoustic wave focusing. In [38], an antenna with

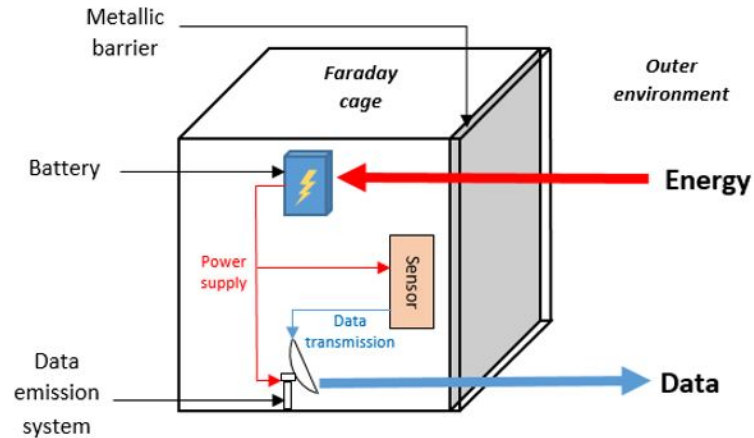


Figure 1.4: Required setup to transmit the information from a sensor out of a Faraday cage frequency steering transduction has been designed.

With the Frequency Steerable Acoustic Transducer (FSAT), Senesi [39] defined a strategy to provide directional frequency dependence to a transducer by designing it in the wavenumber domain. The steering capabilities of the device have been shown experimentally [40, 41] and can be used for NDT purposes. The same design strategy in the wavenumber domain is used for the FSAT and the AWR. However, while the FSAT emits waves in all directions, the AWR only generates waves along three angles at distinct frequencies to simulate the action of three IDTs.

1.2.2 Acoustic data transmission across a barrier

Data transmission across a metallic barrier

Different methods ensuring data transmissions across elastic barriers without drilling have been developed and published in the literature. A first category relies on electromagnetic (EM) waves and contains capacitive coupling [42], inductive coupling [43, 44] or magnetic resonance coupling [45]. However, when the structure hosting one of the transducers is metallic and sealed, a Faraday shielding occurs and prevents any EM waves from being transmitted across the wall and the efficiency of such a system collapses.

As a result, a second method is necessary to ensure the data transmission across sealed

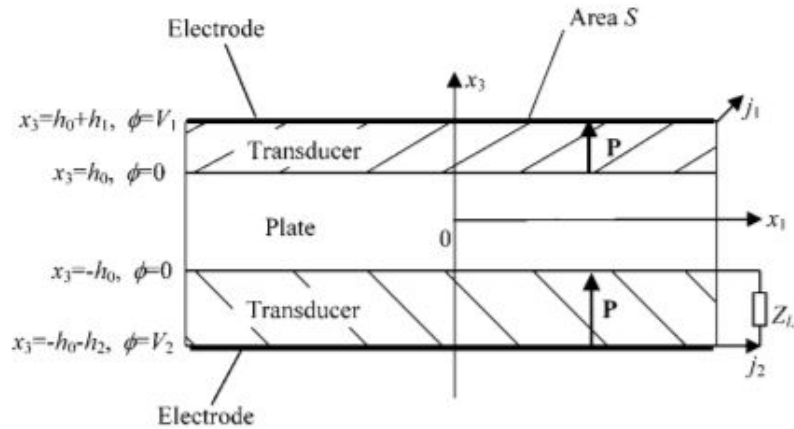


Figure 1.5: An elastic plate sandwiched by two piezoelectric transducers [48]

metallic structures and acoustic solutions have been developed to provide a solution. Electromagnetic Acoustic Transducers (EMATs) use a magnet and a coil to apply the Lorentz force and generate bulk waves across the barrier [46]. Magnetostrictive patches is another alternative but is still at an early stage [47]. The last traditional acoustic option consists in bonding piezoelectric transducers on both sides of the plate.

These acoustic channels can be used to transmit information from sensors inside a sealed metallic environment such as a submarine or a waste container towards the outside without drilling in the structure. The acoustic transmission across the metallic barrier serves two purposes (Figure 1.4):

- A data channel combining an actuator and a receiver on both sides of the plate should transmit information across the barrier
- A power channel transmitting acoustic energy that can be converted towards electric energy to feed the sensor and the data emission system encapsulated inside the sealed structure

Piezoelectric transmission

Piezoelectric channels provide the ability to send and receive both data and energy through metallic walls with a reasonable power. The first idea of using piezoelectric energy to trans-

fer data and energy through a wall has emerged and been patented in 1997 [49] and consists of two transducers facing each other across a plate, while using a signal generator to actuate one side and an oscilloscope to receive the signal. In 2003, Hu et al [48] theoretically showed that the transmission of electric energy through a metal plate sandwiched between piezoelectric actuators and receivers (Figure 1.5) can be achieved. A one-dimensional theoretical model describing the conversion of electric into acoustic energy, and then towards electric power into a load circuit was derived.

From there, the research has been oriented into two directions following the purposes described previously:

- The power delivery [50, 51], where the objective is to harvest a maximum amount of energy from the receiving transducer at a given frequency. The research on this area focuses on the efficiency of the energy transduction between both piezoelectric transducers [48], as well as the circuits and storage systems [52].
- The data transmission, where the objective is to transmit the highest voltage possible over a given bandwidth. Unlike the power delivery, the efficiency is not a decisive feature since the electric currents are not considered. The two key characteristics are the voltage output amplitude and the associated bandwidth. Indeed, a high voltage output enables a better comprehension of the data and requires a lower input voltage. An important bandwidth improves the data transmission rate.

The ultimate purpose is to associate both of these tasks on the same plate [53] so that the power delivery system can feed the sensor and the data transmission system.

Piezoelectric data transmission

The first reports of piezoelectric data transmission carried out experimentally were reported in 2006 [53, 54, 55]. The maximum transmission rate achieved was 55 kbps (kilobits per

seconds). In 2010, high-data rate transmission systems appeared [56, 57]. In this experiments, the data rate could be improved by replacing the couplant (previously in epoxy) by a gel. This enabled to work with a larger bandwidth and transmit data in the range of the mbps (megabits per second).

Different efforts have been carried out to enhance the quality of the data communication by (i) processing the data to reduce the effects of wave reflection between the layers (ii) modeling the transmission in order to optimize the system configuration.

The original model from Hu *et al* [48] solves analytically the wave propagation equation as well the equations of piezoelectricity to provide the output voltage, current and power. Different equivalent circuit methods, such as Mason's model or Leach's model [58] use the properties of piezoelectric and non-piezoelectric media as an analogy to electrical circuits. A transfer matrix method using ABCD parameters [59] describes the system as two-port networks with forward and backward traveling waves.

Finite element model (FEM) simulations have also been used to model the structure and investigate the influence of different parameters [60]. The simulation can be realized through commercially available software such as COMSOL or ANSYS and compared to experimental results [61]. Besides, the analytical methods enable to study simple structures in one dimension, but will fail to describe complex geometries. On the other hand, FEM can provide results incorporating the boundary effects of complex geometries or the effect of a curved surface [58].

Different equalization techniques and digital communication methods have been implemented in order to reduce the impact of the reflections between the layers. Indeed the echoing generate large delays and leads to significant interferences while transmitting at high data rates [62]. An echo-cancellation using predistortion filter at the actuation to generate destructive interference of echoes at the receiver has been tested [62, 56]. Orthogonal frequency-division multiplexing (OFDM) is another method coming from RF systems that divides the wideband transmission channel into several orthogonal narrowband channels in

order to mitigate the effect of echoing for each of them [63, 57].

1.3 Motivations and objectives

1.3.1 Two-dimensional strain sensing

Reliable damage characterization in civil structures and infrastructure is an important objective of structural health monitoring (SHM). This requires an accurate characterization of damage at early stages and a continuous monitoring of critical parameters such as strains. The characterization of the state of strains over a surface is usually performed by resistive strain rosettes. However, such sensors cannot operate at low-power and be wireless. This limitation prevents them from being used in moving pieces such as the rotor blades from helicopters. The solution for wireless strain sensing is usually brought by SAW sensors, which have only been shown to operate measurements in 1D until now.

A theoretical solution has been brought by Carrara [31] with the Acoustic Wave Rosette. However, its frequency dependant wave steering in three distinct directions has never been shown experimentally, nor its ability to provide 2D strain measurements. The first objectives of this project will be to replicate the one-dimensional strain measurements results by:

- Defining a geometry for the 1D strain sensor and derive the expected strain/frequency relation
- Specifying a manufacturing protocol adequate with the equipment in GeorgiaTech cleanroom and manufacturing the device
- Testing its ability to generate and receive a wave at a specific filtered frequency
- Testing its ability to provide accurate measurements in 1D

In a second time, these steps need to be repeated for the 2D strain sensor by:

- Defining a geometry for the AWR and deriving the variation of the three filtered frequencies with planar strains
- Manufacturing the AWR
- Testing its ability to generate and receive three distinct waves at different frequencies
- Testing its ability to provide accurate measurements in 2D

1.3.2 Acoustic data transmission across a barrier

In a lot of industrial applications, data from sensors need to be transmitted from enclosed structures such as waste containers, submarines or pipelines. When the structure is sealed and metallic, the Faraday shielding prevents the electromagnetic (EM) wave transmission and the information can only be conveyed mechanically. Ultrasonic signaling for data transmission by piezoelectric transduction offers a reliable way to provide an efficient transmission, but challenges such as signal/noise ratio, reflection between layers or crosstalk between different channels need to be addressed.

A proper signal processing can answer some of the issues relative to echoing. However, in order to achieve high data rate transmissions, the channel should also be able to transmit signals over a large frequency bandwidth with constant amplitude, which requires an appropriate design in terms of materials and geometry. This project will focus on the latter and the objectives will be to:

- Define a reliable and simple model that can describe the mechanical behavior of the acoustic channel
- Compare this model with experimental results to establish its validity
- Implement a strategy to enable a transmission over a large bandwidth at a high and constant amplitude
- Define a channel configuration following this strategy before testing it experimentally

1.4 Contributions

Achievement of the objectives outlined in the previous section have led to the following contributions:

- The influence of 2D strains on the frequencies filtered by the AWR have been theoretically defined
- The AWR has been manufactured with microfabrication methods with an Aluminum Nitride piezoelectric layer upon a glass substrate
- The AWR has been experimentally characterized and its ability to measure all planar strains has been validated
- A simple analytical modeled describing the mechanical behavior of the piezoelectric data transmission channel has been derived and successfully validated by numerical and experimental results
- Different approaches involving additional backing and intermediate layers as well as electric impedances have been introduced to reduce the amplitude variations within large bandwidths at low frequencies (< 10 MHz)
- An alternate structure shaped like a staircase has been introduced to reduce the amplitude variations within large bandwidths at high frequencies (> 100 MHz)

1.5 Organization of the thesis

The thesis is organized in seven chapters including this introduction. Chapter 2 presents the design of the Acoustic Wave Rosette (AWR) as well as the theoretical relations between the frequencies filtered by the sensor and the applied strains. Chapter 3 tackles the manufacturing of the 1D and the 2D devices, their experimental characterization and the investigation of their sensing capabilities under strain. In Chapter 4, theoretical models describing the

mechanical behavior of the data transmission channels are expressed and compared with finite element and experimental results. Chapter 5 presents the implementation of a strategy to derive a channel configuration capable of transmitting a signal over a large bandwidth with a constant amplitude. Chapter 6 introduces staircase-shaped transducers that targets carrier frequencies and bandwidths in the range of hundreds of MHz. Finally, Chapter 7 outlines conclusions drawn from the work and provides recommendations for future investigations.

CHAPTER 2

DESIGN OF THE ACOUSTIC WAVE ROSETTE

2.1 Overview

Strain sensing is a possible application for Surface Acoustic Wave (SAW) sensors that falls within the field of Structural Health Monitoring. Different examples of SAW devices measuring deformations along one direction have been introduced in the literature [20, 64, 21, 15, 22].

The first section will focus on the theoretical approach necessary to assess the mechanical behavior of these sensors under deformation. Indeed they rely on the shift of frequencies filtered by the electrodes when a strain is applied. The slopes of these frequency changes can be computed theoretically and are based on two phenomena:

- The deformation of the layers and consequently of the electrode pattern
- The change in velocity due to the applied strains and stresses

The approach used to retrieve the frequency shifts under strain has been defined and verified by comparing it to experimental results obtained from the literature.

The second section will focus on an electrode pattern, called Acoustic Wave Rosette (AWR), that has been theoretically introduced by Carrara [31] in order to extend the concept of acoustic strain sensing towards a second dimension. The electrode pattern is defined in the wave number domain and is characterized as three maxima corresponding to specific strain directions. Its mechanical behavior under 2D strains has also been studied and a numerical example has been provided.

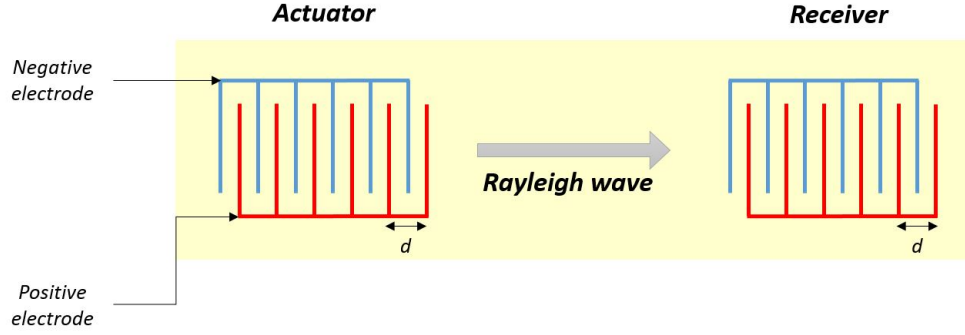


Figure 2.1: Representation of a SAW device

2.2 SAW device for 1D strain sensing

2.2.1 Introduction to Interdigital Transducers

The local detection of strains in one dimension with SAW sensors relies on the generation and reception of Rayleigh waves centered around one frequency along this direction. The frequency filtering and 1D directional capabilities are achieved by using Interdigital Transducers (IDTs) patterns. They are designed as positive and negative electrode lines interlocked in a comb-shape (Figure 2.1). Therefore the IDTs act as a spacial filter selecting the frequency associated with the SAW wavelength $\lambda = d$, where d is the periodicity of the electrode pattern. The layouts of the actuators and receivers are identical and can be mathematically expressed for infinitely thin electrodes as:

$$f(x) = \sum_{i=0}^{I-1} \underbrace{\delta(x - (x_i^{pos}))}_{\text{positive electrode}} - \underbrace{\delta(x - (x_i^{neg}))}_{\text{negative electrode}} \quad (2.1)$$

where x_i^{pos} and x_i^{neg} are the positions of the i -th positive and negative electrodes and can be expressed as:

$$\begin{aligned} x_i^{pos} &= x_0 + id \\ x_i^{neg} &= x_0 + id + d \end{aligned} \quad (2.2)$$

x_0 represents the position of the sensor, I is the total number of fingers in each electrode and δ is the Dirac function. The filtering properties of the IDTs can be shown by its wavenumber representation $D(k)$, and are expressed by the Fourier Transform of Equation 2.2:

$$D(k) = \sum_{i=0}^{I-1} \frac{e^{jkx_0}}{\sqrt{2\pi}} (e^{jkid} - e^{jk(i+\frac{1}{2})d}) \quad (2.3)$$

Equation 2.3 can be rearranged into:

$$D(k) = \frac{e^{jkx_0}}{\sqrt{2\pi}} \frac{\sin(\frac{I}{2}kd)}{\sin(\frac{1}{2}kd)} (1 - e^{\frac{jkd}{2}}) e^{\frac{jkd(I-1)}{2}} \quad (2.4)$$

The function $|D(k)|$ reaches a maximum when its denominator tends toward 0, which happens for the wavenumber k_f :

$$\frac{1}{2}k_f d = p\pi \quad (2.5)$$

where p is an integer.

Consequently the IDTs act as spatial filters for wavenumbers determined by the finger periodicity d . The case where $p = 1$ represents the filtering associated with the fundamental periodicity d and is the one that will be studied from now. Given the non-dispersive nature of the Rayleigh waves, the wavenumber k_f is directly related to a center frequency f_f by its velocity c_R . From Equation 2.5, f_f can be expressed as (for $p = 1$):

$$f_f = \frac{c_R}{d} \quad (2.6)$$

$|D(k(f))|$ describes the signal that would be emitted or received by the IDTs from a broadband input. Figure 2.2 is a representation $|D(k(f))|$ for a configuration centered around 100MHz for different numbers of fingers. The filtering capabilities of the IDTs are highlighted by the presence of a main peak around the targeted frequency, whose width decreases as the amount of electrodes grows.

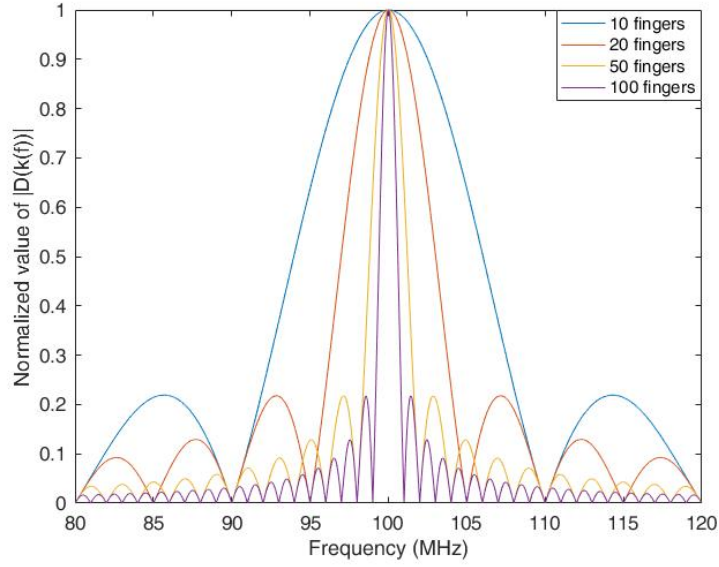


Figure 2.2: Representation of the Fourier Transform of the IDTs with different numbers of fingers, centered around 100MHz

2.2.2 Introduction to 1D strain measurement

The application of a load along the sensor induces a longitudinal strain ε that alters the frequency filtered by the IDTs on the base of two effects:

- The locations of each positive and negative electrodes x_i^{pos} and x_i^{neg} are shifted by amounts u_i^{pos} and u_i^{neg}
- The material characteristics of the propagating layers (piezoelectric and substrate) are changed and therefore modify the wave velocity $c_R(\varepsilon)$

The equations 2.1 to 2.6 can be rewritten to account for the effect of the strain. The new positions of the electrodes are expressed as:

$$f(x) = \sum_{i=0}^{I-1} \underbrace{\delta(x - (x_i^{pos} + u_i^{pos}))}_{\text{positive electrode}} - \underbrace{\delta(x - (x_i^{neg} + u_i^{neg}))}_{\text{negative electrode}} \quad (2.7)$$

The displacements of each electrodes are formulated as:

$$\begin{aligned} u_i^{pos} &= x_i^{pos} \bar{\varepsilon}_i^{pos} \\ u_i^{neg} &= x_i^{neg} \bar{\varepsilon}_i^{neg} \end{aligned} \quad (2.8)$$

where $\bar{\varepsilon}_i^{pos}$ and $\bar{\varepsilon}_i^{neg}$ are the local strains under the i -th positive and negative electrodes. Given the typical small dimensions of SAW sensors (in the range of millimeters), the assumption that strains remain uniform underneath the device is used:

$$\bar{\varepsilon}_i^{pos} = \bar{\varepsilon}_i^{neg} = \varepsilon \quad (2.9)$$

The design in the wavenumber domain under strain is therefore:

$$D(k) = \frac{e^{jkx_0} \sin(\frac{I}{2}kd(1+\varepsilon))}{\sqrt{2\pi} \sin(\frac{1}{2}kd(1+\varepsilon))} (1 - e^{\frac{jkd(1+\varepsilon)}{2}}) e^{\frac{jkd(1+\varepsilon)(I-1)}{2}} \quad (2.10)$$

Consequently the main peak associated with the fundamental periodicity of $|D(k)|$ occurs at:

$$\frac{1}{2}k_f d(1+\varepsilon) = \pi \quad (2.11)$$

As a result, the main frequency filtered by the IDTs under strain is:

$$f_f(\varepsilon) = \frac{c_R(\varepsilon)}{d(1+\varepsilon)} \quad (2.12)$$

Equation 2.12 highlights the fact that the periodicity of the electrode fingers, as well as the filtered wavelength λ , shift from a distance d to $d(1+\varepsilon)$. Besides, the strain modifies the properties of the materials within which the surface wave propagates, thus altering the wave velocity.

Therefore the impact of strains on IDTs is a combination of these two events (Figure 2.3).

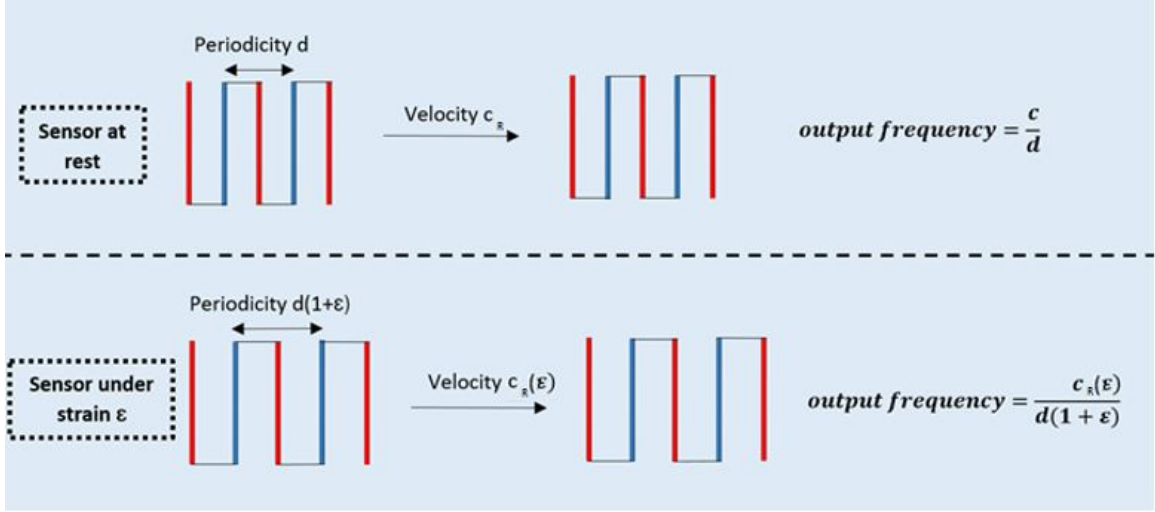


Figure 2.3: Representation of the effects of strains on IDTs

2.2.3 Influence of the strain on the SAW velocity

Rayleigh wave velocity in two layers

In the following equations the time derivation will be represented by a dot, the space derivation is represented by a comma preceding the index and the summation of repeated indexes is used as a convention.

The propagation velocity of the Rayleigh wave in the SAW sensor can be obtained through numerical computations [65, 66, 67]. In the strain sensor, the surface wave propagates along the x_1 direction through the piezoelectric layer and the top of the substrate. x_3 is relative to the direction going toward the plate thickness. The coordinates $x_3 = 0$ and $x_3 = h$ represent respectively the interface between the two layers and the top of the piezoelectric layer (Figure 2.4).

The equations describing the motion for the SAW are modified to account for (i) the piezoelectric properties of the upper layer (ii) the application of initial stresses.

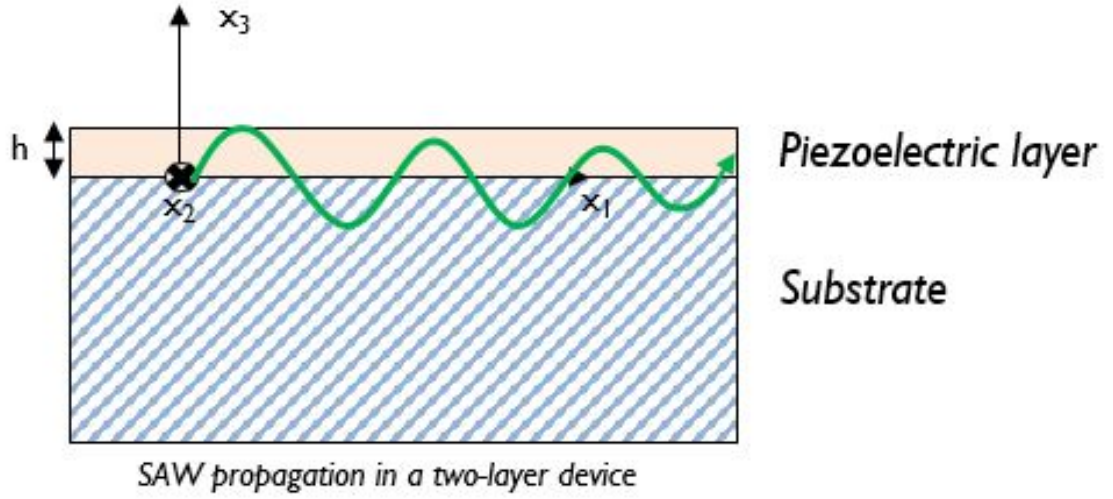


Figure 2.4: Representation of the propagation of the surface wave in a SAW sensor

In the substrate, the equations are:

$$\begin{aligned}\sigma_{ik}u_{j,ki} + c_{ijkl}u_{k,li} &= \rho\ddot{u}_j \\ T_{ij} &= c_{ijkl}u_{k,l} + \sigma_{ik}u_{j,k}\end{aligned}\tag{2.13}$$

where σ is the initial stress, c is the elastic constant, ρ is the density, u is the displacement and T is the total stress.

The equations in the upper layer are:

$$\begin{aligned}\sigma_{ik}u_{j,ki} + c_{ijkl}u_{k,li} + e_{kij}\phi_{,ki} &= \rho\ddot{u}_j \\ e_{ikl}u_{k,li} - \epsilon_{ik}\phi_{,ki} &= 0 \\ T_{ij} &= c_{ijkl}u_{k,l} + \sigma_{ik}u_{j,k} + e_{kij}\phi_{,k} \\ D_i &= e_{ikl}u_{k,l} - \epsilon_{ik}\phi_{,k}\end{aligned}\tag{2.14}$$

where e is the piezoelectric constant, ϵ is the permittivity constant, ϕ is the electric potential and D is the electric displacement.

Thereafter, the indices (s) will refer to the substrate and (p) to the piezoelectric layer. The absence of index means that the equation is valid for both layers.

General solutions for the displacements $\mathbf{u} = \{u_1, u_2, u_3\}$ and the electric potential ϕ are linear combinations of N fundamental solutions for waves propagating along the x_1 direction with an exponential decay in the x_3 direction.

For the substrate:

$$\begin{aligned}
 u_{i(s)} &= \sum_{l=1}^{N(s)} B_{(s)}^{(l)} \beta_{i(s)}^{(l)} \exp(j\alpha_{(s)}^{(l)} \omega x_3 / c_R) \exp(j\omega(t - x_1 / c_R)), \quad i = 1, 2, 3 \\
 \phi_{(s)} &= \sum_{l=1}^{N(s)} B_{(s)}^{(l)} \beta_{4(s)}^{(l)} \exp(j\alpha_{(s)}^{(l)} \omega x_3 / c_R) \exp(j\omega(t - x_1 / c_R))
 \end{aligned} \tag{2.15}$$

For the piezoelectric layer:

$$\begin{aligned}
 u_{i(p)} &= \sum_{l=1}^{N(p)} B_{(p)}^{(l)} \beta_{i(p)}^{(l)} \exp(j\alpha_{(p)}^{(l)} \omega x_3 / c_R) \exp(j\omega(t - x_1 / c_R)), \quad i = 1, 2, 3 \\
 \phi_{(p)} &= \sum_{l=1}^{N(p)} B_{(p)}^{(l)} \beta_{4(p)}^{(l)} \exp(j\alpha_{(p)}^{(l)} \omega x_3 / c_R) \exp(j\omega(t - x_1 / c_R))
 \end{aligned} \tag{2.16}$$

where, for each fundamental solution, α is a decay constant relative to the x_3 direction, β_i ($i=1,2,3,4$) are amplitudes associated with the displacements and electric potential, and B is a weighting factor that is determined by the applied boundary conditions.

The objective of the further approach is to compute the velocity c_R of the Rayleigh wave propagating in the two layers. However, it is impossible to directly calculate its value and an iterative approach is necessary. Consequently, a first value of c_R is assumed.

By injecting the fundamental solutions into the Equations 2.13 for the substrate and 2.14 for the piezoelectric layer, linear homogeneous equations for the variables $\beta_1, \beta_2, \beta_3$ and β_4 are obtained:

$$[H(\alpha)] * \{\beta\} = \{0\} \tag{2.17}$$

where

$$[H] = \begin{bmatrix} H_{11} & H_{12} & H_{13} & H_{14} \\ H_{12} & H_{22} & H_{23} & H_{24} \\ H_{13} & H_{23} & H_{33} & H_{34} \\ H_{14} & H_{24} & H_{34} & H_{44} \end{bmatrix} \quad (2.18)$$

$$\{\beta\} = \begin{bmatrix} \beta_1 \\ \beta_2 \\ \beta_3 \\ \beta_4 \end{bmatrix}$$

and

$$\begin{aligned} H_{11} &= (c_{55} + \sigma_{33})\alpha^2 + 2(c_{15} + \sigma_{13})j\alpha - (c_{11} + \sigma_{11}) + \rho c_R^2 \\ H_{22} &= (c_{44} + \sigma_{33})\alpha^2 + 2(c_{46} + \sigma_{13})j\alpha - (c_{66} + \sigma_{11}) + \rho c_R^2 \\ H_{33} &= (c_{33} + \sigma_{33})\alpha^2 + 2(c_{35} + \sigma_{13})j\alpha - (c_{55} + \sigma_{11}) + \rho c_R^2 \\ H_{12} &= c_{45}\alpha^2 + (c_{14} + c_{56})j\alpha - c_{16} \\ H_{13} &= c_{35}\alpha^2 + (c_{13} + c_{55})j\alpha - c_{15} \\ H_{23} &= c_{34}\alpha^2 + (c_{36} + c_{45})j\alpha - c_{56} \\ H_{14} &= e_{35}\alpha^2 + (e_{15} + e_{31})j\alpha - e_{11} \\ H_{24} &= e_{34}\alpha^2 + (e_{14} + e_{36})j\alpha - e_{16} \\ H_{34} &= e_{33}\alpha^2 + (e_{13} + e_{35})j\alpha - e_{15} \\ H_{44} &= -\epsilon_{33}\alpha^2 - 2\epsilon_{13}j\alpha + \epsilon_{11} \end{aligned} \quad (2.19)$$

In the previous expression, the elastic and piezoelectric constants (c_{ij} and e_{ij}) are written with the compact Voigt notation that will also be used further in this section. This definition of the $[H]$ matrix can be used for the piezoelectric layer as well as the substrate, where the piezoelectric and permittivity constants e_{ij} and ϵ_{ij} can be respectively replaced by 0 and 1.

The only non-trivial solutions to 2.17 are given by:

$$\det[H(\alpha)] = 0 \quad (2.20)$$

For both the substrate and the piezoelectric layer, Equation 2.20 can be solved numerically to provide solutions for the damping coefficient α under the form of complex conjugate pairs. Since the required solutions represent surface waves, the displacement amplitude needs to decay as the x_3 position increases. As a result, the only acceptable coefficients α in the substrate have a negative imaginary part. On the other hand, all the solutions found for the piezoelectric layer can be accepted. Overall, eight possible solutions can be selected for the piezoelectric layer as well as four solutions for the substrate.

For each root α thus found, there is a four component vector $\{\beta\} = \{\beta_1, \beta_2, \beta_3, \beta_4\}$ that can be deduced from the eigenvalue problem 2.17.

The weighting coefficients B are determined by applying boundary conditions to the partial waves propagating in the substrate and in the piezoelectric layers described by equation 2.15.

At the limit between the two layers ($x_3 = 0$), the boundary conditions are:

- The continuity of the longitudinal, transverse and vertical mechanical displacements:

$$u_{1p} = u_{1s} \quad (2.21)$$

$$u_{2p} = u_{2s} \quad (2.22)$$

$$u_{3p} = u_{3s} \quad (2.23)$$

- The continuity of the electric potential:

$$\phi_p = \phi_s \quad (2.24)$$

- The continuity of the normal components of stresses:

$$T_{13p} = T_{13s} \quad (2.25)$$

$$T_{23p} = T_{23s} \quad (2.26)$$

$$T_{33p} = T_{33s} \quad (2.27)$$

- The continuity of the normal electrical displacement:

$$D_{3p} = D_{3s} \quad (2.28)$$

At the surface ($x_3 = h$), the boundary conditions are:

- The vanishing of the traction force:

$$T_{13p} = 0 \quad (2.29)$$

$$T_{23p} = 0 \quad (2.30)$$

$$T_{33p} = 0 \quad (2.31)$$

- The continuity of the normal electrical displacement at a free surface:

$$D_{3p} = k\epsilon_0\phi_p \quad (2.32)$$

The boundary conditions 2.21 to 2.32 form a set of twelve homogeneous equations for the four weighting coefficients B_s of the substrate and the eight coefficients B_p of the piezoelectric layer. They can be expressed in a matrix form:

$$[G]\{B\} = 0 \quad (2.33)$$

where $\{B\}$ is the vector of weighting coefficients and $[G]$ is a 12X12 matrix depending on the decay coefficients α , on the eigenvectors β_i and implicitly on the wave velocity c_R . The coefficients of $[G]$ are obtained by substituting the solutions (2.15) and (2.16) into the equations (2.21) to (2.32), where the expressions of the total stress T and the electric displacement D can be explicitly formulated from (2.13) (for the substrate) and (2.14) (for the piezoelectric layer).

More specifically, $[G]$ can be split into two submatrices $[G_p, G_s]$, where G_p represents the eight left columns and is associated with the left-hand sides of the boundary conditions. Therefore G_s represents the four right columns and is associated with the right-hand sides

of the boundary conditions. The explicit coefficients of $[G_p]$ are, for $l = 1, \dots, 8$:

$$\begin{aligned}
G_{1l(p)} &= \beta_{1(p)}^{(l)} \\
G_{2l(p)} &= \beta_{2(p)}^{(l)} \\
G_{3l(p)} &= \beta_{3(p)}^{(l)} \\
G_{4l(p)} &= \beta_{4(p)}^{(l)} \\
G_{5l(p)} &= [(c_{15(p)} + \sigma_{13(p)}) + (c_{55(p)} + \sigma_{33(p)})\alpha_{(p)}^{(l)}]\beta_{1(p)}^{(l)} + [c_{56(p)} + c_{45(p)}\alpha_{(p)}^{(l)}]\beta_{2(p)}^{(l)} + \\
&\quad [c_{55(p)} + c_{35(p)}\alpha_{(p)}^{(l)}]\beta_{3(p)}^{(l)} + [e_{15(p)} + e_{35(p)}\alpha_{(p)}^{(l)}]\beta_{4(p)}^{(l)} \\
G_{6l(p)} &= [c_{14(p)} + c_{45(p)}\alpha_{(p)}^{(l)}]\beta_{1(p)}^{(l)} + [(c_{46(p)} + \sigma_{13(p)}) + (c_{44(p)} + \sigma_{33(p)})\alpha_{(p)}^{(l)}]\beta_{2(p)}^{(l)} + \\
&\quad [c_{45(p)} + c_{34(p)}\alpha_{(p)}^{(l)}]\beta_{3(p)}^{(l)} + [e_{14(p)} + e_{34(p)}\alpha_{(p)}^{(l)}]\beta_{4(p)}^{(l)} \\
G_{7l(p)} &= [c_{13(p)} + c_{35(p)}\alpha_{(p)}^{(l)}]\beta_{1(p)}^{(l)} + [c_{36(p)} + c_{34(p)}\alpha_{(p)}^{(l)}]\beta_{2(p)}^{(l)} + \\
&\quad [(c_{35(p)} + \sigma_{13(p)}) + (c_{33(p)} + \sigma_{33(p)})\alpha_{(p)}^{(l)}]\beta_{3(p)}^{(l)} + [e_{13(p)} + e_{33(p)}\alpha_{(p)}^{(l)}]\beta_{4(p)}^{(l)} \\
G_{8l(p)} &= [e_{13(p)} + e_{35(p)}\alpha_{(p)}^{(l)}]\beta_{1(p)}^{(l)} + [e_{36(p)} + e_{34(p)}\alpha_{(p)}^{(l)}]\beta_{2(p)}^{(l)} + \\
&\quad [e_{35(p)} + e_{33(p)}\alpha_{(p)}^{(l)}]\beta_{3(p)}^{(l)} - [\epsilon_{13(p)} + \epsilon_{33(p)}\alpha_{(p)}^{(l)}]\beta_{4(p)}^{(l)} \\
G_{9l(p)} &= [(c_{15(p)} + \sigma_{13(p)}) + (c_{55(p)} + \sigma_{33(p)})\alpha_{(p)}^{(l)}]\beta_{1(p)}^{(l)} + [c_{56(p)} + c_{45(p)}\alpha_{(p)}^{(l)}]\beta_{2(p)}^{(l)} + \\
&\quad [c_{55(p)} + c_{35(p)}\alpha_{(p)}^{(l)}]\beta_{3(p)}^{(l)} + [e_{15(p)} + e_{35(p)}\alpha_{(p)}^{(l)}]\beta_{4(p)}^{(l)} * \exp(jk\alpha_{(p)}^{(l)}h) \\
G_{10l(p)} &= [c_{14(p)} + c_{45(p)}\alpha_{(p)}^{(l)}]\beta_{1(p)}^{(l)} + [(c_{46(p)} + \sigma_{13(p)}) + (c_{44(p)} + \sigma_{33(p)})\alpha_{(p)}^{(l)}]\beta_{2(p)}^{(l)} + \\
&\quad [c_{45(p)} + c_{34(p)}\alpha_{(p)}^{(l)}]\beta_{3(p)}^{(l)} + [e_{14(p)} + e_{34(p)}\alpha_{(p)}^{(l)}]\beta_{4(p)}^{(l)} * \exp(jk\alpha_{(p)}^{(l)}h) \\
G_{11l(p)} &= [c_{13(p)} + c_{35(p)}\alpha_{(p)}^{(l)}]\beta_{1(p)}^{(l)} + [c_{36(p)} + c_{34(p)}\alpha_{(p)}^{(l)}]\beta_{2(p)}^{(l)} + \\
&\quad [(c_{35(p)} + \sigma_{13(p)}) + (c_{33(p)} + \sigma_{33(p)})\alpha_{(p)}^{(l)}]\beta_{3(p)}^{(l)} + [e_{13(p)} + e_{33(p)}\alpha_{(p)}^{(l)}]\beta_{4(p)}^{(l)} * \exp(jk\alpha_{(p)}^{(l)}h) \\
G_{12l(p)} &= [e_{13(p)} + e_{35(p)}\alpha_{(p)}^{(l)}]\beta_{1(p)}^{(l)} + [e_{36(p)} + e_{34(p)}\alpha_{(p)}^{(l)}]\beta_{2(p)}^{(l)} + \\
&\quad [e_{35(p)} + e_{33(p)}\alpha_{(p)}^{(l)}]\beta_{3(p)}^{(l)} - [\epsilon_{13(p)} + \epsilon_{33(p)}\alpha_{(p)}^{(l)} - j\epsilon_0]\beta_{4(p)}^{(l)} * \exp(jk\alpha_{(p)}^{(l)}h)
\end{aligned} \tag{2.34}$$

The explicit coefficients of $[G_s]$ are, for $l = 1, \dots, 4$:

$$\begin{aligned}
G_{1l(s)} &= -\beta_{1(s)}^{(l)} \\
G_{2l(s)} &= -\beta_{2(s)}^{(l)} \\
G_{3l(s)} &= -\beta_{3(s)}^{(l)} \\
G_{4l(s)} &= -\beta_{4(s)}^{(l)} \\
G_{5l(s)} &= -\left([(c_{15(s)} + \sigma_{13(s)}) + (c_{55(s)} + \sigma_{33(s)})\alpha_{(s)}^{(l)}]\beta_{1(s)}^{(l)} + [c_{56(s)} + c_{45(s)}\alpha_{(s)}^{(l)}]\beta_{2(s)}^{(l)} + \right. \\
&\quad \left. [c_{55(s)} + c_{35(s)}\alpha_{(s)}^{(l)}]\beta_{3(s)}^{(l)} + [e_{15(s)} + e_{35(s)}\alpha_{(s)}^{(l)}]\beta_{4(s)}^{(l)} \right) \\
G_{6l(s)} &= -\left([c_{14(s)} + c_{45(s)}\alpha_{(s)}^{(l)}]\beta_{1(s)}^{(l)} + [(c_{46(s)} + \sigma_{13(s)}) + (c_{44(s)} + \sigma_{33(s)})\alpha_{(s)}^{(l)}]\beta_{2(s)}^{(l)} + \right. \\
&\quad \left. [c_{45(s)} + c_{34(s)}\alpha_{(s)}^{(l)}]\beta_{3(s)}^{(l)} + [e_{14(s)} + e_{34(s)}\alpha_{(s)}^{(l)}]\beta_{4(s)}^{(l)} \right) \\
G_{7l(s)} &= -\left([c_{13(s)} + c_{35(s)}\alpha_{(s)}^{(l)}]\beta_{1(s)}^{(l)} + [c_{36(s)} + c_{34(s)}\alpha_{(s)}^{(l)}]\beta_{2(s)}^{(l)} + \right. \\
&\quad \left. [(c_{35(s)} + \sigma_{13(s)}) + (c_{33(s)} + \sigma_{33(s)})\alpha_{(s)}^{(l)}]\beta_{3(s)}^{(l)} + [e_{13(s)} + e_{33(s)}\alpha_{(s)}^{(l)}]\beta_{4(s)}^{(l)} \right) \\
G_{8l(s)} &= -\left([e_{13(s)} + e_{35(s)}\alpha_{(s)}^{(l)}]\beta_{1(s)}^{(l)} + [e_{36(s)} + e_{34(s)}\alpha_{(s)}^{(l)}]\beta_{2(s)}^{(l)} + \right. \\
&\quad \left. [e_{35(s)} + e_{33(s)}\alpha_{(s)}^{(l)}]\beta_{3(s)}^{(l)} - [\epsilon_{13(s)} + \epsilon_{33(s)}\alpha_{(s)}^{(l)}]\beta_{4(s)}^{(l)} \right) \\
G_{9l(p)} &= 0 \\
G_{10l(p)} &= 0 \\
G_{11l(p)} &= 0 \\
G_{12l(p)} &= 0
\end{aligned} \tag{2.35}$$

Non-trivial solutions of Equation (2.33) are obtained with:

$$Det[G] = 0 \tag{2.36}$$

It can be recalled that the values of the α and β_i have been previously calculated assuming a given velocity c_R , while it is actually still undetermined. In this respect, the only free

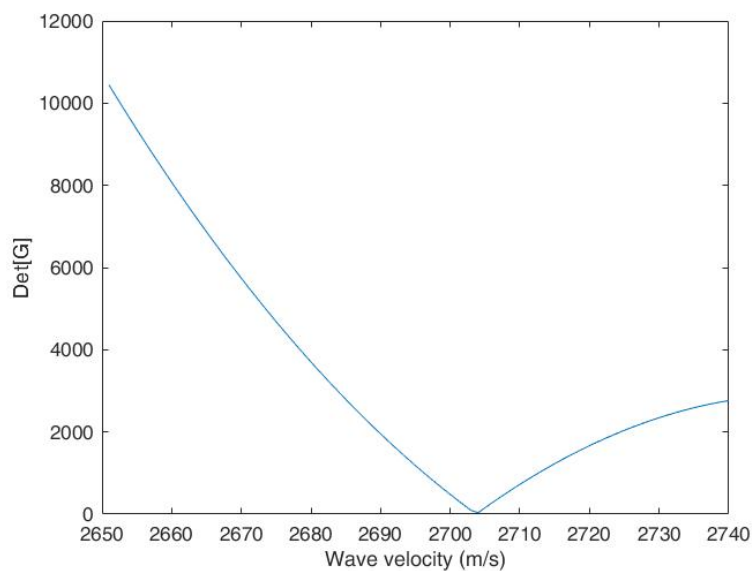


Figure 2.5: Variation of the determinant of Det[G] with potential wave velocities for the configuration described in Table (2.1)

Table 2.1: Table describing a configuration for an ZnO/SiO₂ SAW strain sensor

Piezoelectric material	Zinc Oxide (ZnO)
Piezoelectric layer thickness	6 μm
Substrate material	Fused silica (SiO_2)
Targeted wavelength	24.22 μm

parameter of (2.36) is the wave speed. Therefore the determination of c_R can be achieved numerically by (i) defining a list of potential velocities (ii) computing the values of α , β_i and $\text{Det}[G]$ for each velocity (iii) selecting the wave speed that minimizes the value of $\text{Det}[G]$.

The results of this procedure are shown in Figure 2.5, in a configuration described in Table 2.1, without initial stresses. With this configuration, $\text{Det}[G]$ tends towards 0 for a velocity of 2703 m/s.

Rayleigh wave velocity in strained media

The effects of applied strains on the wave velocity arise from three phenomena [66]:

- The elastic constants are related to the strains through the third-order elastic constants:

$$c_{ijkl} = c_{ijkl}^0 + c_{ijklmn}\varepsilon_{mn} \quad (2.37)$$

where c_{ijkl}^0 are the elastic constants at rest and c_{ijklmn} are the third-order elastic constants.

- According to the conservation of mass, the density varies with the normal strains:

$$\rho = \frac{\rho^0}{(1 + \varepsilon_{11})(1 + \varepsilon_{22})(1 + \varepsilon_{33})} \quad (2.38)$$

where ρ^0 is the density at rest.

- The applied strains generate a state of initial stresses represented by the tensor $\{\sigma\}$

Therefore the wave velocity under strain is calculated by replicating the previous approach while considering the changes in elastic constants, densities and initial stresses.

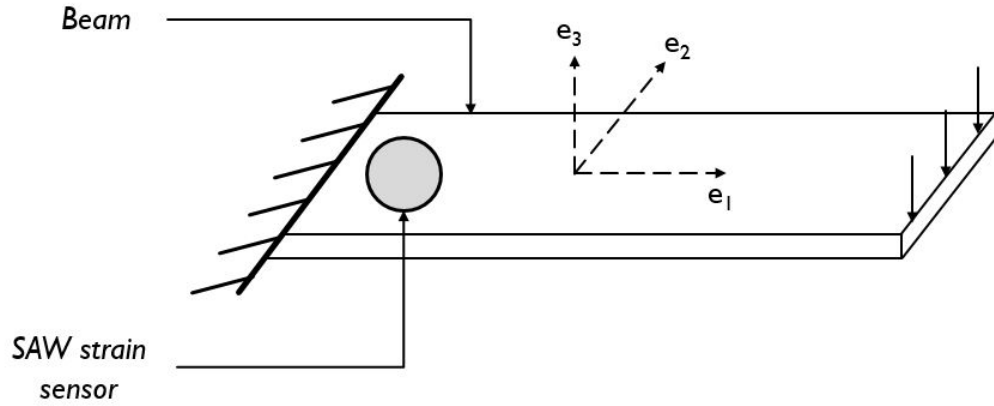


Figure 2.6: Representation of a SAW strain sensor on a loaded beam

2.2.4 Example

Zinc Oxide/ Fused silica device

A first example can be set by reproducing the results obtained in [65], where a sensor is bonded at the base of a loaded beam (Figure 2.6). The measured value is the normal strain along the e_1 axis: $\varepsilon_{11} = \varepsilon$. The strains induced by the load can be expressed directly as functions of ε for both layers as:

$$\begin{aligned}
 \varepsilon_{11} &= \varepsilon \\
 \varepsilon_{22} &= 0 \\
 \varepsilon_{33} &= \frac{s_{12}s_{33} - s_{13}^2}{s_{11}s_{33} - s_{13}^2} * \varepsilon \\
 \varepsilon_{12} &= 0
 \end{aligned}
 \tag{2.39}$$

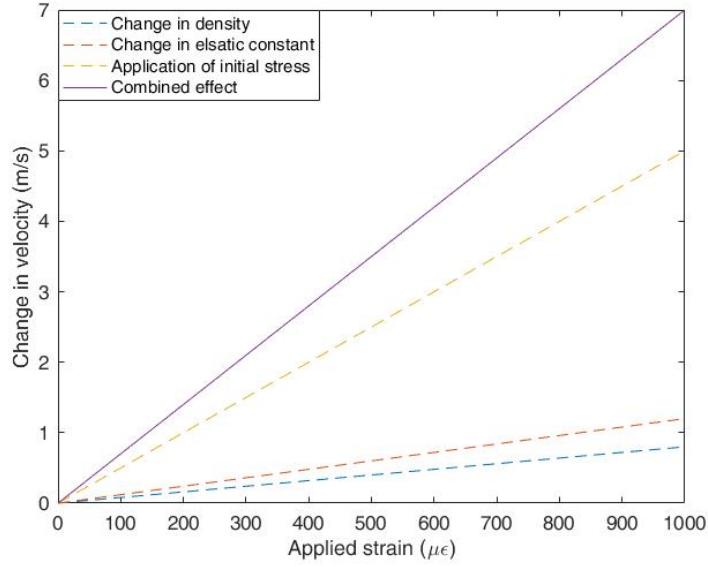


Figure 2.7: Computed variations of the SAW velocity under the strain ε due to the change in densities, elastic constants and initial stresses

where s represents the compliance coefficient.

The stresses are as well expressed for both layers as:

$$\begin{aligned}
 \sigma_{11} &= \frac{s_{33}}{s_{11}s_{33} - s_{13}^2} * \varepsilon \\
 \sigma_{22} &= -\frac{s_{13}}{s_{11}s_{33} - s_{13}^2} * \varepsilon \\
 \sigma_{33} &= 0 \\
 \sigma_{13} &= 0
 \end{aligned} \tag{2.40}$$

The characteristics of the sensor are given in Table 2.1.

In this example, the influence of the strain ε on the Rayleigh wave velocity has been detailed by separating the influence of (i) the change in elastic constants (ii) the change in density (iii) the initial stresses (Figure 2.7).

Furthermore the overall filtered frequency shift can be shown to be represented as a combination of the impact of the wavelength and velocity changes (Figure 2.8). Their combined effect provides a linear relationship between the applied strain ε and the frequency shift.

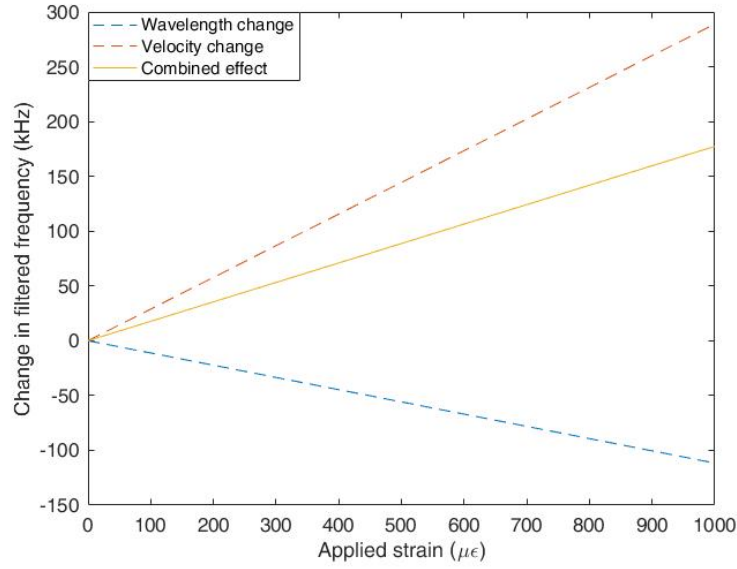


Figure 2.8: Computed frequency shift under strain ϵ due to the wavelength and velocity change

Its slope is a characteristic of the sensor and can be used in experiments to retrieve a value of the applied strain from the measured frequency change.

The calculated slope is $177 \text{ Hz}/\mu\epsilon$ and can be compared with the experimental value of $178 \text{ Hz}/\mu\epsilon$ found in [65].

It can be noted that the value of the characteristic slope does not only depend on the longitudinal strain $\epsilon_{11} = \epsilon$ and would be different if an additional transverse strain was also applied.

Zinc Oxide/ Flexible glass device

Table 2.2: Table describing a configuration for an ZnO/Flexible glass SAW strain sensor

Piezoelectric material	Zinc Oxide (ZnO)
Piezoelectric layer thickness	2, 2.7 or 3.3 μm
Substrate material	Corning Willow glass
Targeted wavelength	20 μm

The second example is inspired by the experimental results obtained in [64] where SAW strain sensors made of flexible glass with a Zinc Oxide piezoelectric layer have been tested.

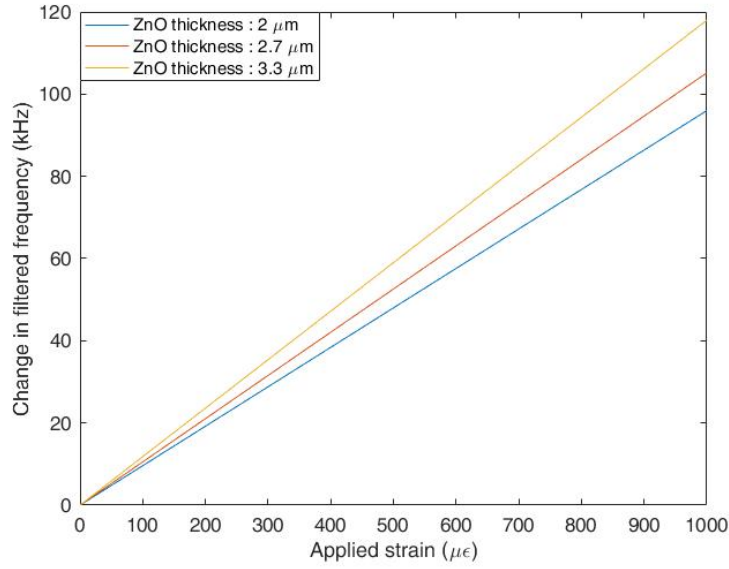


Figure 2.9: Computed frequency shift under strain ϵ for a ZnO/glass sensor

The details of the considered materials and dimensions are given in Table 2.2. The sensor is set in a similar position as in the previous examples and the state of strains and stresses can be obtained from Equations (2.39) and (2.40). The computed change in filtered frequency is given in Figure (2.9) for different thicknesses of piezoelectric Zinc Oxide (2, 2.7 and 3.3 $\mu\epsilon$).

The theoretical slopes "Frequency shift/Strain" are 96 Hz/ $\mu\epsilon$ for a piezo thickness of 2 μm , 105 Hz/ $\mu\epsilon$ for a thickness of 2.7 μm and 118 Hz/ $\mu\epsilon$ for a thickness of 3.3 μm . The experimental slopes obtained from the literature [64] give a slope of 85 Hz/ $\mu\epsilon$ for a thickness of 2 μm , 105 Hz/ $\mu\epsilon$ for a thickness of 2.7 μm and 136 Hz/ $\mu\epsilon$ for a thickness of 3.3 μm . Overall this example highlights the influence of the ratio "piezoelectric layer thickness/wavelength" on the characteristic slope.

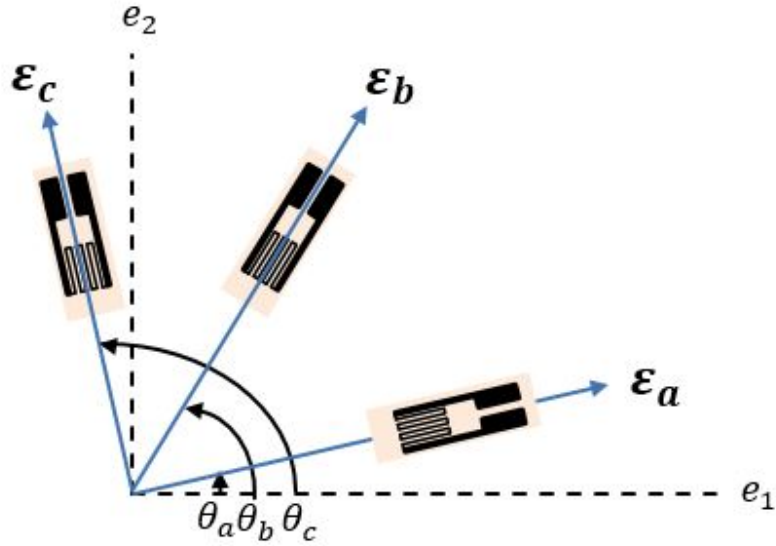


Figure 2.10: Representation of a strain rosette and of its associated orientation

2.3 SAW device for 2D strain sensing

2.3.1 Introduction to bi-dimensional strain sensing

The concept of strain measurement through an acoustic device can be extended to a bi-dimensional domain in a similar approach as what can be observed with resistive strain gages. Indeed, a common method to obtain the displacement state over a plane (two normal strains ε_{11} and ε_{22} , as well as a shear strain ε_{12}) relies on the use of strain rosettes [32]. These devices combine three resistive gages measuring strains ε_a , ε_b and ε_c , oriented in different directions defined by the angles θ_a , θ_b and θ_c relative to the e_1 axis (Figure 2.10). From the tensorial rotation rules, the values of ε_{11} , ε_{22} and ε_{12} can be recovered by inverting the following equations:

$$\begin{aligned}
 \varepsilon_a &= \frac{\varepsilon_{11} + \varepsilon_{22}}{2} + \frac{\varepsilon_{11} - \varepsilon_{22}}{2} \cos 2\theta_a + \varepsilon_{12} \sin 2\theta_a \\
 \varepsilon_b &= \frac{\varepsilon_{11} + \varepsilon_{22}}{2} + \frac{\varepsilon_{11} - \varepsilon_{22}}{2} \cos 2\theta_b + \varepsilon_{12} \sin 2\theta_b \\
 \varepsilon_c &= \frac{\varepsilon_{11} + \varepsilon_{22}}{2} + \frac{\varepsilon_{11} - \varepsilon_{22}}{2} \cos 2\theta_c + \varepsilon_{12} \sin 2\theta_c
 \end{aligned} \tag{2.41}$$

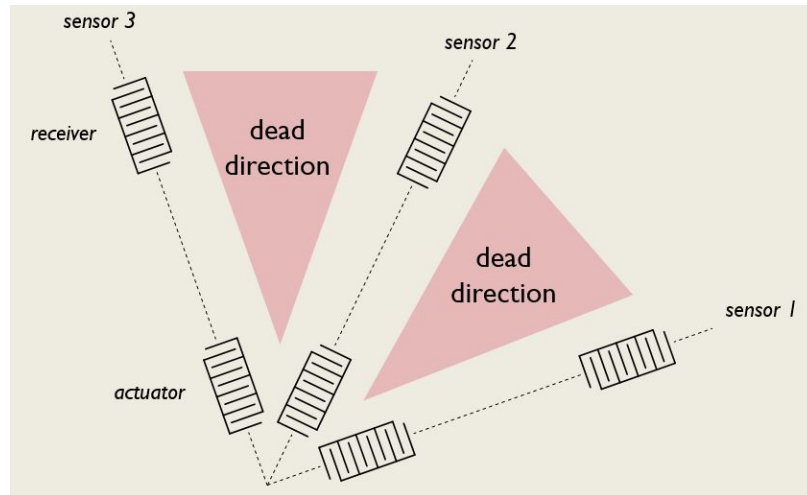


Figure 2.11: Representation of an acoustic device with three sets of IDTs for 2D strain measurement

By following the analogy with the resistive strain rosette, a bi-dimensional SAW strain sensor should compile three sets of IDTs (actuator and receiver) oriented in distinct directions and each providing one strain measurement (Figure 2.11). Such a device shows limitations under two aspects:

- Three different sets of IDTs are involved and therefore six different wire connections are required (as opposed to two connections for 1D devices), which goes against the demand of a lowly invasive device
- The surface waves only propagate on a reduced portion of the device while large sections oriented in "dead directions" (Figure 2.11) are unused. For similar dimensions, a lower power would be required to transmit the same amount of energy to the receivers if the device covered all directions.

For these reasons, the solution of Figure 2.11 is not optimal. A new framework that exploits more advanced electrode patterning is thus derived for strain sensing applications.

2.3.2 Design procedure of the Acoustic Wave Rosette

The objective is therefore to design a single acoustic transducer capable of actuating a SAW along three distinct orientations at given frequencies. These frequencies need to be separate

so that three peak shifts can be assessed to provide measurements in the required directions. The electrode distribution in the spatial domain is expressed by $f(\mathbf{x})$. Its two-dimensional Fourier Transform (2D-FT) $D(\mathbf{k})$ is a geometry-related term that acts upon the voltage reading on the piezoelectric layer. \mathbf{k} and \mathbf{x} are wavenumber and spatial vectors that can be expressed as:

$$\begin{aligned}\mathbf{k} &= k_1\mathbf{e}_1 + k_2\mathbf{e}_2 \\ \mathbf{x} &= x_1\mathbf{e}_1 + x_2\mathbf{e}_2\end{aligned}\tag{2.42}$$

The relation between $f(\mathbf{x})$ and $D(\mathbf{k})$ is provided by:

$$f(x_1, x_2) = \mathcal{F}^{-1}(D(k_1, k_2)) = \iint_{\mathbb{R}^2} e^{-j(k_1x_1+k_2x_2)} D(k_1, k_2) dk_1 dk_2\tag{2.43}$$

where \mathcal{F}^{-1} is the two-dimensional Inverse Fourier Transform (2D-IFT). Given the direct Wavenumber/Frequency relation (Equation 2.6), Equation 2.43 provides a frequency-dependent directivity for the SAW waves. It suggests the possibility of designing the electrode patterning to achieve a desired directionality for specific frequencies. The AWR design relies on that concept by defining the shape of the transducer in the wavenumber domain and using Equation 2.43 to retrieve the corresponding spatial distribution of active material.

The operation requirements of the 2D sensor are to generate three waves (*i*) in distinct directions, (*ii*) at different frequencies. These conditions can be translated in the wavenumber domain, where the distribution corresponds to three maxima associated with separate wave directions. Assuming an orthotropic hosting medium, the design provided as an example in Figure 2.12 features a tri-directional wavenumber distribution associated with three different frequencies, which are represented by different iso-frequency circles. With the wavenumber shape of the device in place, Equation 2.43 can be used to retrieve the spatial distribution of the electrodes through IFT procedures. Given the discrete distribution of the

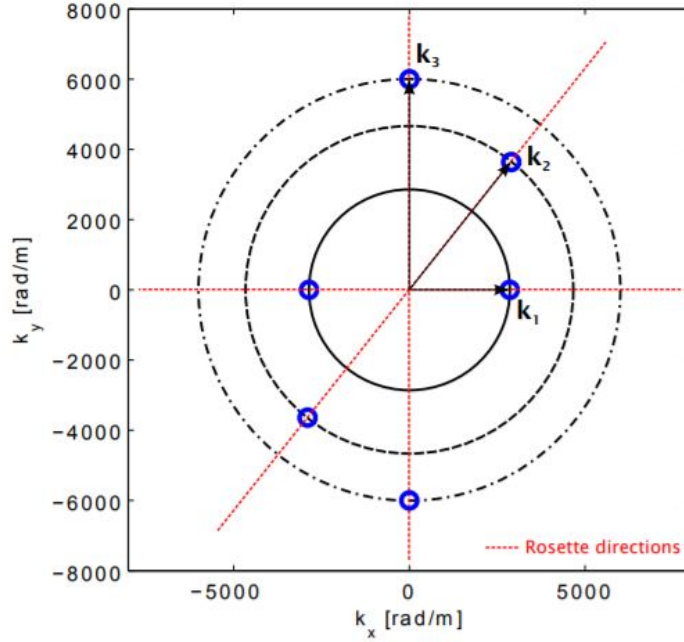


Figure 2.12: Schematic of the AWR directivity in the wavenumber domain

wavenumber maxima, the integrals can be replaced by a sum. The real value of the spatial distribution is given by:

$$f(x_1, x_2) = \sum_{p=1}^3 \cos(k_1^{(p)} x_1 + k_2^{(p)} x_2), p = 1, 2, 3 \quad (2.44)$$

where $k_1^{(p)}$ and $k_2^{(p)}$ ($p=1,2,3$) represent the projections on the \mathbf{e}_1 and \mathbf{e}_2 axis of the three targeted wavenumbers.

However, Equation 2.44 is associated with some limitations that prevent it from being directly used to provide the electrode design in the spatial domain. Indeed:

- The values of $f(x_1, x_2)$ are continuous while electrodes can only be represented by the values 1 (positive electrode), -1 (negative electrode) or 0 (absence of electrode).
- The electrodes are not spatially bounded

A simple strategy to overcome the first problem is to apply a thresholding procedure to $f(x_1, x_2)$, also called "quantization", during which a threshold value η is introduced as a

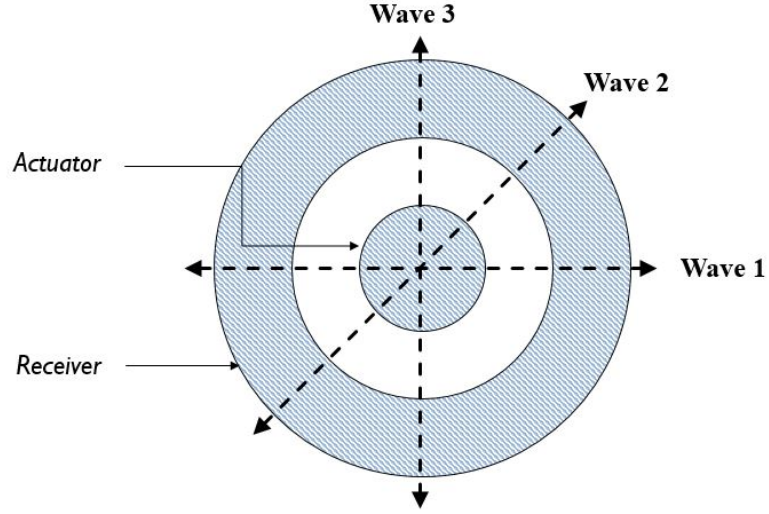


Figure 2.13: Schematic of the envisioned configuration of the AWR

given percentage of the maximum value of $f(x, y)$. The quantized version of the electrode distribution is given by:

$$\bar{f}(x_1, x_2) = \begin{cases} 1 & \text{if } f(x_1, x_2) > \eta \\ -1 & \text{if } f(x_1, x_2) < -\eta \\ 0 & \text{otherwise} \end{cases} \quad (2.45)$$

The value of η mostly depends on manufacturing constraints, since it defines the width of the electrodes as well as the spacing between them.

The second issue is targeted by defining a shape for the actuating and sensing part of the device. A circular shape is adapted for the actuator in order to generate waves in different directions. The sensor should encircle it to receive the waves and an annular shape can be considered (Figure 2.13). The electrode patterns of both the actuator and receiver should be identical to provide them with similar directional filtering properties.

2.3.3 Strain measurements

When the planar strains ε_{11} , ε_{22} and ε_{12} are applied to the AWR, the hosting medium of the electrode patterning is distorted. Assuming the strain is uniform under the device, the displacement field (u, v) associated with the Cartesian coordinate frame (x_1, x_2) is therefore expressed as:

$$\begin{aligned} u &= u_{,1}x_1 + u_{,2}x_2 \\ v &= v_{,1}x_1 + v_{,2}x_2 \end{aligned} \tag{2.46}$$

The linear relation between the strains and the deformations is given by:

$$\begin{aligned} \varepsilon_{11} &= u_{,1} \\ \varepsilon_{22} &= v_{,2} \\ \varepsilon_{12} &= \frac{1}{2}(u_{,2} + v_{,1}) \end{aligned} \tag{2.47}$$

The deformation of of the electrode pattern is expressed by including the material deformations in Equation (2.44):

$$f(x_1, x_2) = \sum_{p=1}^3 \cos(k_{01}^{(p)}(x_1 + u) + k_{02}^{(p)}(x_2 + v)), p = 1, 2, 3 \tag{2.48}$$

where $\{k_{01}^{(p)}, k_{02}^{(p)}\}$ denotes the location of one of the three maxima (p) of the electrode distribution in the wavenumber domain at rest. The frequency-dependent directivity of the device under strain is obtained by applying a 2D Fourier Transform, which is expressed as:

$$D(k_1, k_2) = \sum_{p=1}^3 j\pi [\delta(k_{01}^{(p)} + u_{,1}k_{01}^{(p)} + u_{,2}k_{02}^{(p)} - k_1)\delta(k_{02}^{(p)} + v_{,1}k_{01}^{(p)} + v_{,2}k_{02}^{(p)} - k_2) + \delta(k_{01}^{(p)} + u_{,1}k_{01}^{(p)} + u_{,2}k_{02}^{(p)} + k_1)\delta(k_{02}^{(p)} + v_{,1}k_{01}^{(p)} + v_{,2}k_{02}^{(p)} + k_2)] \quad (2.49)$$

where δ is the Dirac function. The locations of the maxima of the electrode distribution in the wavenumber domain under strain are obtained by maximizing each term of the sum in Equation (2.49):

$$\begin{aligned} k_{M1}^{(p)} &= k_{01}^{(p)} + u_{,1}k_{01}^{(p)} + u_{,2}k_{02}^{(p)} \\ k_{M2}^{(p)} &= k_{02}^{(p)} + v_{,1}k_{01}^{(p)} + v_{,2}k_{02}^{(p)} \end{aligned} \quad (2.50)$$

From there, the maximum wavenumbers need to be expressed in polar coordinates (with $k_M^{(p)}$ and $\theta_M^{(p)}$), as their radial shifts, rather than azimuthal, are in direct relations with the frequency shift observed under strain:

$$k_M^{(p)} = \sqrt{k_{M1}^{(p)2} + k_{M2}^{(p)2}} \quad (2.51)$$

After substituting 2.50 into 2.51, the variation of the radial wavenumber under strain is expressed as:

$$k_M^{(p)} = [(1 + u_{,1})^2 k_{01}^{(p)2} + u_{,2}^2 k_{02}^{(p)2} + 2(1 + u_{,1})u_{,2}k_{01}^{(p)}k_{02}^{(p)} + v_{,1}^2 k_{01}^{(p)2} + (1 + v_{,2})^2 k_{02}^{(p)2} + 2(1 + v_{,2})v_{,1}k_{01}^{(p)}k_{02}^{(p)}]^{1/2} \quad (2.52)$$

Assuming small displacements, Equation 2.52 can be linearized with:

$$\begin{aligned}
(1 + u_{,1})^2 &\approx (1 + 2u_{,1}) \\
u_{,2}^2 &\approx 0 \\
2(1 + u_{,1})u_{,2} &\approx 2u_{,2} \\
v_{,1}^2 &\approx 0 \\
(1 + v_{,2})^2 &\approx (1 + 2v_{,2}) \\
2(1 + v_{,2})v_{,1} &\approx 2v_{,1}
\end{aligned} \tag{2.53}$$

Therefore:

$$k_M^{(p)} = [(1 + 2u_{,1})k_{01}^{(p)2} + 2(u_{,2} + v_{,1})k_{01}^{(p)}k_{02}^{(p)} + (1 + 2v_{,2})k_{02}^{(p)2}] \tag{2.54}$$

The displacements can then be substituted by the strains through Equation (2.47):

$$k_M^{(p)} = [(1 + 2\varepsilon_{11})k_{01}^{(p)2} + 4\varepsilon_{12}k_{01}^{(p)}k_{02}^{(p)} + (1 + 2\varepsilon_{22})k_{02}^{(p)2}]^{1/2} \tag{2.55}$$

Equation (2.55) can be further developed by also transposing the maximum wavenumbers at rest from their azimuthal form ($k_{01}^{(p)}$ and $k_{02}^{(p)}$) into their radial expression ($k_0^{(p)}$ and $\theta_0^{(p)}$):

$$\begin{aligned}
k_{01}^{(p)} &= k_0^{(p)} \cos \theta_0^{(p)} \\
k_{02}^{(p)} &= k_0^{(p)} \sin \theta_0^{(p)} \\
k_0^{(p)} &= \sqrt{k_{01}^{(p)2} + k_{02}^{(p)2}}
\end{aligned} \tag{2.56}$$

Finally, the relation between the maximum radial wavenumbers at rest and under strains is obtained by injecting 2.56 into 2.55:

$$k_M^{(p)} = [(1 + 2\varepsilon_{11})k_0^{(p)2} \cos^2 \theta_0^{(p)} + 4\varepsilon_{12}k_0^{(p)2} \cos \theta_0^{(p)} \sin \theta_0^{(p)} + (1 + 2\varepsilon_{22})k_0^{(p)2} \sin^2 \theta_0^{(p)}]^{1/2} \tag{2.57}$$

which can be rearranged as:

$$\left(\frac{k_M^{(p)}}{k_0^{(p)}}\right)^2 = 1 + 2(\varepsilon_{11} \cos \theta_0^{(p)2} + \varepsilon_{22} \sin \theta_0^{(p)2} + \varepsilon_{12} \sin 2\theta_0^{(p)}) \quad (2.58)$$

Finally, introducing Equation 2.6 leads to:

$$\left(\frac{f_M^{(p)}}{f_0^{(p)}}\right)^2 \left(\frac{c_0^{(p)}}{c_\varepsilon^{(p)}}\right)^2 = 1 + 2(\varepsilon_{11} \cos \theta_0^{(p)2} + \varepsilon_{22} \sin \theta_0^{(p)2} + \varepsilon_{12} \sin 2\theta_0^{(p)}), p = 1, 2, 3 \quad (2.59)$$

where $f_M^{(p)}$ is the p-th filtered frequency under stress, $f_0^{(p)}$ is the p-th filtered frequency at rest, $c_\varepsilon^{(p)}$ is the wave velocity at under strain associated with p-th filtered frequency and $c_0^{(p)}$ is the wave velocity at rest associated with p-th filtered frequency. In subsection 2.2.3, the Rayleigh wave velocity was calculated for a wave propagating in the e_1 direction. However, $c_\varepsilon^{(p)}$ is a velocity associated with the direction $e_1^{(p)}$, defined in Figure 2.14. In the coordinate frame $\{e_1^{(p)}, e_2^{(p)}\}$, $c_\varepsilon^{(p)}$ is calculated under the stresses and strains states $\{\sigma^{(p)}\}$ and $\{\varepsilon^{(p)}\}$, that can be defined for orthotropic materials as:

$$\begin{aligned} \begin{bmatrix} \sigma_{11}^{(p)} & \sigma_{12}^{(p)} \\ \sigma_{12}^{(p)} & \sigma_{22}^{(p)} \end{bmatrix} &= \begin{bmatrix} \cos \theta_0^{(p)} & \sin \theta_0^{(p)} \\ -\sin \theta_0^{(p)} & \cos \theta_0^{(p)} \end{bmatrix} \begin{bmatrix} \sigma_{11} & \sigma_{12} \\ \sigma_{12} & \sigma_{22} \end{bmatrix} \begin{bmatrix} \cos \theta_0^{(p)} & -\sin \theta_0^{(p)} \\ \sin \theta_0^{(p)} & \cos \theta_0^{(p)} \end{bmatrix} \\ \begin{bmatrix} \varepsilon_{11}^{(p)} & \varepsilon_{12}^{(p)} \\ \varepsilon_{12}^{(p)} & \varepsilon_{22}^{(p)} \end{bmatrix} &= \begin{bmatrix} \cos \theta_0^{(p)} & \sin \theta_0^{(p)} \\ -\sin \theta_0^{(p)} & \cos \theta_0^{(p)} \end{bmatrix} \begin{bmatrix} \varepsilon_{11} & \varepsilon_{12} \\ \varepsilon_{12} & \varepsilon_{22} \end{bmatrix} \begin{bmatrix} \cos \theta_0^{(p)} & -\sin \theta_0^{(p)} \\ \sin \theta_0^{(p)} & \cos \theta_0^{(p)} \end{bmatrix} \end{aligned} \quad (2.60)$$

As a result, in Equation 2.59, for each filtered frequency (p=1,2,3):

- ε_{11} , ε_{22} and ε_{12} are strains applied on the sensor.
- $\theta_0^{(p)}$, $f_0^{(p)}$ and $c_0^{(p)}$ depend on the material characteristics and thicknesses, as well as the electrode pattern. They are assigned at the design stage.
- $c_\varepsilon^{(p)}$ depends on the state of strains and stresses along the direction associated with $\theta_0^{(p)}$.

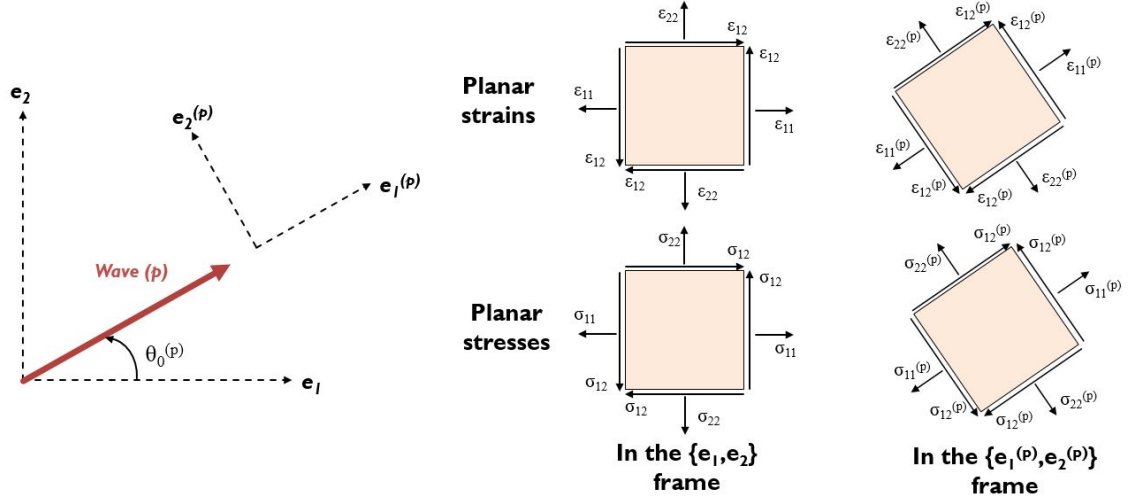


Figure 2.14: Representation of the change of the coordinate frame as well as the states of strains and stresses with the angle $\theta_0^{(p)}$

- $f_M^{(p)}$ is the filtered frequency under strain that is tracked.

2.3.4 Example

Table 2.3: Table describing a configuration for an ZnO/Flexible glass SAW 2D strain sensor

Piezoelectric material	Zinc Oxide (ZnO)
Piezoelectric layer thickness	$2 \mu\text{m}$
Substrate material	Corning Willow glass
Wavelength associated with the first filtered frequency	$12 \mu\text{m}$
Wavelength associated with the second filtered frequency	$16 \mu\text{m}$
Wavelength associated with the third filtered frequency	$20 \mu\text{m}$
Angle associated with the first filtered frequency	0°
Angle associated with the second filtered frequency	45°
Angle associated with the third filtered frequency	90°

The analytical derivation presented above has been applied to simulate the performance of a ZnO/Flexible glass AWR measuring strains on a loaded beam. The experimental configuration has been introduced in Figure (2.6) and the state of strains and stresses were described in (2.39) and (2.40). Its electrode pattern is described by the three wavelengths and angles associated with the filtered frequencies. The material characteristics, thicknesses and pattern attribute are described in Table (2.3). The shape of the electrodes is represented

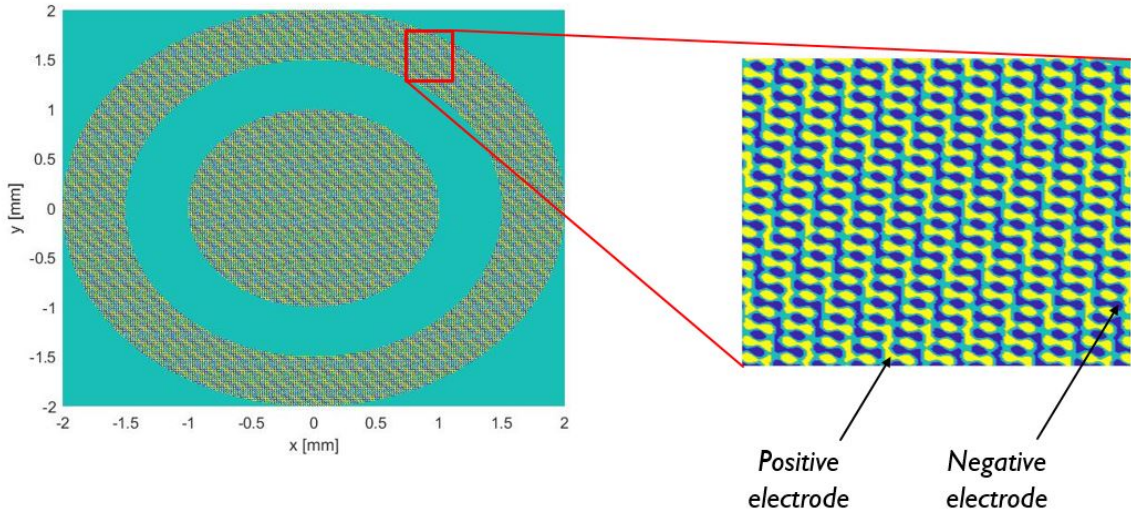


Figure 2.15: Representation of an AWR with the characteristics described in table 2.3

in Figure 2.15 for an actuator with a 2mm-diameter and a receiver with a 3mm-inner diameter and a 4-mm outer diameter.

Assuming that the direction associated with the 0° angle coincides with the e_1 axis, the shifts obtained for the three frequencies are given in Figure 2.16 where the x-axis represents the applied strain along the e_1 axis.

2.4 Conclusion

In this chapter, the concept of frequency filtering by Interdigital Transducers for SAW generation and reception has been introduced as well as a possible application with one-dimensional strain sensing. The relation between the applied deformations and the frequency shift has been theoretically derived and verified through two examples.

The design approach first introduced by Carrara [31] to pattern the electrodes of a device capable of measuring the two normal strains as well as the shear strain in a plane has been presented. The method used to measure the shifts of the three filtered frequency has been given and applied through an example.

The next chapter will tackle the manufacturing and experimental testing of 1D and 2D SAW strain sensors, as well as a comparison with the expected theoretical results.

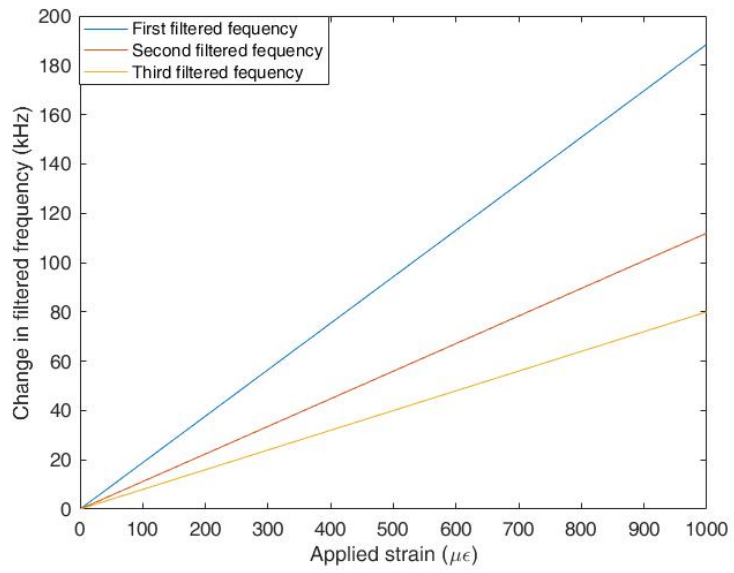


Figure 2.16: Frequency shifts associated with the AWR described in Table 2.3 on a loaded beam

CHAPTER 3

STRAIN SENSOR MANUFACTURING AND TESTING

3.1 Overview

After introducing the designing method for the AWR and the theoretical Frequency/Strain relations in Chapter 2, this chapter will first focus on the manufacturing approach and completion of the 1D and 2D devices. Indeed SAW sensors fall within the category of Microelectromechanical Systems (MEMS) that are defined by their low characteristic dimensions (in the range of micrometers). This miniaturization is necessary to ensure the low-power operations as well as the possibility to measure local strains, but requires a great precision during the fabrication process.

Microfabrication gathers a collection of techniques intended to add and pattern thin layers with the necessary precision. The operations are carried out in a cleanroom facility to avoid the sample contamination by dust. A full protocol has been set and executed to manufacture the 1D and 2D devices before testing their directional frequency filtering capabilities.

3.2 Material and design selections in 1D

The chosen configuration follows the typical layer arrangement for SAW sensors made of a substrate, a piezoelectric layer and metal electrodes. The selected materials are:

- for the substrate : Corning Willow glass, which has been used at multiple occasions in the literature for SAW strain sensors [64, 22, 12]. It is a flexible glass that can sustain strains up to $3000 \mu\epsilon$ without breaking and has a thickness of $200 \mu\text{m}$
- for the piezoelectric layer: Aluminum Nitride (AlN), which is an orthotropic material that has also been previously adopted for strain sensors [15, 30] where it was used

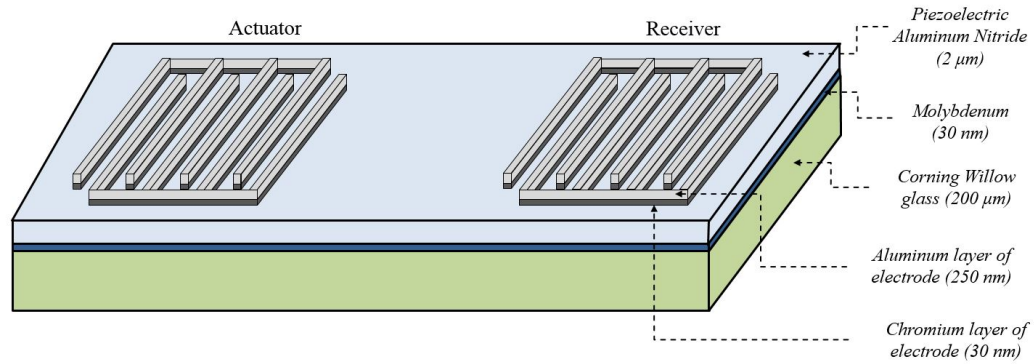


Figure 3.1: Representation of the layer structure used for the SAW strain sensor

for accurate measurements of small deformations. The adopted thickness is $2 \mu\text{m}$.

- for the electrodes: Aluminum, which can be easily deposited and patterned in the microfabrication facilities while providing great electrical conductivity properties. Its thickness is 250 nm.

In addition to the latter, the following materials are required for manufacturing purposes:

- Molybdenum (20nm), between the substrate and piezoelectric layers: it is used as a seed layer upon which the piezoelectric AlN layer can be grown
- Chromium (30nm) under the aluminum electrodes: it is used as a bonding layer as its significant adhesion properties compensate the limited ones of the aluminum. It needs to be patterned in the shape of the electrodes to avoid an electrical connection between the fingers.

The overall structure is represented in Figure 3.1.

The shape of the generated wave depends on the electrode pattern actuating the piezoelectric layer. As expressed in Subsection 2.2.1, Interdigital Transducers (IDTs) provide the required one-dimensional filtering capabilities. For both the actuator and receiver, the electrodes are split into positive and negative sections patterned as interlocking comb-shaped

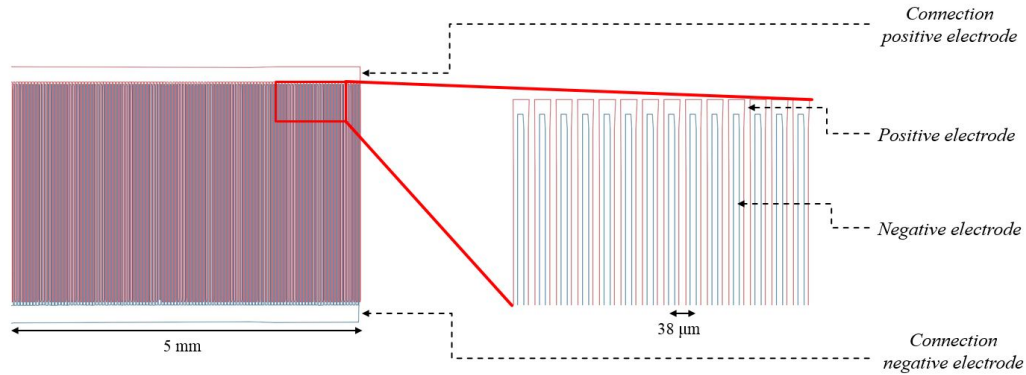


Figure 3.2: Layout of the electrodes in the actuator or receiver

lines, also called fingers. All the fingers of one section are connected together and the layout of the manufactured electrodes for the actuator (or receiver) is illustrated on Figure 3.2. In addition, a contact pad was patterned for each electrode to allow wire bonding. The wavelength λ associated with the manufactured sensor is $38 \mu\text{m}$ and the total width of the actuator (or receiver) is 5 mm. In this configuration, the expected wave velocity c_R and filtered frequency f_r are respectively $3420 \text{ m}\cdot\text{s}^{-1}$ and 90 MHz.

3.3 Manufacturing

The manufacturing approach is dictated by the critical dimensions of the electrodes. Indeed the width of one electrode, as well as the distance between two fingers, equals to $\lambda/4$, or $9.5 \mu\text{m}$. Such a fabrication precision can only be achieved with the microfabrication methods that are performed in cleanroom facilities. All the manufacturing steps introduced and described in this section have been carried out in the Marcus Inorganic Cleanroom at the Georgia Institute of Technology.

3.3.1 Introduction to microfabrication and photolithography

The microfabrication approach for SAW devices mainly relies on three stages:

- The layer deposition
- The electrode patterning

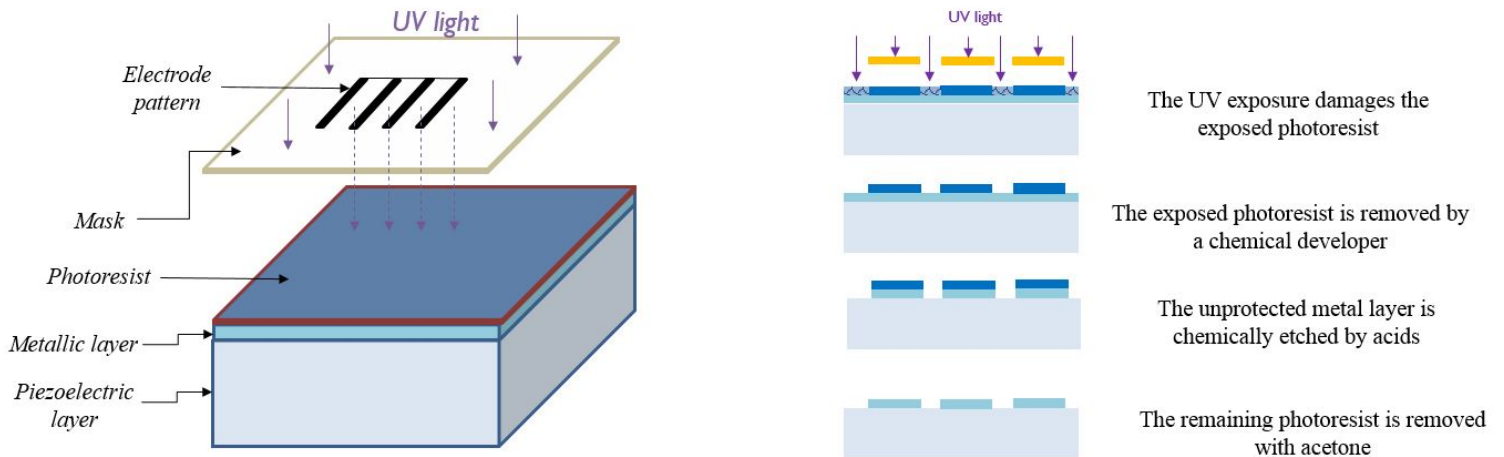


Figure 3.3: Representation of the concept of photolithography and the different steps for electrode patterning

- The layer etching

During the first step, piezoelectric layer and metal layers are deposited upon the substrate. However, the main challenge in this manufacturing process happens in the patterning phase since a connection between a positive and negative finger would render the device inoperative. The required modeling precision is reached with photolithography [68], which is a process using UV light to transfer a pattern printed on a mask onto a photosensitive material called photoresist.

Liquid photoresist is first dropped over the metallic layers of the device and spread uniformly during a spin-coating step. The Coriolis force created by the rotation ejects the top layer and only a thin film of a thickness determined by the spinning velocity remains on the sample. A baking stage on a hotplate is then applied to decrease the solvent concentration and harden this film.

The sample is next placed in a mask aligner, where intense UV light is projected towards the photoresist through a photomask. These masks are transparent plates (usually made of fused silica) covered by an opaque pattern that locally prevents the light from crossing. The type of photoresist defines the action of UV light:

- Positive photoresist is degraded by light

- Negative photoresist is strengthened by light

The time of exposure t_{exp} is determined by:

$$t_{exp} = E_{exp}/I_{exp} \quad (3.1)$$

where E_{exp} is the exposure dose (J/cm^2) that depends on the photoresist thickness and is provided in material data sheets. I_{exp} is the light intensity characteristic of the mask aligner. The "weak" region is then dissolved by an adapted chemical called "developer". Therefore, for a positive photoresist, the pattern printed on the photomask needs to be identical to the shape of the electrodes. The development time can be deduced from process parameters tables or by visual inspection during the step. The sample needs to be rinsed with deionized water immediately after to put an end to the chemical reaction.

Complications may mainly happen if the photoresist is underexposed or underdeveloped, which would result in the presence of a remaining thin layer omnipresent on the device. As a result, it is common practice to slightly overexpose and overdevelop the photoresist. The remaining photoresist layer is used to protect the locations of the electrodes. Indeed, the sample is then immersed in an acidic bath that etches the unprotected metal layers. Finally, the remaining photoresist is removed by acetone.

The main stages of the patterning and etching steps are shown in Figure 3.3. At the end of the process, the piezoelectric layer should be unveiled everywhere except at the positions of the metallic electrodes.

3.3.2 Manufacturing steps

All the specific manufacturing steps for the 1D SAW strain sensor are introduced in Figure 3.4.

The glass wafer is first cleaned during 30 seconds by plasma oxygen in a Reactive-Ion Etching (RIE) equipment in order to remove the potential dirt that could reduce the adhe-

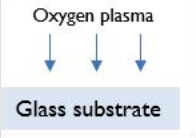

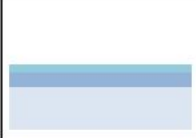
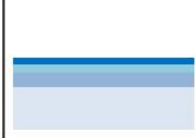
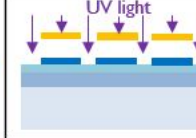
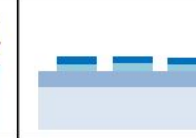
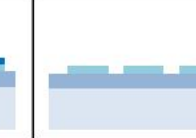


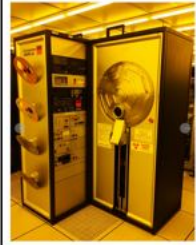




						
Plasma oxygen etching (preliminary cleaning)	Aluminum Nitride magnetron sputtering	Chromium and Aluminum deposition by e-beam evaporation	Photoresist deposition by spin-coating	Photoresist exposure and development	Chemical etching of the metal layers	Photoresist stripping
						
Vision 320 RIE	CtrLayer SDS – AlN Sputtering system	CHA Modified Mar-40 E-beam evaporator 2	SCS G3 Spin Coater+ Microposit S1813	Heidelberg MLA 150 Maskless aligner+ Microposit MF-319	Fume hood + aluminum and chromium etchant	Fume hood + acetone

Figure 3.4: Manufacturing steps for the 1D SAW strain sensor

sion between the glass and the other materials. A layer of Molybdenum (30 nm) is then deposited by reactive magnetron sputtering as a seed where AlN can grow. The same sputtering tool is used to lay AlN, using a pure Aluminum target in an Ar- N_2 atmosphere. The piezoelectric properties associated with the crystals orientation result from specific sputtering parameters [69]. The Chromium (30 nm) and Aluminum (250 nm) are deposited afterwards. The process used is electron-beam (or e-beam) evaporation, where accelerated electrons are directed towards a metal target, causing it to evaporate and re-solidify uniformly over the substrate.

A film of photoresist Microposit S1813 [70] is then spin-coated at a rotation speed of 4000 rpm, leaving a layer with a theoretical thickness of $1.4 \mu\text{m}$. After a softbake on a hotplate (115°C during one minute), the photoresist is exposed to UV light (365 nm wavelength) by a maskless aligner (Heidelberg MLA 150). Unlike mask aligners that protect the desired patterns with the opaque section of a mask, maskless aligners project UV light through a narrow beam directed towards the locations that need to be exposed. Their main advantage

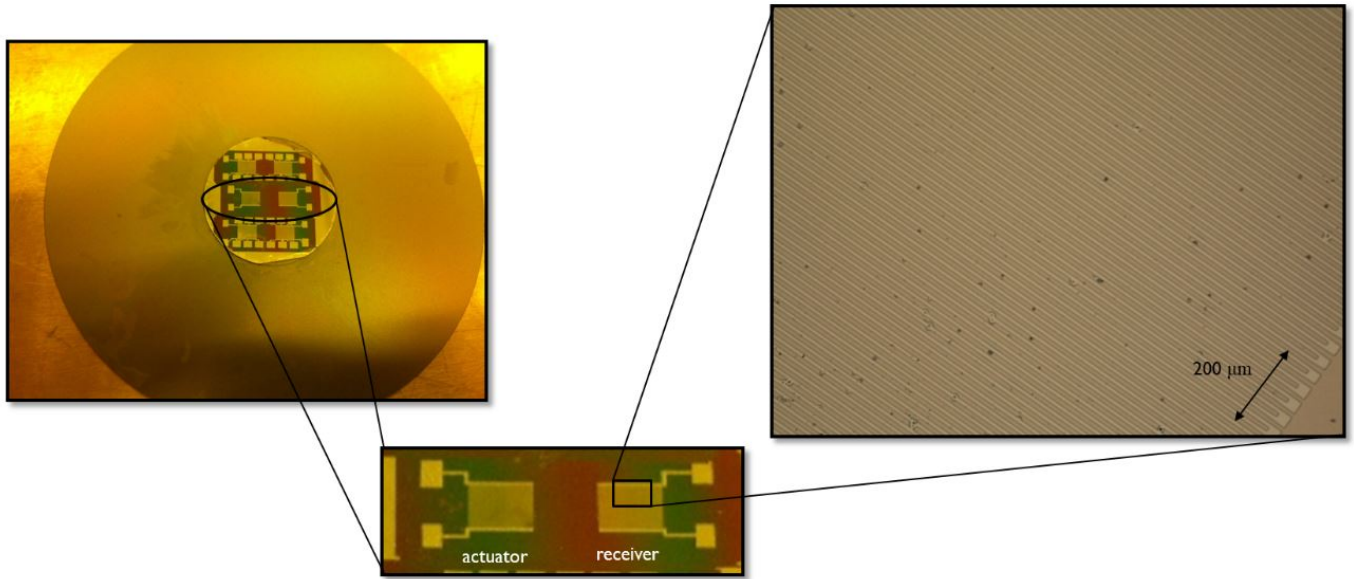


Figure 3.5: Pictures and microscopic view of the manufactured 1D device

comes from the flexibility in the electrode pattern as it is unnecessary to manufacture a mask for every new design. A drawback could be the additional time required for the UV beam to travel over the whole sample. However, given the small dimensions of the glass substrate, the exposure time was limited to 5 minutes. The exposed photoresist has then been developed in a bath of Microposit MF-319 [71] diluted into water at a 1:3 ratio during 30 seconds.

After a thorough rinsing with deionized water to stop the chemical reaction caused by the developer, the sample is immersed in a bath of Aluminum etchant type-A during which the unprotected aluminum is attacked. The etching time can be determined visually as the chromium layer unveiled at the end of this step is darker. After rinsing again the sample, the unprotected chromium is removed by an adapted etching chemical. At this stage, the electrodes have been patterned and there is no electrical connection remaining between them. Finally, the photoresist can be stripped by acetone.

3.3.3 Manufactured 1D device

The manufactured device is shown in Figure 3.5. Rectangular contact pads have been added along each electrode to allow wire bonding.

3.4 Characterization of the 1D device

3.4.1 Experimental setup

The manufactured device has been bonded at the base of an aluminum beam by a two-component epoxy adhesive (Loctite E-20 HP). Wires have been attached on each of the contact pads with conductive silver epoxy (MG Chemicals 8331 Silver Epoxy Adhesive) and are connected to SMA connectors, designed to handle electric signals up to the range of gigahertz (GHz).

The actuator is powered by a Pulser-Receiver (Olympus 5900-PR) capable of generating pulse signals associated with a bandwidth equal to 200 MHz. The signal obtained from the receiver is first magnified by the amplifier of the Olympus 5900-PR, before being collected by an oscilloscope (Tektronix TDS 5034B). The data is then transferred by a GPIB cable to a computer in order to analyze its frequency content. The connection between the pulser and the amplifier to the SMA connectors is ensured by SMA/BNC cables.

Two resistive one-dimensional strain gages have also been bonded along the SAW sensor (on both side of the beam) to provide reference values (Figure 3.6.a). Both gages have an identical resistance value R at rest. When a force is applied on top of the beam, the upper gage becomes under tension (under strain $+\varepsilon$) while the bottom one is under compression (under strain $-\varepsilon$). The value of their internal resistance changes respectively by $+\Delta R$ and $-\Delta R$ and this variation is measured through an electrical circuit called Half-Wheatstone bridge (Figure 3.6.b). Under this configuration, the gages are connected to two additional resistances R and an output voltage V_{out} is measured across the bridge. The applied strain

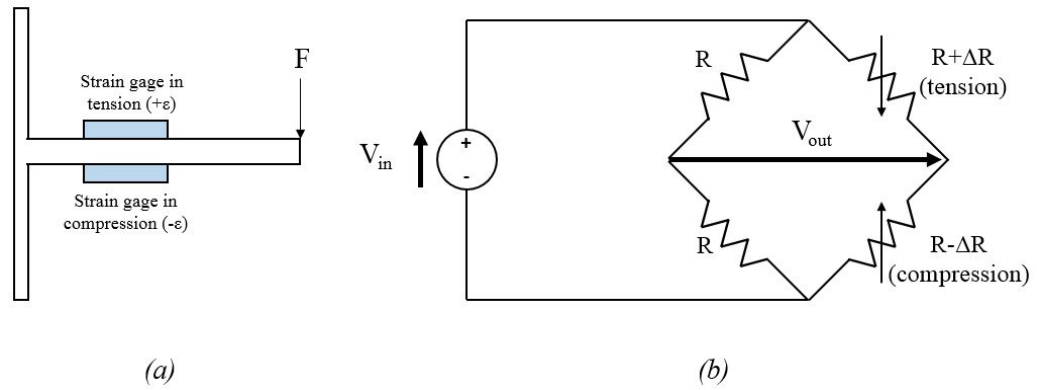


Figure 3.6: Representation the resistive strain sensors on the beam (a) and of the Half-Wheatstone bridge (b)

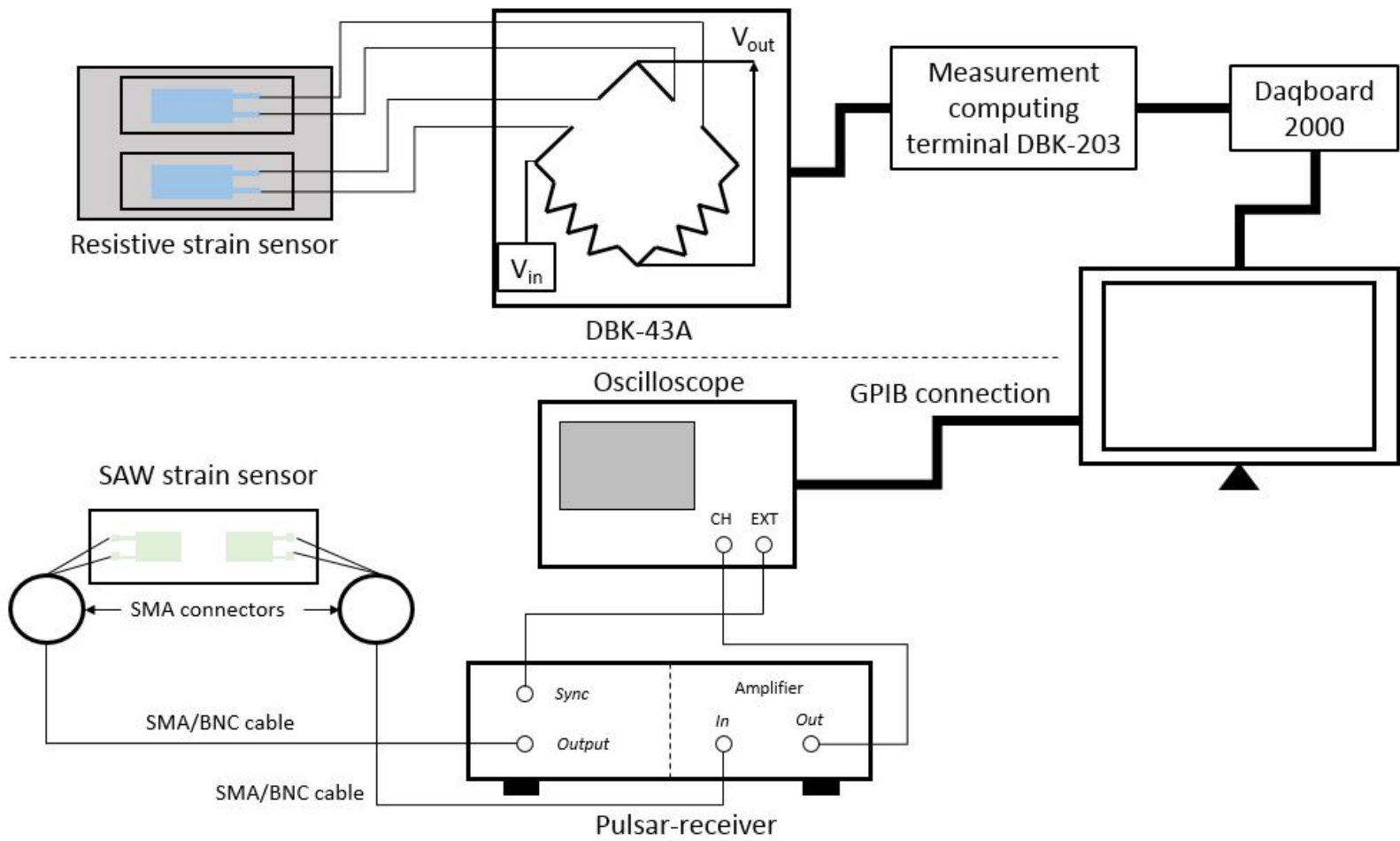


Figure 3.7: Representation of the measurement setup for SAW and resistive strain gages

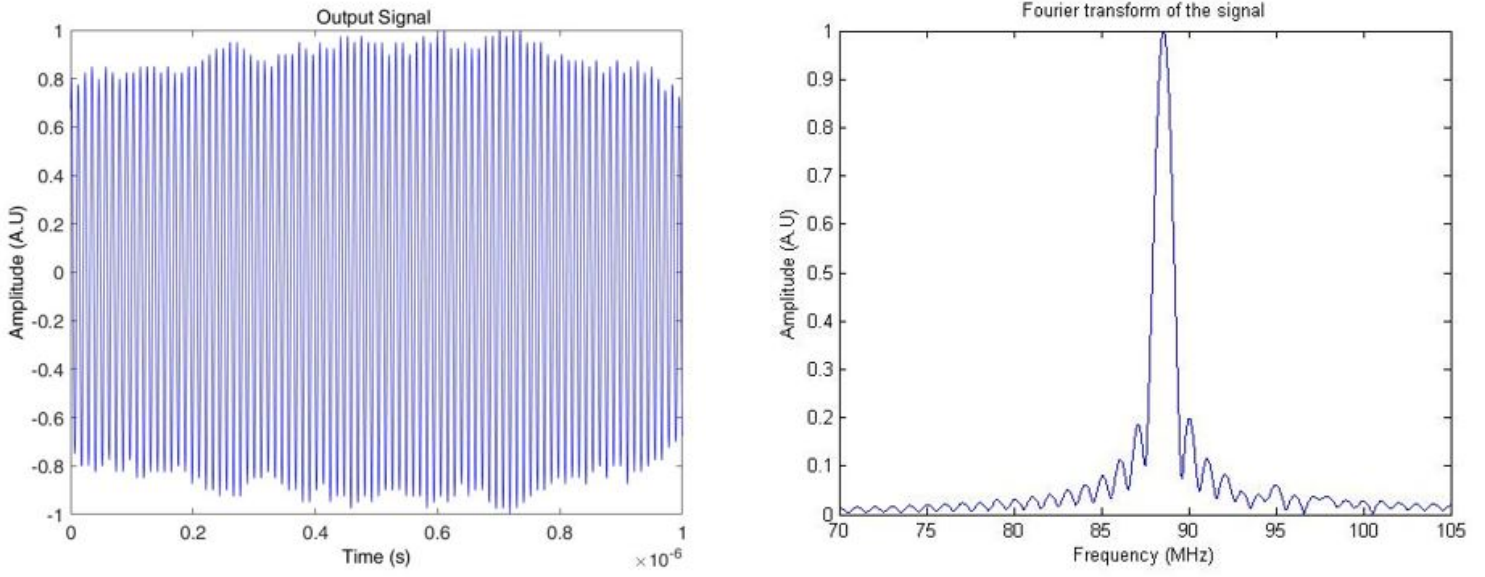


Figure 3.8: Experimental output signal (left) and associated spectrum (right) obtained from the manufactured 1D device

ε is therefore given as:

$$\varepsilon = -2 \frac{V_{out}}{V_{in}} \frac{1}{GF} \quad (3.2)$$

where V_{in} is the input voltage and GF is the gage factor, which defines the sensitivity of the gage to strains and is provided by the manufacturer.

The gages are powered and conditioned by a module DBK 43A and the measurement terminal DBK 203 is used to adjust the electric output to the characteristics of the strain gages. A data acquisition board DaqBoard 2000 communicates between the computer and the adapter.

The overall setup for parallel strain measurements with the SAW and resistive sensors is represented in Figure 3.7

3.4.2 Experimental frequency filtering capabilities

Under the actuation of the pulsar, the input signal for the SAW sensor provides a wideband excitation while keeping the signal footprint limited in the time domain. The output signal is obtained as the difference of electric potentials between the positive and negative elec-

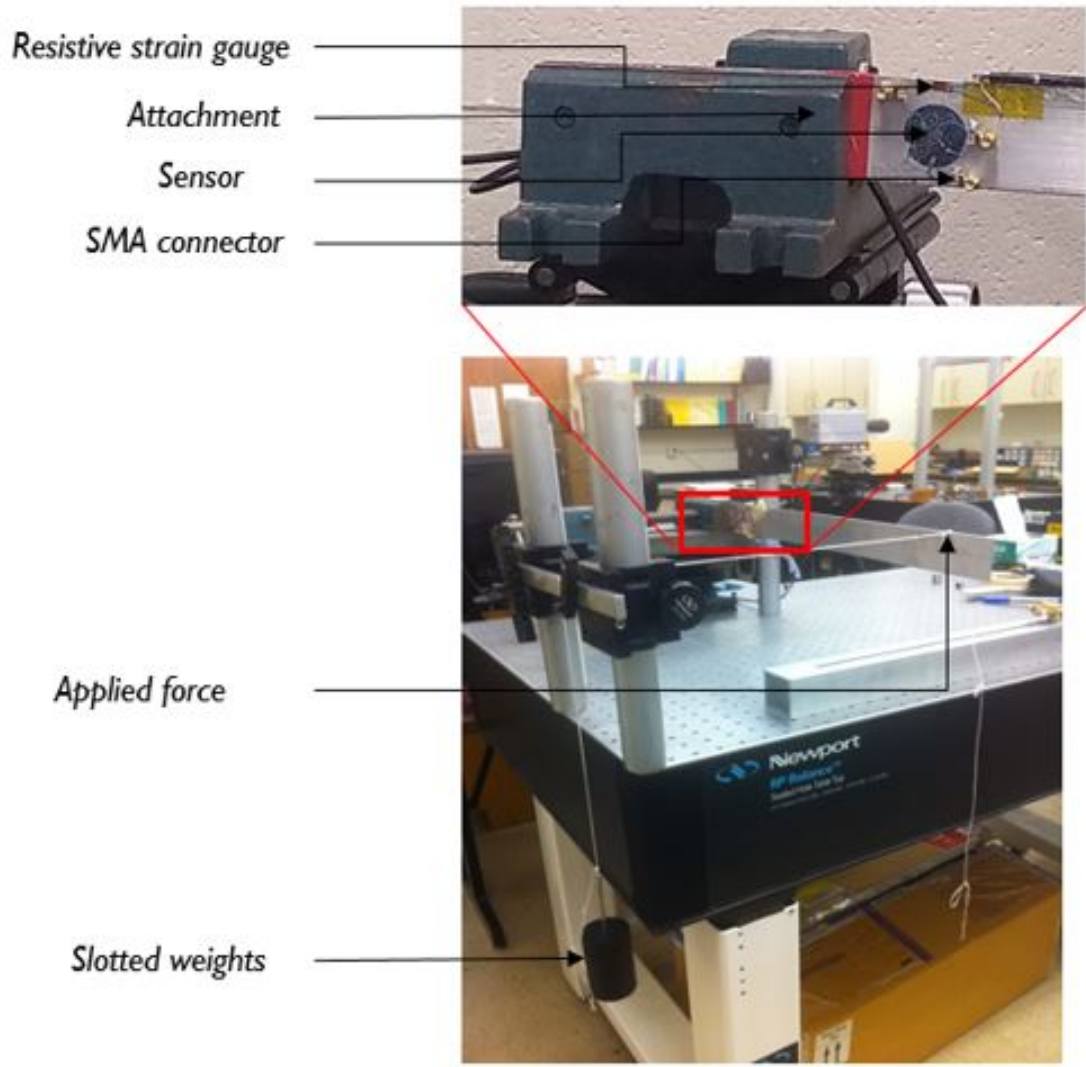


Figure 3.9: Experimental setup used for strain measurements over a loaded beam

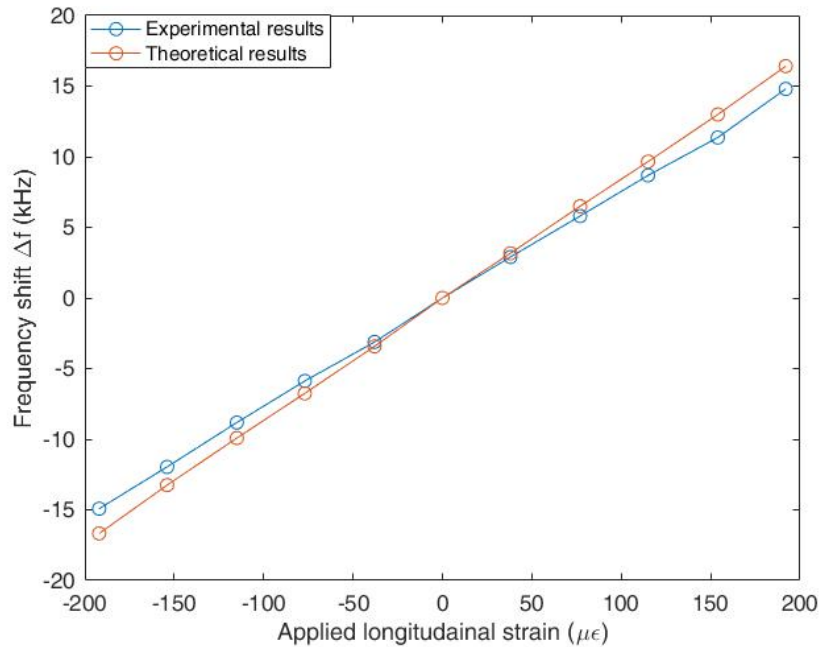


Figure 3.10: Experimental and theoretical frequency shifts under strain for the 1D strain sensor

trodes of the receiver.

The time-domain signal is transformed into the frequency domain by means of a Fourier Transform (FT). It can be noted that a fine frequency resolution is needed in order to achieve measurements of the filtered frequency shift at an acceptable precision. In the case of a conventional Fast Fourier Transform (FFT) procedure, the resolution would be limited by the brevity of the received signal obtained from a pulse input. As a result, a Chirp-Z-Transform (CZT) is used instead, which allows the computation of the Fourier Transform over a limited and selectable band and improves the signal spectrum resolution [72].

The experimental output signal and the associated Fourier Transform are introduced on Figure 3.8. The frequency spectrum is characterized by a main peak centered on 88 MHz and multiple side peaks due to the finite dimensions of the device.

3.4.3 Experimental relation Frequency/Strain

The configuration introduced in Figure 2.6 has been used to evaluate the strain measurements capacities of the device. Indeed, the aluminum beam has been clamped near the sensor and loaded by slotted weights on its other extremity. A reference value for the longitudinal displacement is provided by resistive gages, while the remaining strain and stress fields have been given in Equations 2.39 and 2.40. The overall configuration is shown on Figure 3.9.

The oscilloscope and data transmission towards the computer is remotely controlled through Keysight Control Expert software. For each strain applied, the position of the main peak is computed and the value is averaged over 100 measurements. A frequency shift Δf is therefore obtained as:

$$\Delta f = f_\varepsilon - f_0 \quad (3.3)$$

where f_ε and f_0 are the filtered frequency under a longitudinal strain ε and at rest.

The experimental results are then compared with theoretical ones (Figure 3.10).

The characteristic slope Frequency/Strain of the device is deduced by applying a linear regression to the experimental results. It equals $77 \text{ Hz}/\mu\varepsilon$. The deviation of the results from the slope are expressed by the coefficient of determination R^2 , which equals to 0.9998.

The slope given by the theoretical model equals to $85 \text{ Hz}/\mu\varepsilon$.

3.5 Extension to the 2D device

After exploring the manufacturing and testing of the 1D SAW strain sensor in the previous section, these steps will be repeated for the two-dimensional extension of the device: the Acoustic Wave Rosette.

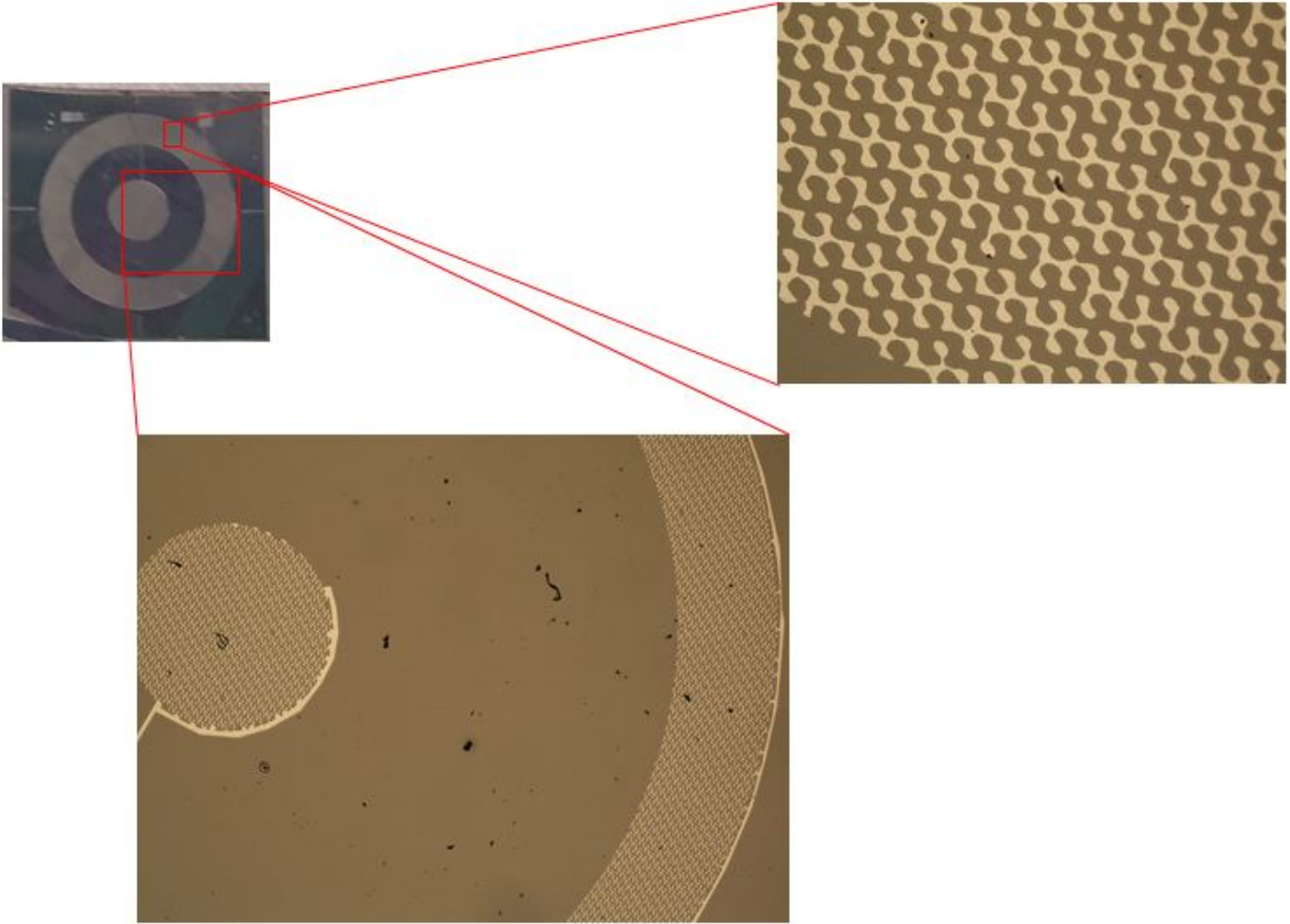


Figure 3.11: Pictures and microscopic views of the manufactured AWR

3.5.1 Manufactured device

The layer disposition and manufacturing process for the Acoustic Wave Rosette device are identical to the ones used for the one-dimensional sensor. The main difference lies in the electrode patterns, that have been defined in the subsection 2.3.2. Their locations are described by Equation 2.44 and the quantization process 2.45.

The three targeted filtered frequency have been 130, 115 and 100 MHz and the associated propagation angles are 0° , 45° and 90° . The thickness of the piezoelectric layer has been increased to $3 \mu\text{m}$ in order to improve the slope "Frequency/Strain". For this design, the velocities and wavelengths associated with the three waves are respectively 3488 m.s^{-1} and $26 \mu\text{m}$, 3463 m.s^{-1} and $30 \mu\text{m}$, 3447 m.s^{-1} and $34 \mu\text{m}$.

As shown in Figure 2.15, the theoretical electrode patterns are characterized by multiple unconnected patches through which the electrical current cannot propagate. Additional connections between the patches and around the actuator/receiver are used to unify the positive and negative electrodes. Besides, the manufacturing process of the AWR has been unsuccessful because of electrical connections between the positive and negative electrodes due to their proximity. The negative electrode has therefore been removed and replaced by a ground connection. The pictures of the manufactured device are displayed in Figure 3.11.

3.5.2 Experimental frequency filtering capabilities

After setting the AWR on a beam and bonding wires towards SMA connectors, the sensor has again been actuated by a pulsar and the output has been collected on an oscilloscope. The signal and its Fourier Transform are represented on Figure 3.12 and display three distinct peaks around 100, 115 and 130 MHz characteristic of the three waves emitted and received in the concerned directions.

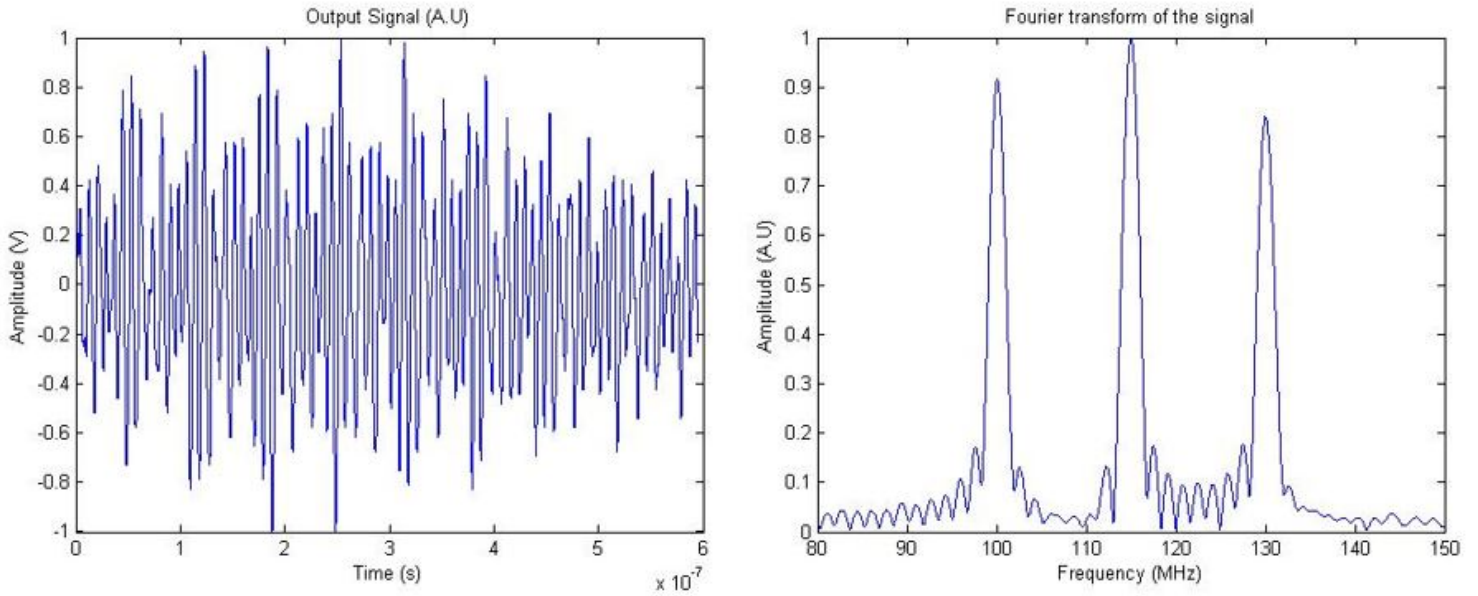


Figure 3.12: Experimental output signal (left) and associated spectrum (right) obtained from the manufactured 2D device

3.5.3 Experimental relations Frequency/Strain

The strain measurement experiments for the AWR have been conducted with an approach similar to subsection 3.4.3. The sensor has been bonded on a loaded beam and a reference value for the longitudinal strain has been obtained from resistive strain gages. The other stress and strain values were calculated from Equations 2.39 and 2.40.

For different loads, the output signals from the sensor have been collected and the positions of the three peaks identified on Figure 3.12 have been computed. Given the knowledge of the angles associated with each of these frequencies, the theoretical frequency shifts associated with each longitudinal strain could be calculated and compared with the experimental results (Figure 3.13).

For each peak, the experimental relation between frequency shifts and the longitudinal strain can be approximated through a linear regression. Their slopes and coefficients of determination R^2 are respectively $-38 \text{ Hz}/\mu\epsilon$ and 0.963 for the 100-MHz-resonance, $59 \text{ Hz}/\mu\epsilon$ and 0.971 for the 115-MHz-resonance, $143 \text{ Hz}/\mu\epsilon$ and 0.998 for the 130-MHz-

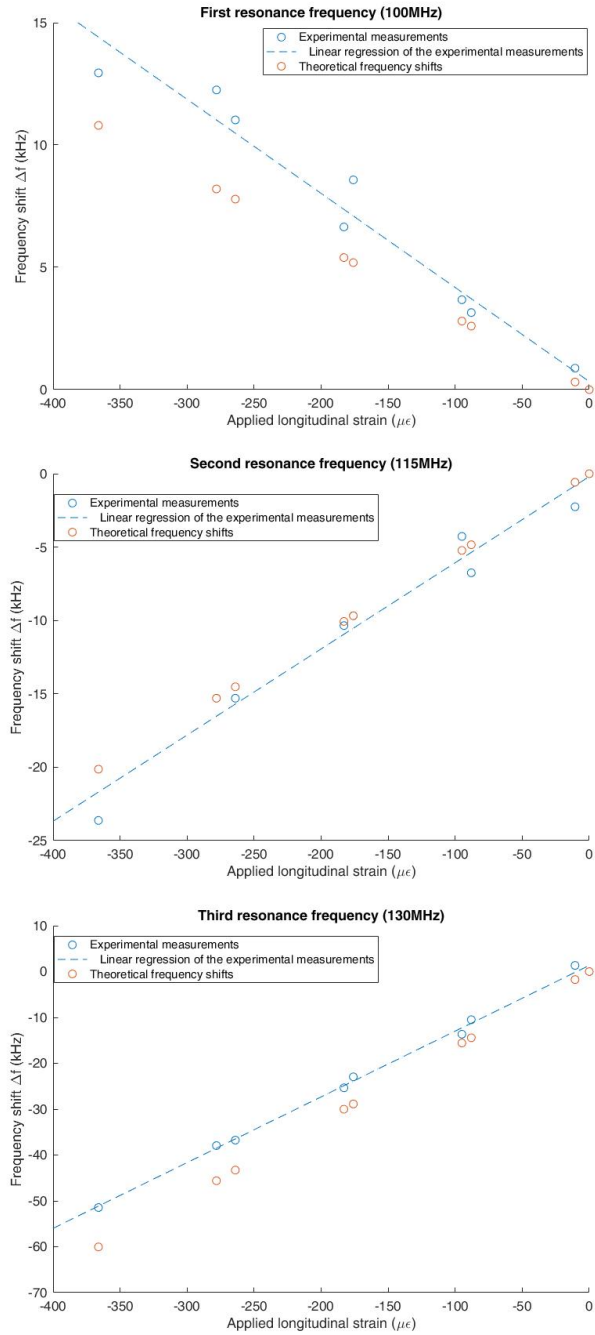


Figure 3.13: Experimental and theoretical frequency shifts for the AWR

resonance. The associated theoretical slopes are $-30 \text{ Hz}/\mu\epsilon$, $55 \text{ Hz}/\mu\epsilon$ and $164 \text{ Hz}/\mu\epsilon$

3.6 Conclusion

In Chapter 3, the focus has been shifted to the manufacturing and testing of the 1D and 2D SAW strain sensors. After establishing the layer disposition and the fabrication strategy, the devices have been produced in GeorgiaTech cleanroom by following microfabrication methods. The electrode patterns defined in Chapter 2 have been printed upon the devices by photolithography and used to actuate the piezoelectric layer.

The frequency filtering capabilities of the 1D device has first been tested upon a broadband actuation. After bonding the device to a beam, the frequency shift of the peak has been measured for various strains and the experimental results have been compared to the theoretical values.

This approach has been repeated for the AWR. After manufacturing the device, its capability to filter three peaks associated with different wave directions has been shown. The two-dimensional strain sensing capacities of the device has been tested on a beam and the experimental results have been compared to theoretical ones.

CHAPTER 4

CHARACTERIZATION OF THE ACOUSTIC DATA TRANSMISSION BY PIEZOELECTRIC TRANSDUCTION

4.1 Overview

Ultrasounds have been used as a means of communication as an alternative to electromagnetic waves for which communications can be limited by bandwidth regulations [73] or Faraday shielding. In 2003, Hu et al. [48] have first theoretically formulated the possibility of transmitting energy and data across metallic structure by piezoelectric transduction. The structure described was made of one metallic plate sandwiched between two piezoelectric transducers, acting as an actuator and a receiver. Further experiments [53, 54, 55, 57] have shown the necessity to incorporate bonding layers attaching the transducers to the plate in these representations.

The following work focus on deriving a simple one-dimensional analytical model that can be further used to describe the impact of different parameters on the transmission without the time-consuming disadvantages of Finite Element Models. The one-dimensional assumption of the model will be checked by comparing it to multi-dimensional Finite Element results and its overall validity will be verified by experimental results. More specifically, the impact of the bonding layers on the output voltage has been assessed.

4.2 Description of the electro-mechanical behavior in the frequency domain

The efficiency of data transmission across a barrier can be evaluated in the frequency domain through two parameters: the output voltage magnitude and the associated bandwidth. Consequently, only the frequency content of the signals has been studied.

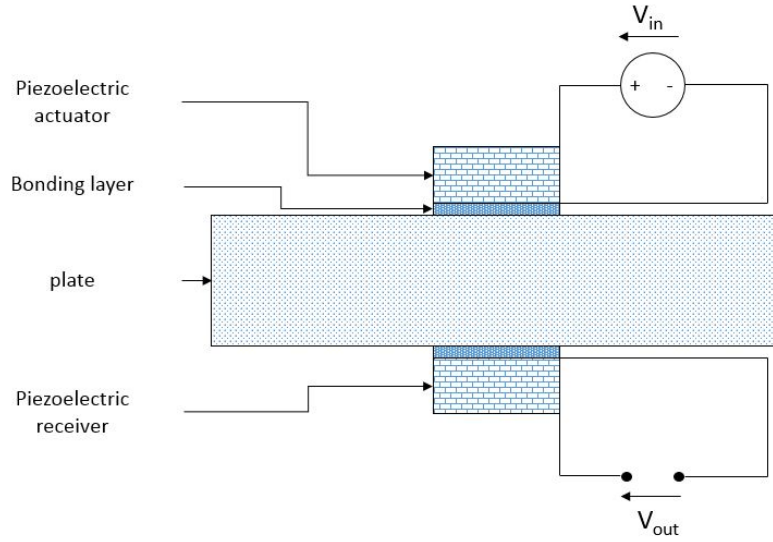


Figure 4.1: Representation of the structure for acoustic data transmission by piezoelectric transduction

4.2.1 Structure for data transmission

The simplest configuration ensuring data transmission across a metallic barrier is achieved by bonding two piezoelectric transducers facing each other across the plate, as first proposed in the patent [49]. The characteristics of the plate (material and thickness) are assumed to be known and set. Both transducers are made of Lead-Zirconate PZT-5A (except when specified otherwise) and their thickness is a parameter that can be chosen. The connection between the plate and both transducers is ensured by bonding layers such as conductive epoxy or solder patches.

The piezoelectric transducer used as an actuator is powered by a function generator. An oscilloscope is connected to the receiving transducer, which can be considered as in open-circuit. Assuming an harmonic excitation at a frequency f of amplitude V_{in} , the acoustic transmission is characterized by the transmitted power T_p :

$$T_p = 20 \log \frac{V_{out}}{V_{in}} \quad (4.1)$$



Figure 4.2: Representation of the forces and displacements applied on one element

where V_{out} is the amplitude of the voltage measured by the oscilloscope. The structure for acoustic transmission is shown on Figure (4.1). It can be noted that additional layers can be added below and above the transducers to alter the mechanical behavior and provide the desired output voltage. Besides, the layer structure is symmetric around the plate to optimize the acoustic transmission.

4.2.2 Derivation of an analytical rod model

A first analytical model has been developed in one-dimension by representing each layer as a rod. The plane strain approximation is used to describe the mechanical behavior of the elements. The studied system is divided between rods of different characteristics (dimensions, density, Young's modulus).

Inside passive elements, the stresses are expressed as:

$$T_{33} = c_{33}u_{,3} \quad (4.2)$$

where T_{ij} is the stress tensor, c_{ij} is the stiffness matrix and u is the longitudinal displacement in the \vec{e}_z direction. For a single element of thickness L , the forces applied on its

boundaries are $-F_1\vec{e}_z$ and $F_2\vec{e}_z$ (Figure 4.2) with:

$$\begin{aligned} F_1 &= c_{33}A \frac{du(z=0)}{dz} \\ F_2 &= c_{33}A \frac{du(z=L)}{dz} \end{aligned} \quad (4.3)$$

where A is the cross-section of the element. A harmonic solution is suggested for the displacements:

$$u(x) = a_1 \cos kz + a_2 \sin kz \quad (4.4)$$

where k is the wavenumber in the layer:

$$k = \omega \sqrt{\frac{\rho}{c_{33}}} \quad (4.5)$$

and ρ is the density. By substituting the expression 4.4 into 4.3, a matrix expression for the forces is expressed:

$$\begin{bmatrix} -F_1 \\ F_2 \end{bmatrix} = \begin{bmatrix} 0 & -kc_{33}A \\ -kc_{33}A \sin kL & kc_{33}A \cos kL \end{bmatrix} \begin{bmatrix} a_1 \\ a_2 \end{bmatrix} \quad (4.6)$$

Besides, the displacements at the nodes are obtained from 4.4 as:

$$\begin{bmatrix} u_1 \\ u_2 \end{bmatrix} = \begin{bmatrix} 1 & 0 \\ \cos kL & \sin kL \end{bmatrix} \begin{bmatrix} a_1 \\ a_2 \end{bmatrix} \quad (4.7)$$

By inverting the matrix equation 4.7 and injecting it into 4.6, a direct relation between the forces and the displacements at the nodes is obtained:

$$\begin{bmatrix} -F_1 \\ F_2 \end{bmatrix} = [K] \begin{bmatrix} u_1 \\ u_2 \end{bmatrix} \quad (4.8)$$

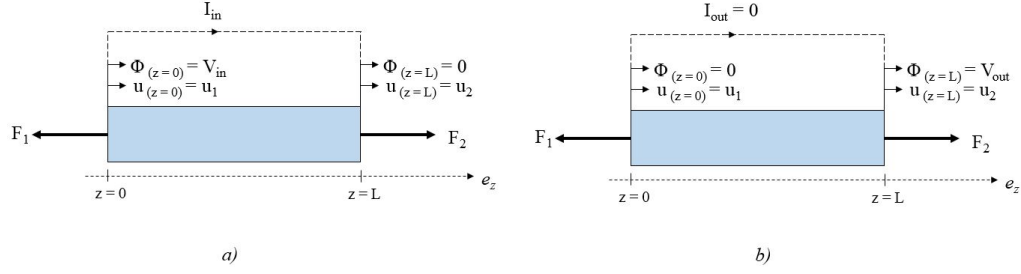


Figure 4.3: Representation the displacements, forces, electric potentials and currents for a) an actuator b) a receiver

where $[K]$ is the stiffness matrix of the element expressed by:

$$[K] = kc_{33}A \begin{bmatrix} \cot kL & -\csc kL \\ -\csc kL & \cot kL \end{bmatrix} \quad (4.9)$$

In the case of piezoelectric elements, the linear relations governing the mechanical and electrical behaviors are:

$$\begin{aligned} T_{33} &= c_{33}u_{,3} - e_{33}E_3 \\ E_3 &= -\phi_{,3} \\ e_{33}u_{,33} - \epsilon_{33}\phi_{,33} &= 0 \\ D_3 &= e_{33}u_{,3} + \epsilon_{33}E_3 \end{aligned} \quad (4.10)$$

where e_{ij} and ϵ_{ij} are the piezoelectric and dielectric tensors, E , D and ϕ are the electric field, displacement and potential.

In the case of an actuator (Figure 4.3.a), the expression of the electrical potential is obtained by integrating twice Equation 4.10.3 and applying the boundary conditions. As-

suming that the back electrode is perfectly grounded, the latter are defined as:

$$\begin{aligned}\phi(z = 0) &= V_{in} \\ \phi(z = L) &= 0\end{aligned}\tag{4.11}$$

Therefore, the electric potential in the actuator is given by:

$$\phi(z) = \frac{L - z}{L} V_{in} + \frac{e_{33}}{\epsilon_{33}} (u(z) - u(0)) - \frac{e_{33}}{\epsilon_{33}} z (u(L) - u(0))\tag{4.12}$$

The forces F_1 and F_2 can be derived from the equations 4.10.1 and 4.10.2 as:

$$\begin{aligned}F_1 &= c_{33} A \frac{du(z = 0)}{dz} + e_{33} \frac{d\phi(z = 0)}{dz} \\ F_2 &= c_{33} A \frac{du(z = L)}{dz} + e_{33} \frac{d\phi(z = L)}{dz}\end{aligned}\tag{4.13}$$

By injecting the expression of the electric potential 4.12, F_1 and F_2 are obtained as:

$$\begin{aligned}F_1 &= c_{33} A \frac{du(z = 0)}{dz} - e_{33} \frac{V_{in}}{L} + \frac{e_{33}^2}{\epsilon_{33}} \frac{du(z = 0)}{dz} - \frac{e_{33}^2}{\epsilon_{33}} (u(L) - u(0)) \\ F_2 &= c_{33} A \frac{du(z = L)}{dz} - e_{33} \frac{V_{in}}{L} + \frac{e_{33}^2}{\epsilon_{33}} \frac{du(z = L)}{dz} - \frac{e_{33}^2}{\epsilon_{33}} (u(L) - u(0))\end{aligned}\tag{4.14}$$

With the harmonic expressions for the displacements 4.4, the matrix equation relating the forces, input voltage and displacements is given by:

$$\begin{bmatrix} -F_1 - e_{33} \frac{V_{in}}{L} \\ F_2 + e_{33} \frac{V_{in}}{L} \end{bmatrix} = [K] \begin{bmatrix} u_1 \\ u_2 \end{bmatrix}\tag{4.15}$$

where

$$[K] = A \begin{bmatrix} \frac{e_{33}^2}{\epsilon_{33}L}(\cos kL - 1) & -k(c_{33} + \frac{e_{33}^2}{\epsilon_{33}}) + \frac{e_{33}^2}{\epsilon_{33}L} \sin kL \\ -k(c_{33} + \frac{e_{33}^2}{\epsilon_{33}}) \sin kL - \frac{e_{33}^2}{\epsilon_{33}L}(\cos kL - 1) & k(c_{33} + \frac{e_{33}^2}{\epsilon_{33}}) \cos kL - \frac{e_{33}^2}{\epsilon_{33}L} \sin kL \end{bmatrix}^* \begin{bmatrix} 1 & 0 \\ \cos kL & \sin kL \end{bmatrix}^{-1} \quad (4.16)$$

The receiving transducer (Figure 4.3.b) is in open circuit and its electric displacement D_3 consequently reaches zero. According to Equation 4.10.4, the electric field in the receiver is given by:

$$E_3 = -\frac{e_{33}}{\epsilon_{33}}u_{,3} \quad (4.17)$$

Therefore, from 4.10.1, the forces applied at the nodes of the receiver are:

$$\begin{aligned} F_1 &= (c_{33} + \frac{e_{33}^2}{\epsilon_{33}})A \frac{du(z=0)}{dz} \\ F_2 &= (c_{33} + \frac{e_{33}^2}{\epsilon_{33}})A \frac{du(z=L)}{dz} \end{aligned} \quad (4.18)$$

The relations between the forces and displacements in the receiver are:

$$\begin{bmatrix} -F_1 \\ F_2 \end{bmatrix} = [K] \begin{bmatrix} u_1 \\ u_2 \end{bmatrix} \quad (4.19)$$

with

$$[K] = k(c_{33} + \frac{e_{33}^2}{\epsilon_{33}})A \begin{bmatrix} \cot kL & -\csc kL \\ -\csc kL & \cot kL \end{bmatrix} \quad (4.20)$$

Let's now consider a structure of N elements, where the actuator is the N_{act} -th layer and the receiver is the N_{rec} -th layer (Figure 4.4). Each layer is characterized by its stiffness

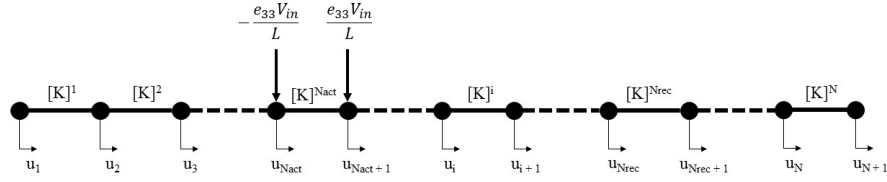


Figure 4.4: Representation of a structure of N layers and with their associated stiffness matrices

matrix expressed by the relations 4.9, 4.16 or 4.20, depending on the type of element used.

For the i-th layer, the stiffness matrix has a dimension of 2 X 2:

$$[K^i] = \begin{bmatrix} K_{11}^i & K_{12}^i \\ K_{21}^i & K_{22}^i \end{bmatrix} \quad (4.21)$$

A global stiffness matrix $[K^g]$ of dimensions $(N+1) \times (N+1)$ is built as an association of the stiffness matrices for the N layers:

$$[K^g] = \begin{bmatrix} K_{11}^1 & K_{12}^1 & 0 & \dots & 0 \\ K_{21}^1 & K_{22}^1 + K_{11}^2 & K_{12}^2 & \dots & 0 \\ 0 & K_{21}^2 & K_{22}^2 + K_{11}^3 & \dots & 0 \\ \vdots & \vdots & \vdots & \ddots & \vdots \\ 0 & 0 & 0 & K_{11}^{N-1} + K_{22}^{N-2} & K_{12}^{N-1} & 0 \\ 0 & 0 & 0 & K_{21}^{N-1} & K_{22}^{N-1} + K_{11}^N & K_{12}^N \\ 0 & 0 & 0 & 0 & K_{21}^N & K_{22}^N \end{bmatrix} \quad (4.22)$$

Assuming the vibrations in the structure are only driven by the voltage applied on the

actuator, the relation between the applied voltage and the displacements at the $N + 1$ nodes are given by:

$$\begin{array}{c}
 \text{row } N_{act} \\
 \text{row } N_{act} + 1
 \end{array}
 \begin{pmatrix}
 0 \\
 \vdots \\
 -e_{33} \frac{V_{in}}{L} \\
 e_{33} \frac{V_{in}}{L} \\
 \vdots \\
 \vdots \\
 \vdots \\
 0
 \end{pmatrix}
 = [K^g]
 \begin{pmatrix}
 u_1 \\
 \vdots \\
 \vdots \\
 \vdots \\
 u_{N_{rec}} \\
 u_{N_{rec}+1} \\
 \vdots \\
 u_N
 \end{pmatrix}
 \quad (4.23)$$

All the displacements are obtained by inverting Equation 4.23.

By assuming that the left node of the receiving transducer is grounded, the output voltage V_{out} on its right node is calculated by integrating Equation 4.10.4 between both sides of the element. Therefore, V_{out} is given by:

$$V_{out} = \frac{e_{33}}{\epsilon_{33}} (u_{N_{rec}+1} - u_{N_{rec}}) \quad (4.24)$$

4.2.3 Comparison with finite elements results

The validity of the analytical rod model developed in the previous subsection can be limited by two aspects:

- The mechanical behavior of each layer in the structure is expressed under the plane-strain approximation
- The model is one-dimensional and does not take into account the boundary effects arising from the finite dimensions of the piezoelectric transducers.

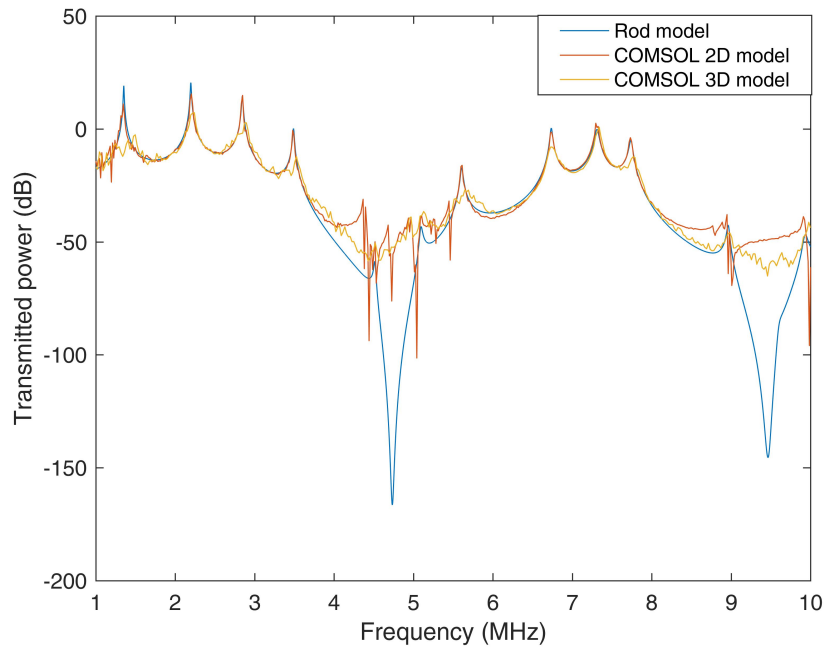


Figure 4.5: Comparison of the transmitted power given by the rod model, a COMSOL 2D model and a COMSOL 3D model for a 1-mm-thick transducer bonded to a 1-mm-thick copper plate

On the other hand, Finite Elements Methods (FEMs) can overcome these limitations by introducing the second and third dimensions. Their interest in design processes is limited by their higher computation times, but FEMs can be used to provide a validation step for the one-dimensional analytical model. The commercial software COMSOL has been used to generate 2D and 3D models. The structure used in the computations is made of 1-mm-thick transducers attached directly to a 1-mm-thick copper plate, without bonding layers. The transmitted power (Figure 4.5) described by the finite element models compares favorably with the results obtained from the analytical rod model at/between the resonances. On the opposite side, the rod model indicates strong transmission drops at the frequencies characteristic of the piezoelectric anti-resonances, which are not as apparent on the finite element results.

Figure 4.6 shows a representation the longitudinal displacements from the actuator towards the receiver at the resonance frequency 2.15MHz. At the center, the displacements are

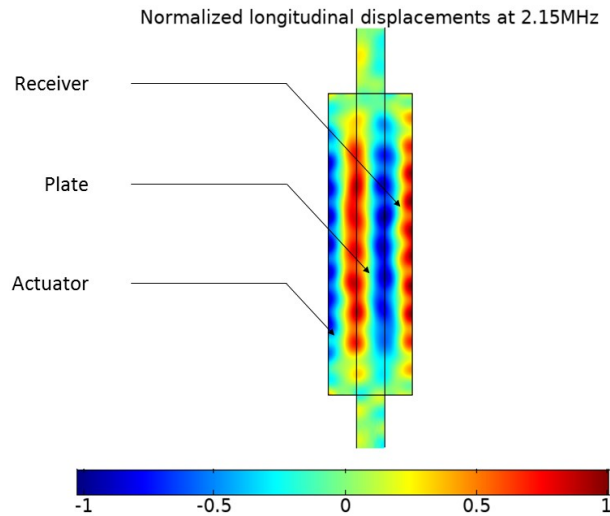


Figure 4.6: 2D finite element representation of the normalized longitudinal displacements at 2.15MHz

characterized by wavefronts parallel to the surface of the transducers and can be described by the one-dimensional rod model. However, on the sides of the piezoelectric patches, the displacements are mostly defined by the boundary effects. Around the resonances, the displacements on the borders are much weaker than the ones in the middle. The impact of the boundary effects are limited, therefore making the one-dimensional model a coherent - though overestimating - approach to describe the transmission.

At the anti-resonances, the wavelength λ introduced by the rod model is proportional to the thickness of the piezoelectric layers, thus providing identical longitudinal displacements between the two faces of the transducers. As the output voltage is proportional to the difference of displacements between both faces, the rod model describes a sharp transmission drop. Consequently, on the FE models, the transmitted power mostly comes from the boundary effects and cannot be described by the one-dimensional analytical model.

Given the objective of transmitting signals with a sufficient amplitude, the structure performance will be studied away from the anti-resonances and the rod model can be reliably used under this application.

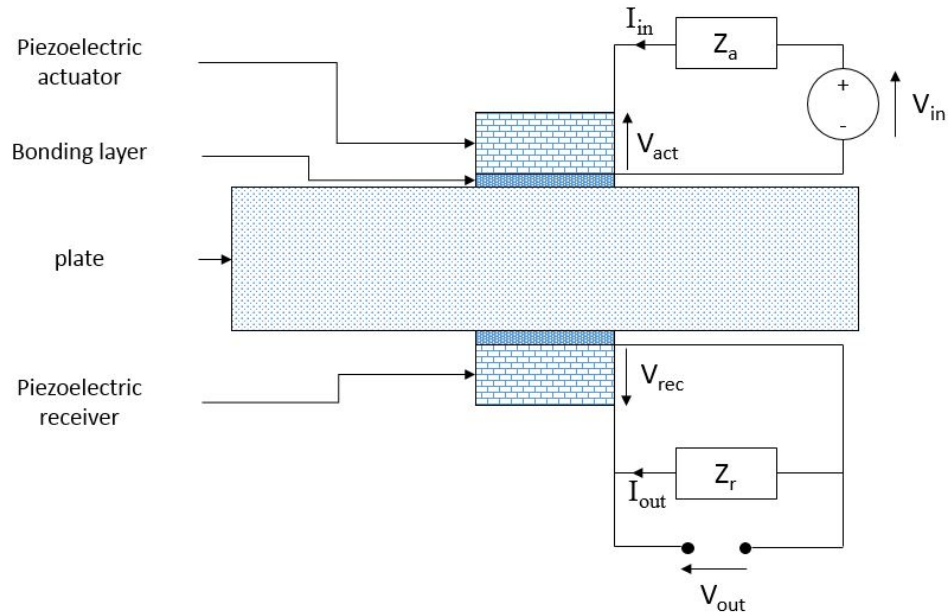


Figure 4.7: Representation of the structure for acoustic data transmission by piezoelectric transduction connected to electrical circuits

4.2.4 Mason model

The expressions of the transmission from the input to the output voltage can be modified to account for the presence of electrical circuits connected to the actuating and receiving transducers. Indeed, function generators are represented as a combination of a voltage source and an internal resistance, while oscilloscopes read the output voltages through an impedance. Besides, additional electric impedances Z_a and Z_r can be added respectively in series and parallel of the actuator and receiver to alter the output. Overall, the structure including the electrical circuits is shown in Figure 4.7.

The electric impedances have a direct influence on the electrical currents I_{in} and I_{out} traveling through them. They are related to the electric displacements in the piezoelectric transducers through:

$$I = A \frac{dD_3}{dt} = j\omega AD_3 \quad (4.25)$$

where I is the electric current traveling through the transducer.

By combining Equations 4.10.a and 4.10.d, the stresses within the piezoelectric layers are given as a function of the mechanical and electrical displacements:

$$T_{33} = (c_{33} + \frac{e_{33}^2}{\epsilon_{33}})u_{3,3} - \frac{e_{33}}{\epsilon_{33}}D_3 \quad (4.26)$$

Their expression is expanded by injecting 4.25 into 4.26:

$$T_{33} = (c_{33} + \frac{e_{33}^2}{\epsilon_{33}})u_{3,3} - \frac{e_{33}}{\epsilon_{33}} \frac{I}{j\omega A} \quad (4.27)$$

At the boundaries of the piezoelectric layers, the velocities v_1 and v_2 are expressed as:

$$\begin{aligned} v_1 &= \dot{u}_1 = j\omega u_1 \\ v_2 &= -\dot{u}_2 = -j\omega u_2 \end{aligned} \quad (4.28)$$

while assuming that the velocities are positive when the motion is directed inward the layer. As a result, the forces applied on the piezoelectric layer F_1 and F_2 are expressed as functions of the mechanical velocities at its boundaries and the electric current:

$$\begin{aligned} F_1 &= -jZ_p(\cot klv_1 + \csc klv_2) - j \frac{e_{33}}{\epsilon_{33}\omega} I \\ F_2 &= -jZ_p(\csc klv_1 + \cot klv_2) - j \frac{e_{33}}{\epsilon_{33}\omega} I \end{aligned} \quad (4.29)$$

where Z_p is the acoustic impedance of the piezoelectric layer:

$$Z_p = A \sqrt{\rho(c_{33} + \frac{e_{33}^2}{\epsilon_{33}})} \quad (4.30)$$

Equation 4.10.b relates the voltage in the piezoelectric transducers to the integrated form of the electric field. Given that the face directed towards the plate is considered as the ground,

the electric potential on the other face is expressed as:

$$V = - \int_{z=0}^{z=L} E_3 dz \quad (4.31)$$

where E_3 is expressed from Equation 4.10.d as:

$$E_3 = \frac{D_3}{\epsilon_{33}} - \frac{e_{33}}{\epsilon_{33}} u_{,3} \quad (4.32)$$

By injecting Equation 4.32 into 4.31 and expressing the electric and mechanical displacements as functions of the electric current and mechanical velocities according to Equations 4.25 and 4.28, the electric potential on the electrode V is given by:

$$V = -j \frac{e_{33}}{\epsilon_{33}\omega} (v_1 + v_2) - \frac{j}{\omega C_0} I \quad (4.33)$$

where C_0 is the electric capacitance of the piezoelectric layer:

$$C_0 = \frac{A\epsilon_{33}}{L} \quad (4.34)$$

Consequently, the transducers can be expressed as three-ports systems through the following matrix equation:

$$\begin{bmatrix} F_1 \\ F_2 \\ V \end{bmatrix} = -j \begin{bmatrix} Z \cot kl & Z \csc kl & \frac{e_{33}}{\epsilon_{33}\omega} \\ Z \csc kl & Z \cot kl & \frac{e_{33}}{\epsilon_{33}\omega} \\ \frac{e_{33}}{\epsilon_{33}\omega} & \frac{e_{33}}{\epsilon_{33}\omega} & \frac{1}{\omega C_0} \end{bmatrix} \begin{bmatrix} v_1 \\ v_2 \\ I \end{bmatrix} \quad (4.35)$$

The representation of the transducer can be restricted to a two-port device under two different configurations:

- If the transducer is backed by air (Figure 4.8.a), the force F_1 equals to 0. The voltage

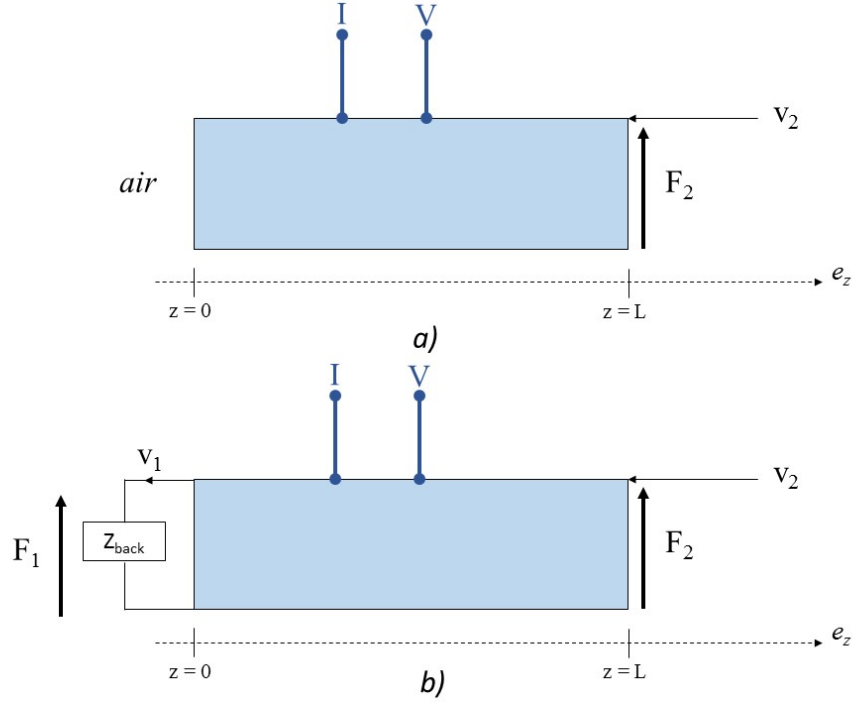


Figure 4.8: Representation of a two-port system for a) an air-backed transducer, b) a transducer backed by a layer of acoustic impedance Z_{back}

V and electric current I are found by reorganizing the matrix equation 4.35 into:

$$\begin{bmatrix} F_2 \\ v_2 \end{bmatrix} = [T_p] \begin{bmatrix} V \\ I \end{bmatrix} = \begin{bmatrix} T_{p11} & T_{p12} \\ T_{p21} & T_{p22} \end{bmatrix} \begin{bmatrix} V \\ I \end{bmatrix} \quad (4.36)$$

with

$$\begin{aligned} T_{p11} &= \frac{\epsilon_{33}}{e_{33}} \frac{\omega Z_p}{\tan kL/2} \\ T_{p12} &= j \frac{\epsilon_{33}}{e_{33}} \frac{\omega Z_p + 2C_0 \left(\frac{e_{33}}{\epsilon_{33}}\right)^2 (\cot kL - \csc kL)}{\omega C_0 \tan kL/2} \\ T_{p21} &= -j \frac{\epsilon_{33}}{e_{33}} \frac{\omega \cot kL}{\tan kL/2} \\ T_{p22} &= \frac{\epsilon_{33}}{e_{33}} \frac{\omega Z_p \cot kL - C_0 \left(\frac{e_{33}}{\epsilon_{33}}\right)^2}{\omega C_0 \tan kL/2} \end{aligned} \quad (4.37)$$

- If a backing layer is used over the transducer (Figure 4.8.b), it can be considered as an impedance Z_{back} connected to one port. The force and the velocity at this boundary

are related through:

$$F_1 = Z_{back}v_1 \quad (4.38)$$

where

$$Z_{back} = A\sqrt{\rho_{back}c_{33back}} \quad (4.39)$$

In this configuration, the coefficients of the transmission matrix $[T_p]$ are:

$$\begin{aligned} T_{p11} &= \frac{\omega Z_p(Z_p + jZ_{back} \cot kL)}{\frac{\epsilon_{33}}{\epsilon_{33}}(jZ_{back} + Z_p \tan kL/2)} \\ T_{p12} &= \frac{j\omega Z_p^2 + C_0\left(\frac{\epsilon_{33}}{\epsilon_{33}}\right)^2 Z_{back} + 2jC_0\left(\frac{\epsilon_{33}}{\epsilon_{33}}\right)^2 Z_p(\cot kL - \csc kL) - \omega Z_p Z_{back} \cot kL}{\omega C_0 \frac{\epsilon_{33}}{\epsilon_{33}}(jZ_{back} + Z_p \tan kL/2)} \\ T_{p21} &= \frac{\omega(jZ_{back} - Z_p \cot kL)}{\frac{\epsilon_{33}}{\epsilon_{33}}(Z_{back} - jZ_p \tan kL/2)} \\ T_{p22} &= \frac{jC_0\left(\frac{\epsilon_{33}}{\epsilon_{33}}\right)^2 - \omega(Z_{back} - jZ_p \cot kL)}{\omega C_0 \frac{\epsilon_{33}}{\epsilon_{33}}(Z_{back} - jZ_p \tan kL/2)} \end{aligned} \quad (4.40)$$

On passive layers, the relation between the applied forces and mechanical velocities is obtained by injecting Equation 4.28 through 4.8:

$$\begin{bmatrix} F_1 \\ F_2 \end{bmatrix} = -j \begin{bmatrix} Z \cot kl & Z \csc kl \\ Z \csc kl & Z \cot kl \end{bmatrix} \begin{bmatrix} v_1 \\ v_2 \end{bmatrix} \quad (4.41)$$

which can be reorganized as a two-port system through:

$$\begin{bmatrix} F_2 \\ v_2 \end{bmatrix} = [T] \begin{bmatrix} F_1 \\ v_1 \end{bmatrix} = \begin{bmatrix} \cos kl & -jZ \sin kl \\ -j \sin kl/Z & \cos kl \end{bmatrix} \begin{bmatrix} F_1 \\ v_1 \end{bmatrix} \quad (4.42)$$

where Z is the acoustic impedance of the passive layer:

$$Z = A\sqrt{\rho c_{33}} \quad (4.43)$$

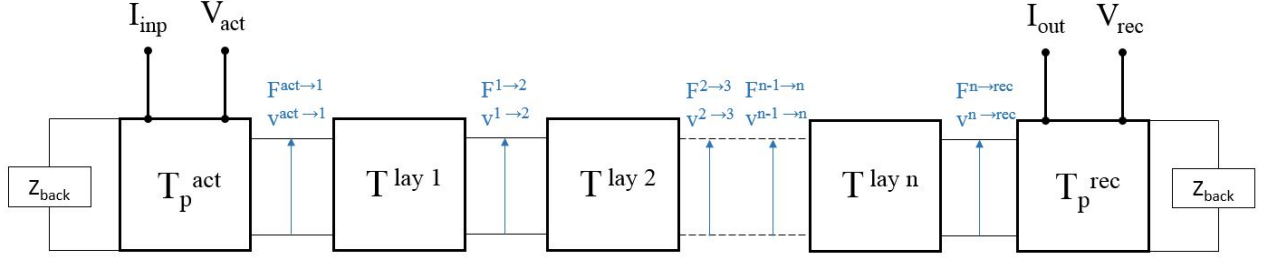


Figure 4.9: Equivalent model for n layers sandwiched between two piezoelectric transducers

The structure described in Figure 4.9 incorporates an actuator, a receiver and n passive layers. The voltages V_{act} and V_{rec} represent the differences of electric potentials taken directly from the transducers, as opposed to V_{in} and V_{out} that are the values emitted by the generator and collected by the oscilloscope. At the boundaries between two layers, the forces and velocities are equal on both sides. Consequently, the transmission matrices associated with the passive and piezoelectric layers can be combined to relate the output voltage and current to the input voltage and current through:

$$\begin{aligned}
 \begin{bmatrix} V_{rec} \\ I_{out} \end{bmatrix} &= [T_p^{rec}]^{-1} \begin{bmatrix} F_2^{lay n} \\ v_2^{lay n} \end{bmatrix} \\
 \begin{bmatrix} F_2^{lay n} \\ v_2^{lay n} \end{bmatrix} &= [T^{lay n}] \begin{bmatrix} F_2^{lay n-1} \\ v_2^{lay n-1} \end{bmatrix} = [T^{lay n}][T^{lay n-1}] \dots [T^{lay 1}] \begin{bmatrix} F_1^{lay 1} \\ v_1^{lay 1} \end{bmatrix} \\
 \begin{bmatrix} F_1^{lay 1} \\ v_1^{lay 1} \end{bmatrix} &= [T_p^{act}] \begin{bmatrix} V_{act} \\ I_{in} \end{bmatrix}
 \end{aligned} \tag{4.44}$$

By associating the three previous matrix equations, the output electric potential and current

are given as:

$$\begin{bmatrix} V_{rec} \\ I_{out} \end{bmatrix} = [T_{tot}] \begin{bmatrix} V_{act} \\ I_{in} \end{bmatrix} = \begin{bmatrix} T_{tot11} & T_{tot12} \\ T_{tot21} & T_{tot22} \end{bmatrix} \begin{bmatrix} V_{act} \\ I_{in} \end{bmatrix} \quad (4.45)$$

where:

$$[T_{tot}] = [T_p^{rec}]^{-1} [T^{lay n}] [T^{lay n-1}] \dots [T^{lay 1}] [T_p^{act}] \quad (4.46)$$

The output potential V_{out} can be obtained as function of the input voltage V_{in} in two situations:

- In absence of input and output electric impedances ($Z_a = 0$ and $Z_r = \infty$), the output circuit is open ($I_{out} = 0$) and the difference in potential at the terminals of the actuator V_{act} equals to the input voltage brought by the generator V_{in} . The solution of Equation 4.45 is:

$$V_{out} = \frac{T_{tot11}T_{tot22} - T_{tot12}T_{tot21}}{T_{tot22}} V_{in} \quad (4.47)$$

- In presence of input and output electric impedances, the currents in the input and output circuits are:

$$\begin{aligned} I_{out} &= -V_{out}/Z_r \\ I_{in} &= \frac{V_{in} - V_{act}}{Z_a} \end{aligned} \quad (4.48)$$

Given that $V_{rec} = V_{out}$, the solution of Equation 4.45 is:

$$V_{out} = \frac{(T_{tot11}T_{tot22} - T_{tot12}T_{tot21})Z_r}{T_{tot12} + T_{tot22}Z_r - T_{tot11}Z_a - T_{tot21}Z_rZ_a} V_{in} \quad (4.49)$$

4.3 Experimental validation of the analytical rod model

4.3.1 Setup and configuration

The validity of the Mason model has been tested through experiments. The structure made for acoustic transmission was constituted of a metal plate sandwiched between two piezoelectric transducers attached by a bonding layer. The actuator was excited harmonically by a function generator while sweeping over a given span of frequencies. The output voltage was measured directly between the two faces of the receiving transducer and collected on an oscilloscope for each frequency. The transmission is characterized by the amplitude ratio between the received and emitted signal (in decibels).

The electrodes on each transducer are directly connected to SMA connectors, which are designed to handle high-frequency applications (up to the Gigahertz range) by limiting the electromagnetic interferences and noise. The function generator and oscilloscope are connected to these connectors by BNC/SMA cables.

The function generator is comprised of a voltage source in series with an internal resistance $Z_{gen} = 50\Omega$. Each BNC/SMA cable can be associated with a resistance $Z_{cable} = 50\Omega$. The oscilloscope has been set on its high input impedance mode and acts as a $10\text{ M}\Omega$ resistance ($Z_{oscillo}$). Figure 4.10 represents the structure and electric circuits used in the 1D Mason model to simulate the transmission across the plate. Given the extensive resistance associated with the oscilloscope, the receiving transducer can be considered as in open-circuit.

4.3.2 Results for configurations with conductive epoxy bonding layers

Different types of bonding layers can be used to attach the transducers to the plate. In the first reports of experimental data transmission from the literature, the connection was achieved by conductive epoxy [53, 54, 55]. These experiments have been reproduced by curing silver epoxy to 150°C to bond two piezoelectric patches of grade TRS 101 (TRS

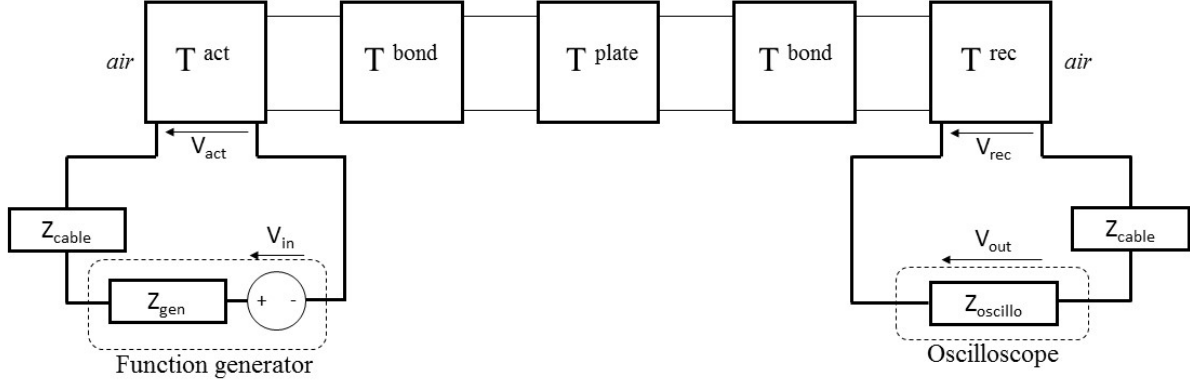


Figure 4.10: Equivalent model for the experimental setup

Technologies) to a 1-mm-thick copper plate. The dimensions of the transducers were 1cm X 1cm and the transmission has been studied for two channels of different piezoelectric thicknesses: 1.7 and 2.7 mm.

The experimental results have been compared to the theoretical ones in Figure 4.11. The output is characterized by peaks centered on the fundamental and harmonic resonances f_{R_n} of the isolated transducers:

$$f_{R_n} = \frac{(n - \frac{1}{2})}{l_{piezo}} \sqrt{\frac{c_{33 piezo} + \frac{e_{33 piezo}^2}{\epsilon_{33 piezo}}}{\rho_{piezo}}} \quad n = 1, 2, 3, \dots \quad (4.50)$$

Out of the resonances, the theoretical signal amplitude strongly drops as the frequencies reach the anti-resonances. The experimental and theoretical results show a good agreement at the resonances, while the noise level of the acquisition system is a limitation away from these peaks.

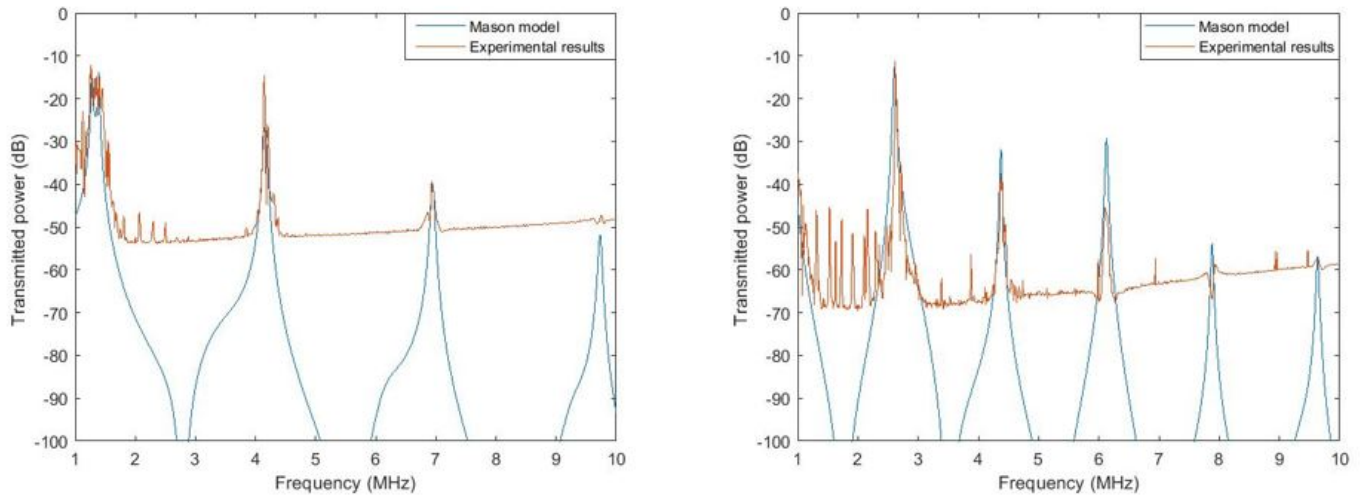


Figure 4.11: Comparison of the transmitted power obtained from experimental results and the Mason model for 1.7 and 2.7-mm-thick transducers bonded to a 1-mm-thick copper plate by conductive silver epoxy

The narrowness of the peaks restricts the bandwidths over which a proper acoustic transmission could be reached to the range of tens of kilo-Hertz (kHz).

4.3.3 Results for configurations with vacuum grease bonding layers

In further reports of experimental acoustic data transmission, higher rates were achieved with structures using vacuum grease as a bonding layer [56, 57]. The grease acts as a coupling material between the transducers and the plate, but does not provide a permanent attachment. Additional clamps are therefore required to hold the piezoelectric patches.

Experiments have been carried out in this configuration with 0.7-mm-thick PZT4 transducers attached to a 2-mm-thick aluminum plate through 30- μm -thick grease layers. The theoretical and experimental results are given in Figure 4.12 and show that the region with high transmission capabilities is spread over two peaks and reaches the range of hundreds of kilo-Hertz.

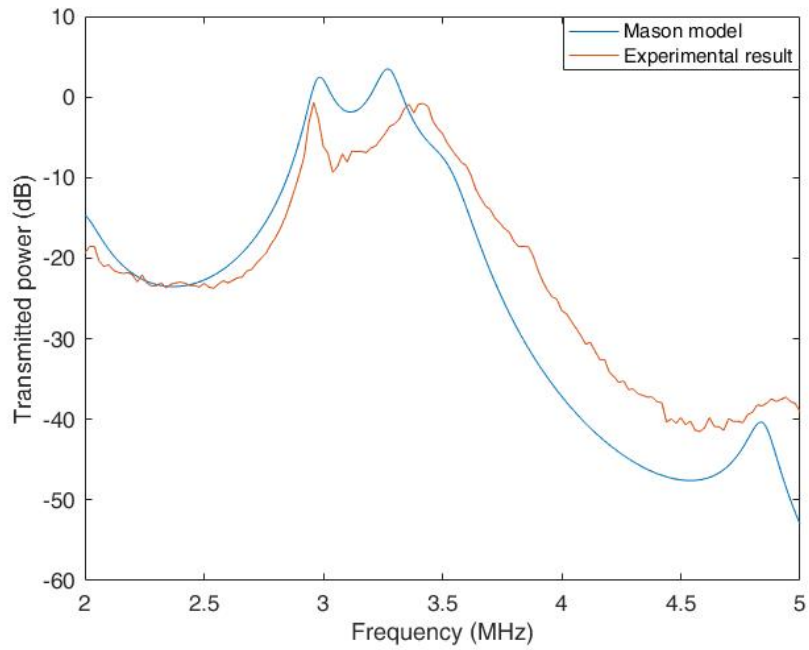


Figure 4.12: Comparison of the transmitted power obtained from experimental results and the Mason model for 0.7-mm-thick transducers bonded to a 2-mm-thick aluminum plate by vacuum grease

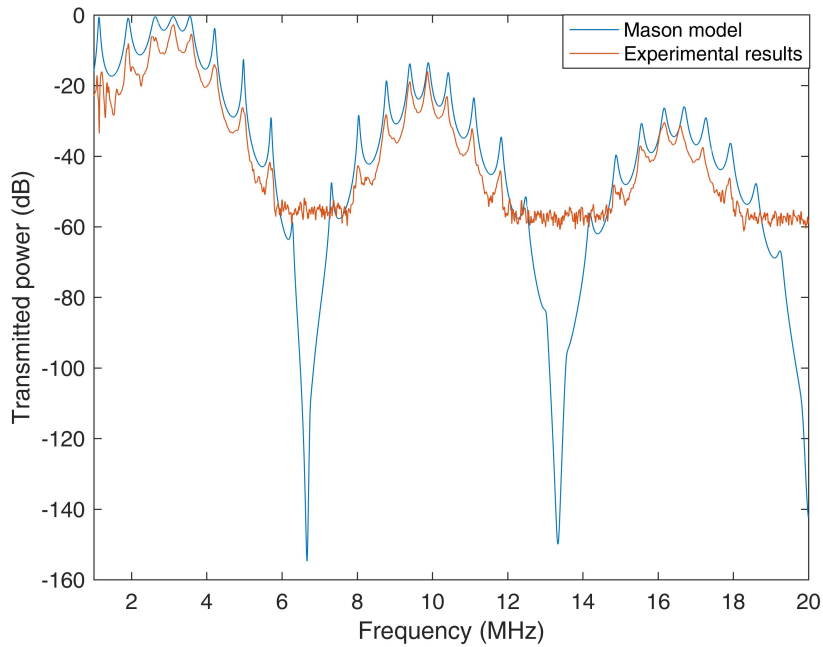


Figure 4.13: Comparison of the transmitted power obtained from experimental results and the Mason model for 0.7-mm-thick transducers bonded to a 3-mm-thick aluminum plate by solder patches

4.3.4 Results for configurations with solder patches bonding layers

Solder patches have been tested as a third bonding option in order to meet the requirement of a permanent attachment. The choice of solder materials are limited by their melting point. Indeed, the transducers are bonded in a two-stage process:

- A thin solder patch is placed on the upper surface of the plate, over which the first transducer is added. This structure is then taken in oven at a temperature slightly higher than the melting point of the solder.
- After a cooling stage, the plate is flipped and another stack of solder and transducer is placed on the upper face of the plate. The structure is again heated in an oven at a temperature slightly higher than the melting point of the second solder.

Therefore, the melting point of both solders should remain under the Curie temperature of the piezoelectric materials to prevent them from losing their polarization and consequently their piezoelectric properties. Besides, during the second stage, the transducer initially attached is facing downwards and would split off from the plate if the heating temperature met the melting point of its associated solder. The melting point of the second solder then needs to be lower than the one of the first solder. The first solder used is a Pb/Sn alloy with a melting point reaching $182^{\circ}C$, while the second one is made of Indium with a melting point of $156^{\circ}C$. Both solder patches have a thickness estimated at $25 \mu m$.

The theoretical and experimental results are given in Figure 4.13 and show multiple peaks between each anti-resonance. At the locations of the anti-resonances, the experimental output signal reached its noise level of the oscilloscope.

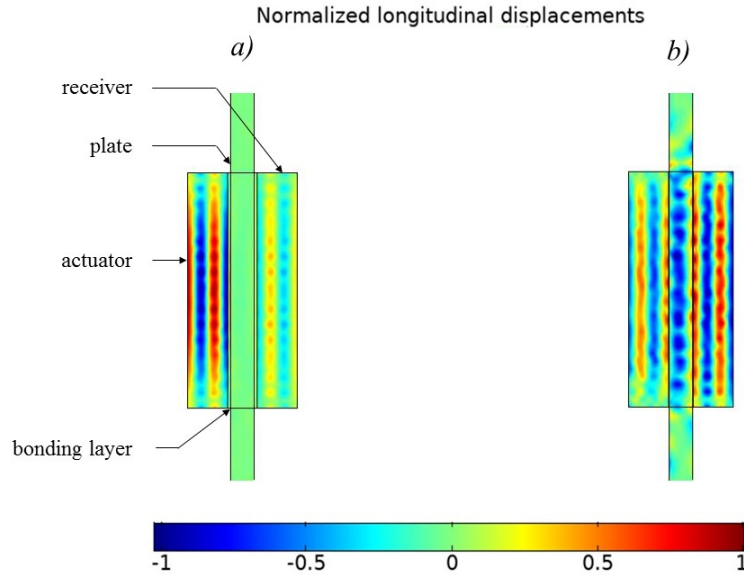


Figure 4.14: COMSOL 2D finite element representation of the normalized longitudinal displacements at resonance frequencies (4MHz) for configurations with a) silver epoxy bonding layers b) solder bonding layers

4.4 Influence of the bonding layer on the resonances

4.4.1 Cases of the epoxy and solder bonding layers

The experimental results displayed in the previous section demonstrated that the type of bonding layer strongly impacts the output at other frequencies.

Figure 4.14.a shows the longitudinal displacements generated by the actuator through a 2D COMSOL Finite Element model at a resonance frequency (4MHz) for a structure with a conductive epoxy bonding layer. It can be noted that the acoustic transmission from the actuator towards the plate is weak and that each transducer behaves as an element uncoupled from the plate. Indeed, the epoxy layer is characterized by a low acoustic impedance and a high thickness, which mostly entails wave reflections at their boundaries. In consequence of the lack of coupling, the transducers mechanically act as if they were isolated from the rest of the structure. The amplitude of the emitted vibrations therefore reach a maximum at the natural frequencies of the piezoelectric layers and the transmission only peaks at these

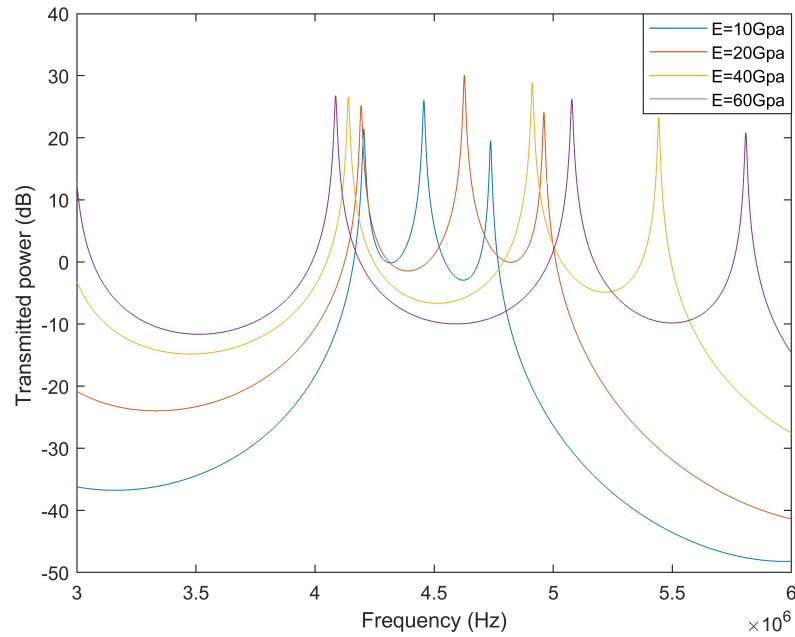


Figure 4.15: Comparison of the theoretical transmitted powers for 0.5-mm-thick transducers on a 1-mm-thick copper plate with 100- μm -thick bonding layers (density of 4000 k/m^3 , Young modulus ranging between 10 and 60 GPa)

specific frequencies.

On the other hand, Figure 4.14.b shows the longitudinal displacements for a structure with solder bonding layers. In this situation, the waves are mostly transmitted from the actuator towards the plate. Indeed, the solder patches are characterized by a higher acoustic impedance and a small thickness, and have a limited impact on the transmission between the different layers. Consequently, there is a strong coupling between the different layers of the structure, which generate the presence of multiple peaks between each anti-resonance.

4.4.2 Cases of intermediate bonding layers

The cases of the epoxy and solder bonding layers bring to light two extreme situations where the peaks are respectively grouped at the natural resonance of the transducers or spread at multiple locations between each anti-resonance. The bonding layers can therefore be seen as a means to bring resonance peaks closer to each other as their thickness increases

or/and their acoustic impedance decreases.

This point has been highlighted through Figure 4.15, which provides a comparison of the output powers for structures with various of bonding layers. The transducers used were 0.5-mm-thick and the plate was made of copper (1-mm-thick). The bonding layers used have similar thicknesses ($100 \mu m$) and densities ($4000 kg/m^3$) but different Young moduli (between 10 and 60 GPa). While peaks are spread over large frequency spans for bonding layers of high elasticity, decreasing their Young modulus has two major repercussions:

- Three peaks are brought together around the resonance frequency of the piezoelectric transducer
- The amplitude between the peaks increases

These two phenomena are closely related as bringing resonances closer to each other limits the amplitude drop between the peaks.

The addition of a layer with an acoustic impedance lower than the impedances of the transducers and the plate therefore offers an option to reduce the amplitude fluctuations between these three peaks that will be exploited in the next chapter.

4.5 Conclusion

The electro-mechanical behavior of an acoustic system intended to transmit data across metallic structures has been described through two one-dimensional analytical models:

- A rod model describing each layer through a stiffness matrix
- The Mason model, which describes the layers as two or three-ports systems

The one-dimensional aspect of these models has been validated through the comparison with two and three-dimensional Finite Element Models.

Experiments have been carried out as a second validation step. Different types of bonding layers have been used in these experiments: conductive epoxy and vacuum grease, which

have been employed in previous reports, as well as solder pastes, which provide the advantages of a permanent attachment with little influence on the transmission across the layers. On the other hand, bonding layers can modify the shape of the transmitted power by bringing peaks closer to each other as their thickness increases or/and their acoustic impedance decreases.

CHAPTER 5

WIDEBAND ACOUSTIC DATA TRANSMISSION BY PIEZOELECTRIC TRANSDUCTION

5.1 Overview

After previously describing the behavior of an acoustic system aiming at transmitting data across metallic barriers, this chapter will focus on different strategies limiting the amplitude variations over wide bandwidths.

Different approaches related both to the mechanical and electrical fields will be used in order to define the largest bandwidth possible within which amplitude fluctuations could be limited to 2 dB. In a second time, these approaches will be merged in order to draw benefits from each of them and optimize the frequency span over which data transmission of the desired quality could be achieved.

5.2 Limitations of the quality of data transmissions for undamped structures

The acoustic system for data transmission has been studied in the frequency domain in the previous chapter and different parameters characterizing the data transmission (in the time domain) can be brought forward:

- The transmission rate for the data (in bits per second or *bps*), which is directly related to the bandwidth of the channel.
- The ratio signal/noise, which is also depicted by the amplitude of the output voltage within the bandwidth in the frequency domain.

Beyond the ratio signal/noise, the quality of the transmission is also related to the correspondence between the input and output. Indeed, a signal distortion can originate from two

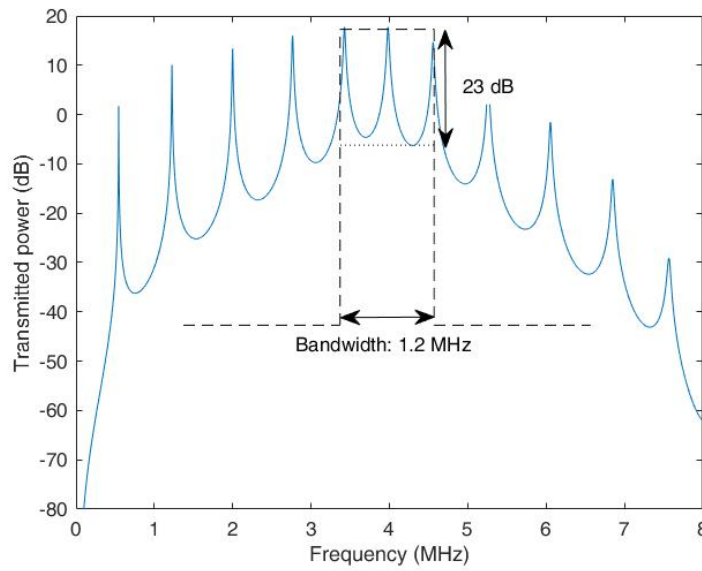


Figure 5.1: Transmitted power for 0.5-mm-thick PZT5A transducers bonded to a 3-mm-thick aluminum plate by solder patches

phenomena:

- The waves are reflected on the surface of each layers, thus creating footprints of the echoes in the received signal.
- According to the study from the previous chapter, the amplitude transmitted strongly depends on the frequency involved. Consequently, each frequency content of the emitted signal is transmitted at a different magnitude.

The first problem has been tackled in the literature through signal processing. In [62], a pre-distorsion filter was applied to reduce the echo amplitude by destructive interferences. Orthogonal frequency-division multiplexing (OFDM) is another method coming from RF systems that divides the wideband transmission channel into several orthogonal narrow-band channels in order to mitigate the effect of echoing for each of them [74, 63].

Solving the second issue is the topic of this chapter, which will be focused on limiting the amplitude variations within a targeted frequency span. The objective will be to damp the transmission at the resonances to bring the fluctuations of the transmitted power down to

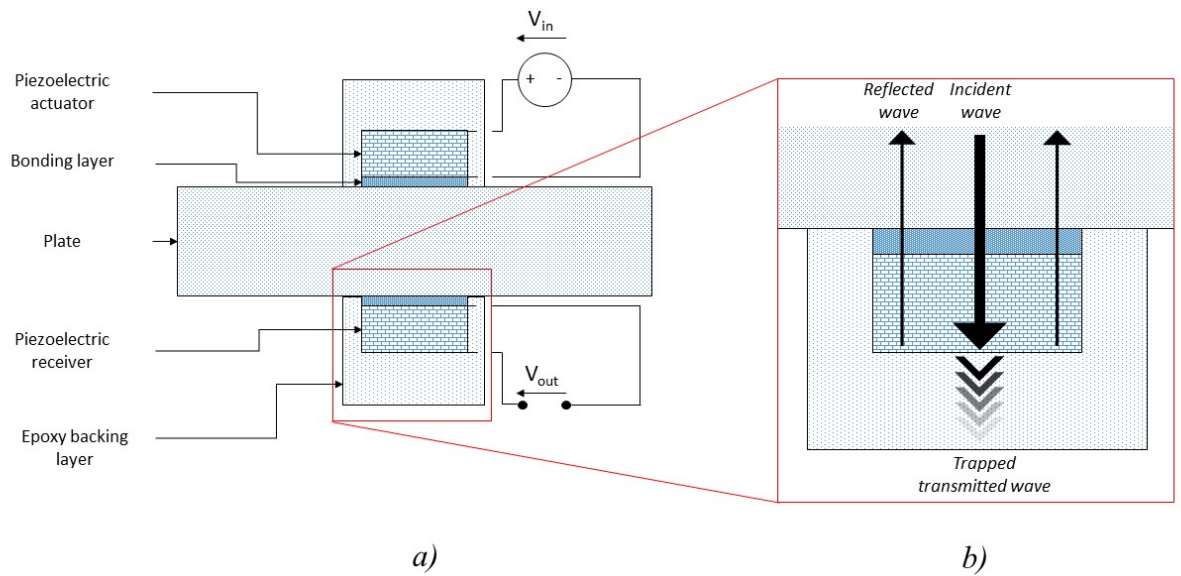


Figure 5.2: Representation of (a) the structure for acoustic data transmission by piezoelectric transduction and (b) the wave-trapping effect of the backing

2dB in the dedicated bandwidth. Figure 5.1 represents the transmitted power for 0.5-mm-thick transducers (PZT-5A) bonded to a 3-mm-thick aluminum plate by solders, without electric impedances in the circuits connected to the actuator and receiver. A 1.2 MHz bandwidth is organized around three peaks, within which the amplitude variations reach 23 dB and largely exceed the targeted value of 2 dB. This configuration is the basis which will be implemented to obtain acceptable fluctuations.

5.3 Reduction of the amplitude variations through backing layers

5.3.1 Introduction of backing layers

The total output voltage stems from the sum of:

- the waves transmitted directly from the actuator to the receiver
- the waves reflected at the boundary of the different layers, especially at the free surface of the piezoelectric transducers

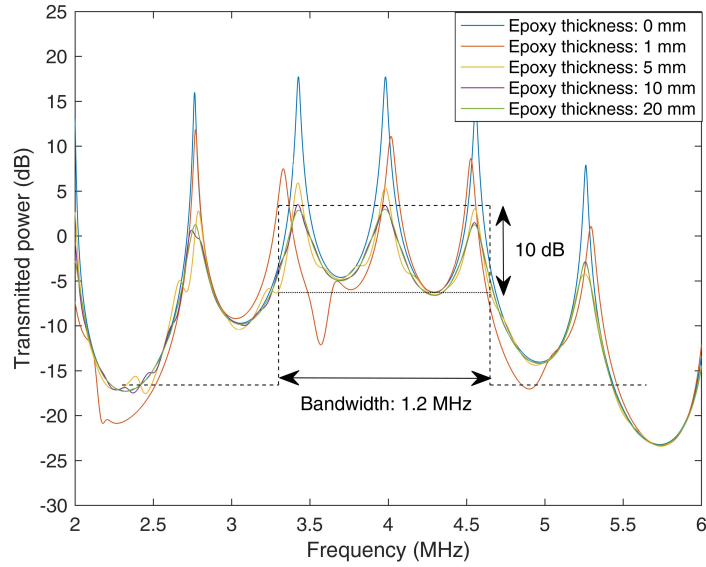


Figure 5.3: Transmitted power for 0.5-mm-thick PZT5A transducers bonded to a 3-mm-thick aluminum plate by solder patches, with epoxy backings of different thicknesses (0, 1, 5, 10 and 20 mm)

At the resonances, the constructive interference of both terms amplify the transmission and generate the undesirable peaks. A method to attenuate the wave reflections at the surface of the transducers consists in using a backing layer with damping properties that can trap this acoustic energy (Figure 5.2). Epoxy is commonly chosen as the backing material for its viscous properties, which provide (i) great acoustic attenuation capacities (ii) the possibility to encapsulate the transducers within an epoxy structure with a thickness of several millimeters.

The quality of the backing layer is characterized by two parameters:

- Its acoustic attenuation capacities (in dB), which depends on both the layer thickness L (in meters) and the damping attenuation coefficient α_{dB} (in dB/m) of the material:

$$attenuation_{dB} = L * \alpha_{dB} \quad (5.1)$$

It can be noted that the value of α_{dB} is only defined at a given frequency f and can

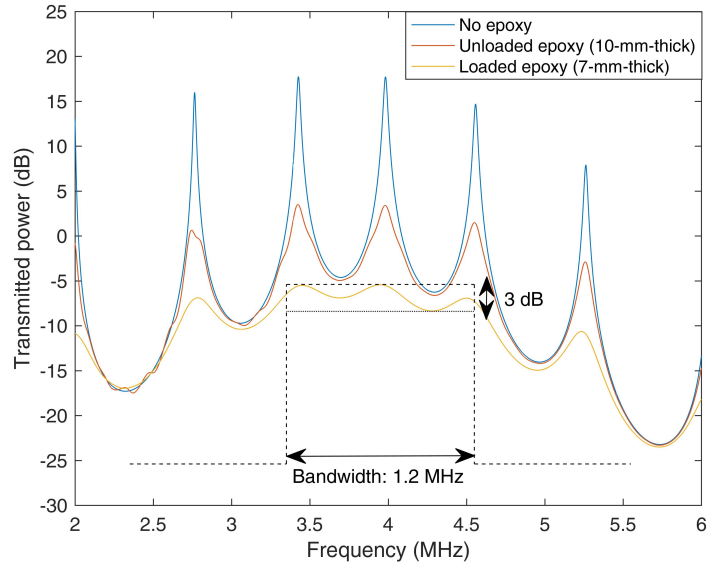


Figure 5.4: Comparison of the transmitted power for 0.5-mm-thick PZT5A transducers bonded to a 3-mm-thick aluminum plate by solder patches, with no backings, with a 10-mm-thick unloaded epoxy backing, and with a 7-mm-thick loaded epoxy backing

be related to the isotropic damping coefficient η through:

$$\alpha_{dB} = 8.69 \frac{\pi L \eta f}{c} \quad (5.2)$$

where c is the longitudinal wave velocity in the layer and the value "8.69" comes from the conversion between the Neper and Decibel units.

- Its acoustic impedance, as the transmission from the transducers to the backings depends on the impedance matching between the layers. The remaining energy is reflected and added constructively at the resonances to generate the undesired peaks.

In the further theoretical simulations, the backing material will be constituted of the epoxy glue Epotek-301. Figure 5.3 compares the transmitted power obtained for structures with backings of different thicknesses (0, 1, 5, 10 and 20 mm). The amplitude of the peaks drops as the backing thickness increases up to 10 mm, while the results obtained with 10-mm and 20-mm-thick layers are similar. Consequently, a backing thickness of 10 mm is sufficient to dissipate the acoustic energy of the waves transmitted to the epoxy. However,

under this configuration, the fluctuations within the bandwidth are only reduced down to 10 dB. Indeed, epoxy is characterized by a low acoustic impedance ($Z_{epox} = 3MRayl$) that generates a large mismatch with the transducers.

Its impedance can be raised by adding heavy tungsten particles in the epoxy. An homogeneous Epoxy-Tungsten composite can be obtained by centrifugation [75]. The mechanical properties of the loaded epoxy were provided by [76] for different Tungsten concentrations. The mixture with the highest indicated acoustic impedance (25% of Tungsten volume concentration) has been chosen. The Tungsten powder increases both the elastic constants and densities, therefore enhancing the backing impedance up to 10 MRayl. In addition, the attenuation capacities of the material are improved, hence decreasing the required layer thickness down to 7 mm.

Figure 5.4 shows the transmission for the structure with 25%-loaded epoxy. With its increased acoustic impedance, the theoretical amplitude variations within the 1.2-MHz-bandwidth were limited to 3 dB, therefore showing great improvement while compared with the structure with unloaded epoxy.

5.3.2 Combination of backing layers and additional electroplated layers

In the previous chapter, the possibility to bring peaks closer to each other by using a bonding layer of low impedance has been brought to light. A consequence of this convergence is the reduction of the amplitude drops happening between each resonance, therefore limiting the amplitude fluctuations.

In order to bring resonances together, layers with an acoustic impedance weaker than the transducers (in PZT5A) and the plate (in aluminum) need to be included between them. For thicknesses in the range of tens or hundreds microns, a practical approach to place these layers would be to deposit them onto one face of the transducers by electroplating. Among different elements that can be commonly electroplated, tin has the lowest acoustic impedance. The stack made of each piezoelectric transducer associated with the electro-

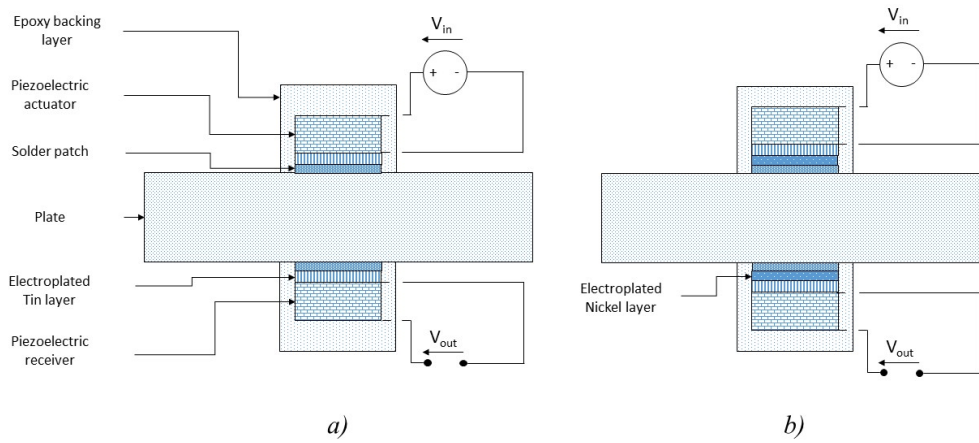


Figure 5.5: Representation of the structure for acoustic data transmission by piezoelectric transduction with (a) a tin electroplated layer, (b) a tin and a nickel electroplated layer

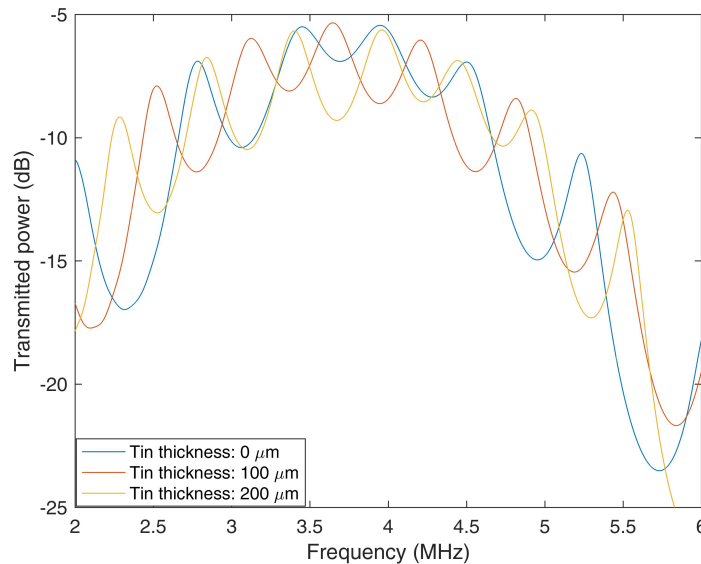


Figure 5.6: Comparison of the transmitted power for 0.5-mm-thick PZT5A transducers bonded to a 3-mm-thick aluminum plate by solder patches with loaded epoxy backing, without tin layer or with 100/200 μm tin layers

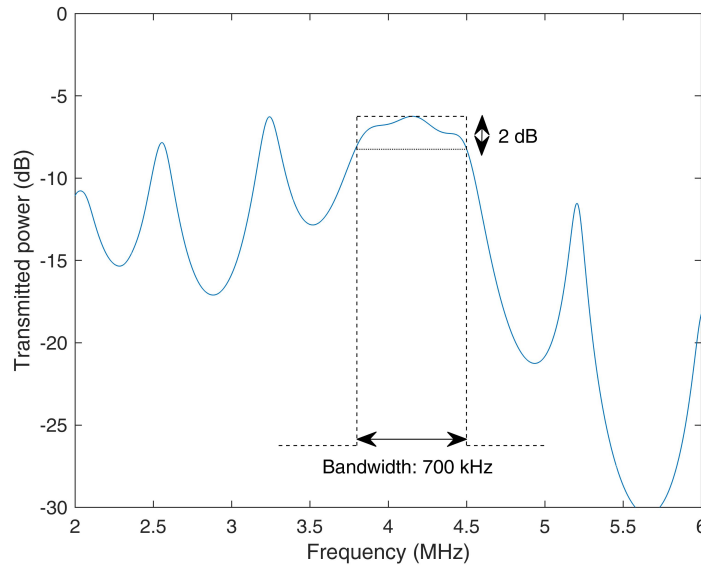


Figure 5.7: Transmitted power for the structure given in Table 5.1

plated tin layer needs to be attached to the aluminum plate and solder patches are used as the bonding layer. Given their low thickness, the solders will have a weak impact on the acoustic transmission between the plate and the tin layers. The full structure is described in Figure 5.5.a.

The transmission has been computed in Figure 5.6 for structures without tin layers, as well as with 100-mm and 200-mm-thick tin layers. The results show that the additional electroplated layers have not been able to bring peaks closer to each other and therefore reduce the amplitude variations. The main issue comes from the fact that tin has a higher acoustic impedance ($Z=24 \text{ MRayl}$) than aluminum ($Z=17 \text{ MRayl}$).

A solution is to isolate the tin layer from the aluminum by adding another high-impedance material between the solder patch and the tin layer by electroplating. nickel stands out as a solution as it is a commonly electroplated material with a high impedance ($Z=50 \text{ MRayl}$). It is consequently placed between the solders and the tin layers. The structure with both electroplated layers on both side of the plate is shown in Figure 5.5.b.

The possibility to bring the three peaks within the bandwidth closer to each other with both electroplated layers is shown in Figure 5.7 for 90- μm -thick nickel and 220- μm -thick tin

layers (structure described in this Table 5.1).

Table 5.1: Configuration of the channel with backing and two electroplated layers

	Thickness	Material
Actuator	500 μm	PZT-5A
Receiver	500 μm	PZT-5A
Plate	3 mm	Aluminum
Backing	7 mm	Tungsten-loaded epoxy (25%)
Bonding	Indium and Pb/Sn	25 μm
Electroplated layer 1	90 μm	Nickel
Electroplated layer 2	220 μm	Tin

The bandwidth constructed around the same three peaks is restricted to 700 kHz, within which the amplitude variations are limited to 2 dB. By bringing peaks together, the two electroplated layers are then capable of enhancing the attenuation provided by the backing. A major drawback can though be identified as the frequency span of the bandwidth has strongly shrunk.

5.4 Reduction of the amplitude variations through an electric impedance in a load circuit

5.4.1 Introduction of an electric load impedance

In addition to the mechanical behavior, electrical aspects can be considered to damp the transmission at resonance frequencies. In [48], Hu et al. described the possibility to adjust the characteristics of an electric impedance Z_r in a load circuit connected to both sides of the receiving transducer and in parallel of the oscilloscope (Figure 4.7). The objective was then to optimize the amount of energy that could be collected by the receiving transducer in order to charge a battery on one side of the barrier.

On the opposite side, the load impedance could also be seen as a means to absorb the acoustic energy traveling through the receiving transducer and therefore oppose the wave motion generating the output voltage. The electric impedance Z_r is constituted of a resistance R_r

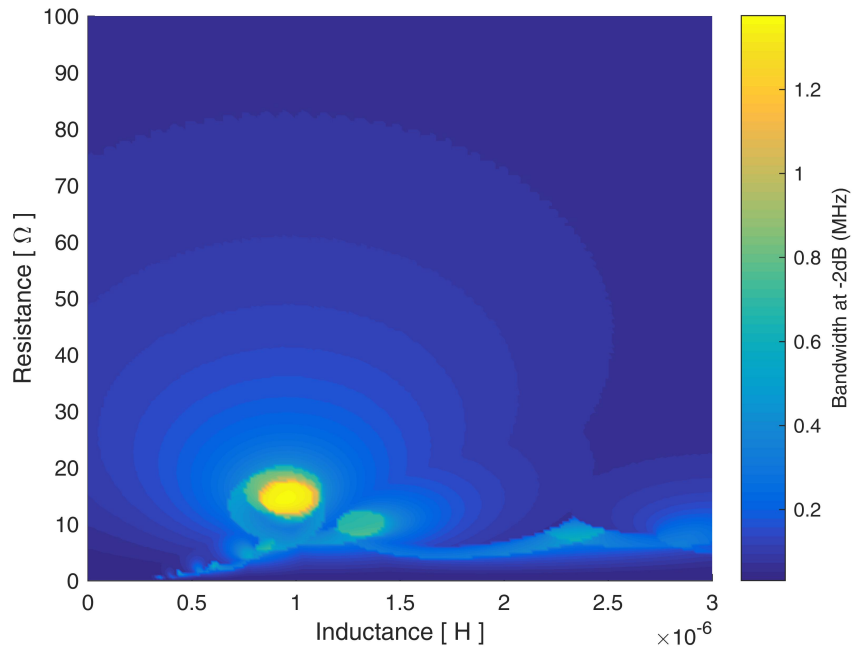


Figure 5.8: Variations of the bandwidth at -2dB for different values of resistance and inductance in the load impedance, for 0.5-mm-thick transducers bonded to a 3-mm-thick aluminum plate by solder patches

in series with an inductance L_r . Its value is given by the expression:

$$Z_r = R_r + jL_r(2\pi f) \quad (5.3)$$

In addition to absorbing the acoustic energy, the electric load also modifies the locations of the resonances, consequently making the derivation of analytical formulas for optimal values of R_r and L_r problematic. The calculation of the desired resistance and inductance values has then been done numerically, by computing the largest bandwidth possible within which the fluctuations were limited to 2 dB (or shortly "bandwidth at -2 dB") over a two-dimensional table of values for R_r and L_r ranging respectively between 0 and 100 Ω , and 0 and 3000 nH. In this configuration, there are no backing or electroplated layers located around the transducers.

Figure 5.8 shows the evolution of the bandwidth at -2 dB with different values of R_r and

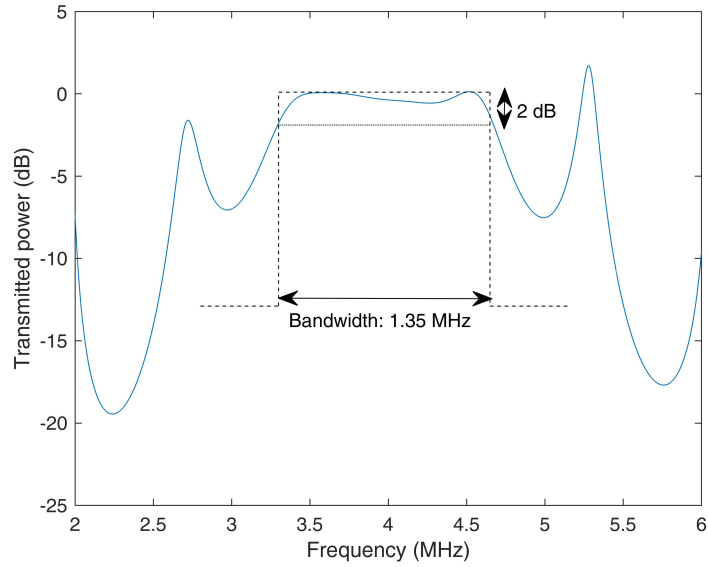


Figure 5.9: Transmitted power for for the structure given in Table 5.2

L_r under the shape of a heat map. The largest bandwidth occurs at $R_r = 14.6\Omega$ and $L_r = 950nH$. Its width reaches 1.35 MHz. It is worth noting the heat map depends on the dimensions of the piezoelectric layers (1cm X 1cm) and would scale back with the surface area of the transducers (for example, dividing the area by two would increase twofold the optimal values of R_r and L_r). Figure 5.9 shows the theoretical transmission obtained with this configuration (structure described in Table 5.2).

Table 5.2: Configuration of the channel with an electric load impedance

	Thickness	Material	Resistance	Inductance
Actuator	500 μm	PZT-5A	/	/
Receiver	500 μm	PZT-5A	/	/
Plate	3 mm	Aluminum	/	/
Backing	no	no	/	/
Bonding	Indium and Pb/Sn	25 μm	/	/
Electroplated layer 1	no	no	/	/
Electroplated layer 2	no	no	/	/
Receiving circuit	/	/	14.6 Ω	950nH

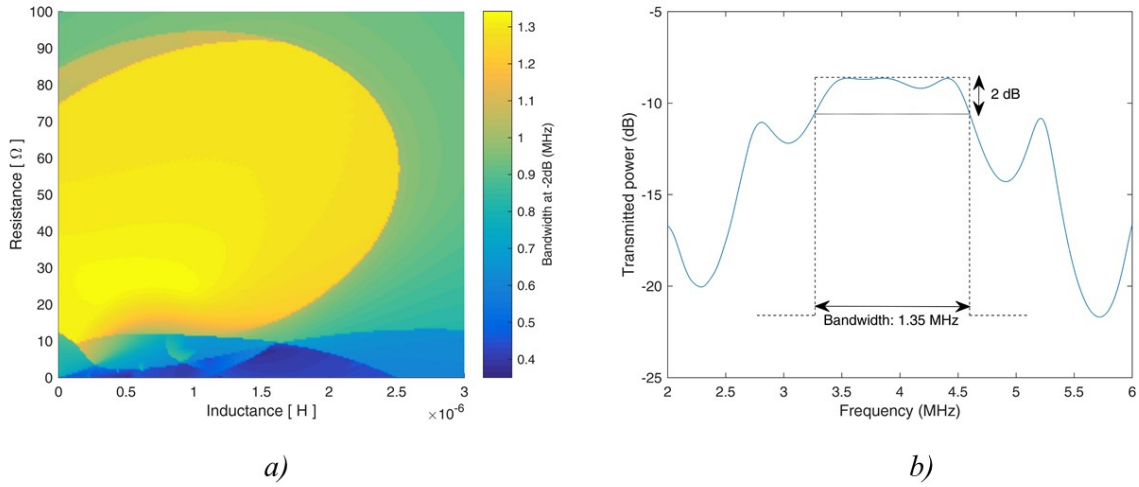


Figure 5.10: (a) Variations of the bandwidth at -2dB for different values of resistance and inductance in the load impedance and (b) Transmitted power for the structure given in Table 5.3

5.4.2 Combination of an electric load impedance and backing layers

It can be noted that the electric load impedance and the backing layers use different mechanisms to attenuate the transmission at the peaks. As a consequence, they could be used concurrently to provide an attenuation strong enough to organize a bandwidth including both resonances located at 2.7 MHz and 5.2 MHz on Figure 5.9.

7-mm-thick layers of epoxy loaded with tungsten (at a 25% volume concentration) have been added on top of the structure introduced in the previous subsection. The theoretical bandwidth at -2 dB has again been computed over the same ranges of values for R_r and L_r and the results have been presented under the form of a heat map in Figure 5.10.a. The largest bandwidth was reached for $R_r = 26.2\Omega$ and $L_r = 560nH$. Under this configuration (presented in Table 5.3), the bandwidth is again spread over 1.35 MHz, but the attenuation was not strong enough to include additional peaks within (Figure 5.10.b).

The additional damping provided by the backing layers could though be noticed in the heat

Table 5.3: Configuration of the channel with backing and an electric load impedance

	Thickness	Material	Resistance	Inductance
Actuator	500 μm	PZT-5A	/	/
Receiver	500 μm	PZT-5A	/	/
Plate	3 mm	Aluminum	/	/
Backing	7 mm	Tungsten-loaded epoxy (25%)	/	/
Bonding	Indium and Pb/Sn	25 μm	/	/
Electroplated layer 1	no	no	/	/
Electroplated layer 2	no	no	/	/
Receiving circuit	/	/	26.2 Ω	560nH

map, as a very large range of inductance and resistance values could offer a bandwidth at -2dB greater than 1.3 MHz, as opposed to the limited range observed previously in Figure 5.8. Wide ranges of possible resistances and inductances offer advantages at the experimental stage as they allow room for inaccuracies in the electric circuits. The major drawback of this configuration comes from the amplitude in the bandwidth, that drops from -2 dB to -11 dB with the addition of the epoxy backing layers.

5.4.3 Combination of an electric load impedance, backing layers and electroplated layers

The previous subsection has shown the limitations of the attenuation capacities obtained from the combination of the impedance load and the backing layer. The bandwidth could not be increased as other peaks external to the bandwidth could not be brought within. On the other hand, appropriate electroplated layers have been shown to be capable of bringing peaks closer to each other.

Consequently, the next step will be to combine both approaches and use a structure made of electroplated Nickel and Tin layers, of loaded-epoxy backings and that includes a load circuit. The bandwidth at -2 dB now needs to be optimized over four parameters (the Tin and Nickel thicknesses, as well as the values of the resistance R_r and L_r in the load circuit). After computing the transmission while varying these four parameters, the optimal thicknesses were 20 μm for the Nickel and 110 μm for the Tin layers. The largest bandwidth was obtained for $R_r = 13\Omega$ and $L_r = 770\text{nH}$ and its frequency span ranged over 2 MHz

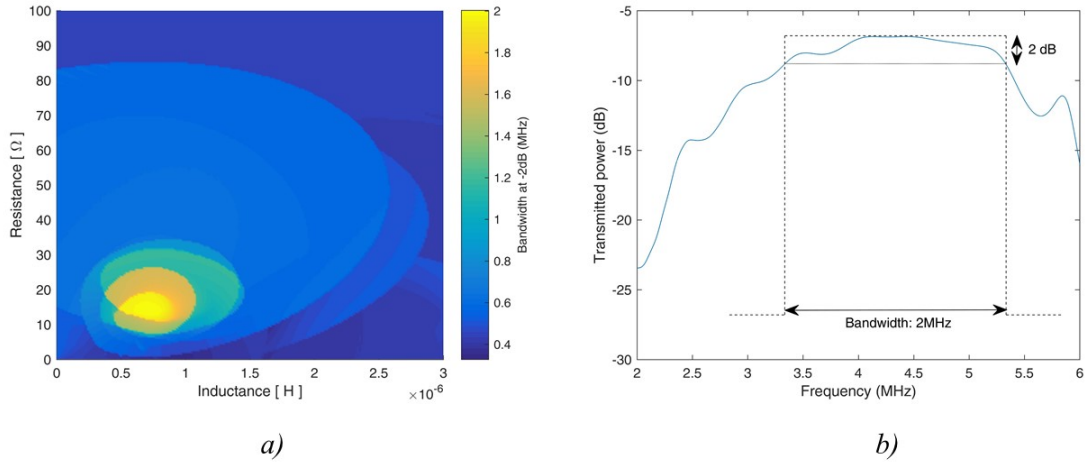


Figure 5.11: (a) Variations of the bandwidth at -2dB for different values of resistance and inductance in the load impedance and (b) Transmitted power for the structure given in Table 5.4

(structure described in Table 5.4).

Table 5.4: Configuration of the channel with backing, electroplated layers and an electric load impedance

	Thickness	Material	Resistance	Inductance
Actuator	500 μm	PZT-5A	/	/
Receiver	500 μm	PZT-5A	/	/
Plate	3 mm	Aluminum	/	/
Backing	7 mm	Tungsten-loaded epoxy (25%)	/	/
Bonding	Indium and Pb/Sn	25 μm	/	/
Electroplated layer 1	20 μm	Nickel	/	/
Electroplated layer 2	110 μm	Tin	/	/
Receiving circuit	/	/	13 Ω	770nH

Figure 5.11.a shows the heat map while varying the resistance and inductance in the load circuit for the optimal thicknesses of Nickel and Tin. It can be noted again that the range of R_r and L_r that includes large bandwidths at -2 dB is narrow, which could generate difficulties at the experimental stage. The transmission obtained with the optimal configuration is given in Figure 5.11.b. The bandwidth described is much wider than the ones obtained

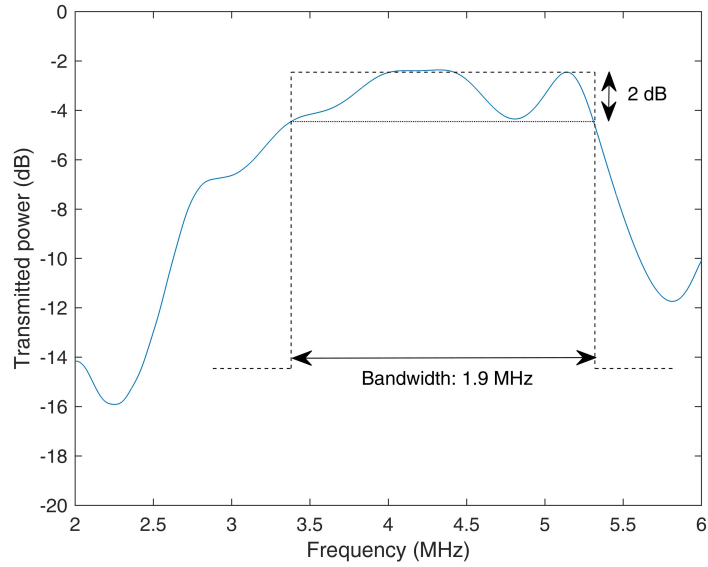


Figure 5.12: Transmitted power for the structure given in Table 5.5

previously in this chapter. However, the amplitude of its transmission only reaches -9 dB.

5.5 Combination of electric impedances on both the actuating and receiving circuits

While a load circuit has been added to the receiving transducer to oppose the wave motion within, there has not been an equivalent approach with the actuating transducer yet. Given that the actuator is in close-circuit, the additional impedance in the actuating circuit would need to be in series with both the generator and the transducer. This configuration is represented on Figure 4.7.

The electric impedance Z_a in the actuating circuit is given as:

$$Z_a = R_a + jL_a(2\pi f) \quad (5.4)$$

where R_a and L_a are respectively the resistance and inductance constituting the electric impedance. They are mounted in series in the circuit connected to the actuator. Controlling the electric impedance in the actuating circuit is more challenging than in the receiving cir-

cuit as generators usually contain an internal resistance. An alternate approach to remove this internal resistance would be to use an operational amplifier as the voltage source.

Electroplated layers have not been used in this section as they did not bring any improvement to the bandwidth, but an impedance is still used in the receiving load circuit. 7-mm-thick loaded epoxy backings are also placed over the transducers. Consequently, the bandwidth at -2 dB needs to be optimized over four parameters (R_a , R_r , L_a and L_r). After computing the transmission while varying these four parameters, the optimal resistance and impedance values were $R_a = 7\Omega$, $L_a = 670nH$, $R_r = 24\Omega$, $L_r = 1080nH$ (structure described in Table 5.5).

Table 5.5: Configuration of the channel with loaded backing and electric actuating and load impedances

	Thickness	Material	Resistance	Inductance
Actuator	500 μm	PZT-5A	/	/
Receiver	500 μm	PZT-5A	/	/
Plate	3 mm	Aluminum	/	/
Backing	7 mm	Tungsten-loaded epoxy (25%)	/	/
Bonding	Indium and Pb/Sn	25 μm	/	/
Electroplated layer 1	no	no	/	/
Electroplated layer 2	no	no	/	/
Actuating circuit	/	/	7 Ω	670nH
Receiving circuit	/	/	24 Ω	1080nH

The transmitted power under this configuration is given by Figure 5.12 and presents a bandwidth at -2 dB of 1.9 MHz.

The attenuation achieved by both electric impedances is strong enough to simply use unloaded epoxy as a backing layer. Under this configuration, the used resistance and impedance values were $R_a = 5\Omega$, $L_a = 880nH$, $R_r = 18.5\Omega$, $L_r = 880nH$ (structure described in Table 5.6) and a bandwidth at -2 dB of 2.15 MHz could be reached (Figure 5.13).

In addition, by switching to unloaded epoxy, a transmission at a magnitude of -0.5 dB could be reached within this bandwidth, therefore making this configuration the most efficient in terms of bandwidth and transmission.

Table 5.6: Configuration of the channel with unloaded backing and electric actuating and load impedances

	Thickness	Material	Resistance	Inductance
Actuator	500 μm	PZT-5A	/	/
Receiver	500 μm	PZT-5A	/	/
Plate	3 mm	Aluminum	/	/
Backing	10 mm	Unloaded epoxy	/	/
Bonding	Indium and Pb/Sn	25 μm	/	/
Electroplated layer 1	no	no	/	/
Electroplated layer 2	no	no	/	/
Actuating circuit	/	/	5 Ω	880nH
Receiving circuit	/	/	18.5 Ω	880nH

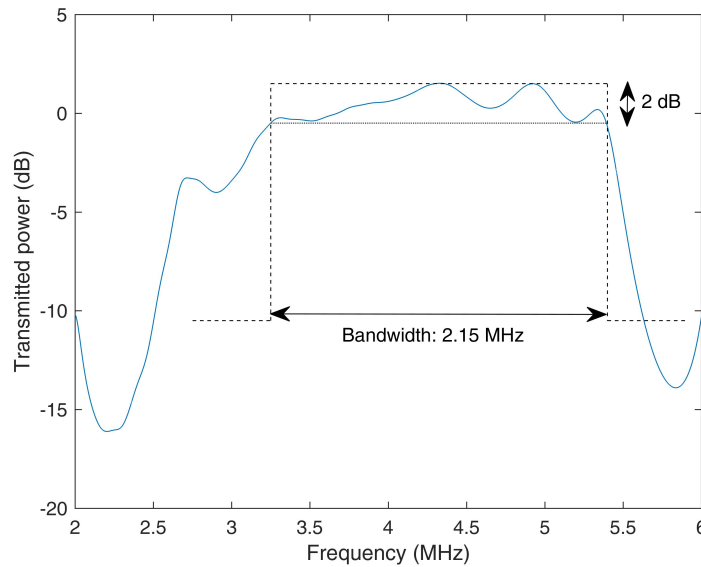


Figure 5.13: Transmitted power for the structure given in Table 5.6

5.6 Conclusion

Different methods aiming at reducing the variations of the transmitted power within a given bandwidth have been introduced in this chapter. These approaches can be either:

- Mechanical, by adding backing layers encapsulating the transducers in order to trap the waves reaching the free surfaces of the piezoelectric layers. The best performances were theoretically obtained by epoxy loaded with tungsten powder. Besides, additional electroplated layers have been added under the transducers to bring the

peaks closer to each other and therefore limit the amplitude drop between them.

- Electrical, by using an impedance (resistance in series with an inductance) in a load circuit in parallel with the measuring device. This approach has further been extended to the use of an electric impedance in the circuit connected to the actuating transducer.

Given the objective of obtaining the largest bandwidth at -2 dB possible, the best configurations were obtained by using a combination of both the mechanical and electrical approaches. A configuration using tungsten-loaded epoxy, electroplated layers and an electrical impedance in the receiving load circuit enabled a bandwidth of 2 MHz. Another one using unloaded epoxy, as well as electric impedances in both circuits connected to the actuator and the receiver reached a bandwidth of 2.15 MHz.

CHAPTER 6

WIDEBAND ACOUSTIC DATA TRANSMISSION AT HIGH FREQUENCIES THROUGH STAIRCASE PIEZOELECTRIC TRANSDUCERS

6.1 Overview

After previously developing different approaches intending to reduce the amplitude variations at low carrier frequencies (under 10 MHz), this chapter will focus in fulfilling the same objective for high-frequencies channels (in the range of hundreds of MHz). The motivation has been to target very large bandwidths (around 100 MHz) while using thick piezoelectric transducers to prevent them from drawing an extensive amount of current from the generator.

An alternate design in the shape of a staircase has been developed and combines the outputs associated with each step to mitigate the amplitude variations over large frequency spans. After showing these capabilities through finite element models, analytical models have been developed to characterize the electric and mechanical behavior of such a structure. Its limitations have been studied and different approaches have been developed to obtain a configuration capable of covering a bandwidth at -3 dB larger than 100 MHz.

6.2 Wide bandwidth at high frequency

The previous two chapters have been focused on acoustic transmission at frequencies below 10 MHz, consequently limiting the achievable bandwidths to the range of the Mega Hertz. The enhancement of the rate of data transmission therefore relies on the use of higher carrier frequencies. The objective of this chapter will be to derive a configuration enabling data transmission through a bandwidth of 100 MHz, while keeping the amplitude variations under 3 dB within.

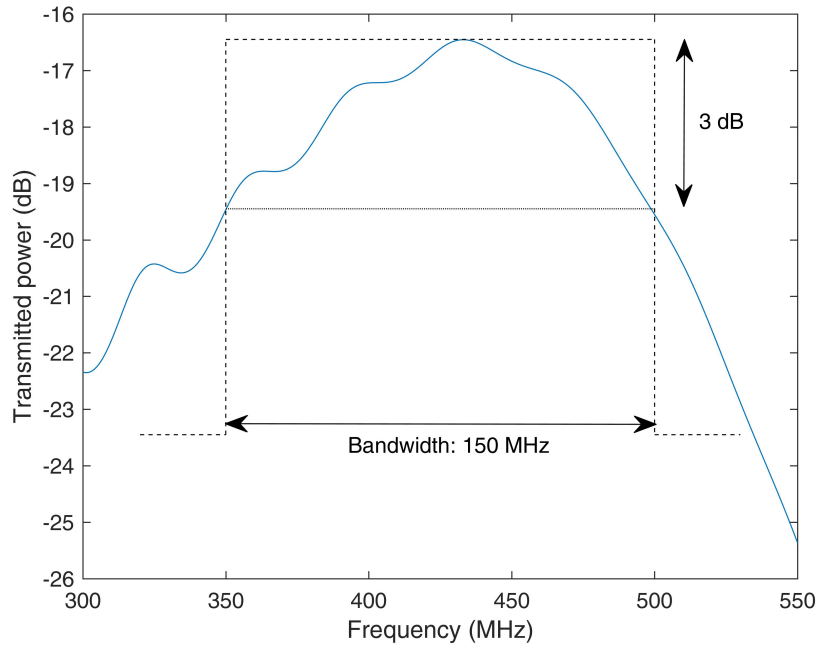


Figure 6.1: Transmitted power for 4- μm -thick transducers bonded to a 3-mm-thick aluminum plate

An obvious solution would be to use thin piezoelectric films with a fundamental resonance at the center of the targeted bandwidth. For example, Figure 6.1 shows the transmitted power obtained with 4- μm -thick piezoelectric transducers bonded to a 3-mm-thick aluminum plate. For this thickness, the transducers are assumed to be directly sputtered on the plate, therefore eliminating the necessity of a bonding layer. A 150-MHz-bandwidth at 3 dB can be defined between 350 MHz and 500 MHz, therefore satisfying the objective. However, piezoelectric layers are characterized by an electric capacitance C_0 inversely proportional their thickness L :

$$C_0 = \frac{\epsilon_{33}A}{L} \quad (6.1)$$

where ϵ_{33} is the permittivity of the piezoelectric material and A is its cross-section. As a consequence, films with low thicknesses are characterized by a high capacitance and would therefore draw a high electric current that generators would struggle to provide.

Thicker transducers are then required to design the communication channels. The trans-

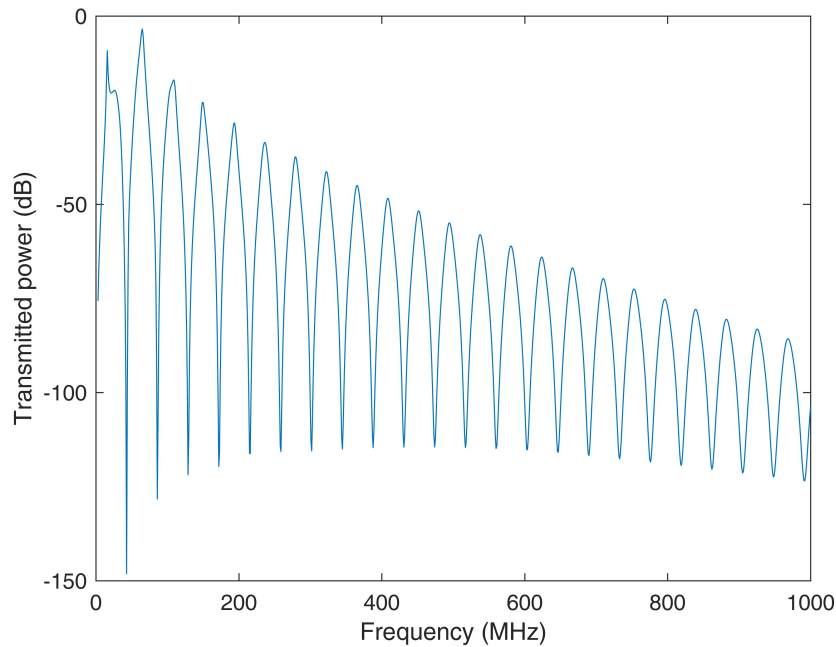


Figure 6.2: Transmitted power for 100- μm -thick transducers bonded to a 3-mm-thick aluminum plate

mission for 100- μm -thick transducers is given in Figure 6.2 and shows an output divided in multiple resonances. Each peaks is characterized by a low width and only narrow bandwidths at -3 dB (in the range of the Mega Hertz) can be distinguished within. Such a configuration is then unsuitable for the expected high data-rate transmission and the structure will be adapted to meet this objective.

6.3 Angled and staircase transducers

Under the target of using a frequency span of 100 MHz with limited amplitude variations, the associated bandwidth would need to overlap anti-resonances. The different strategies for bandwidth enhancement introduced in the previous chapter were based on the concept of "flattening" the transmission around the fundamental resonance of the transducers and are therefore not adapted for this new purpose.

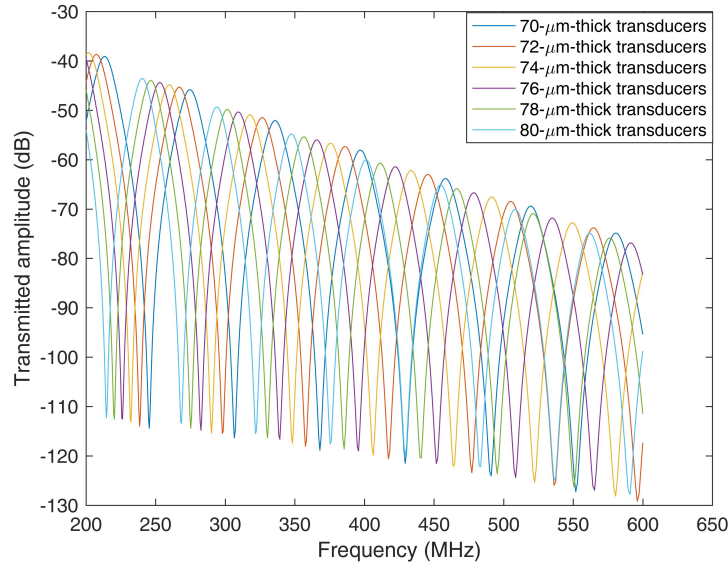


Figure 6.3: Transmitted power for transducers of different thicknesses (70, 72, 74, 76, 78 and 80 μm) bonded to a 3-mm-thick aluminum plate

The positions of the anti-resonances are given as:

$$f_{A_n} = \frac{n}{l_{piezo}} \sqrt{\frac{c_{33 piezo} + \frac{e_{33 piezo}^2}{\epsilon_{33 piezo}}}{\rho_{piezo}}} \quad n = 1, 2, 3, \dots \quad (6.2)$$

They only depend on the material characteristics and the thickness of the piezoelectric layers. As a consequence, the addition of other layers in the structure would not enable to overlap the anti-resonances. On the other hand, Figure 6.3 represents the transmitted power for piezoelectric layers of different thicknesses (from 70 to 80 μm) bonded to a 1-mm-thick aluminum plate and shows that it is possible to shift the positions of the anti-resonances by modifying the thicknesses of the transducers. Besides, the similar shift of the resonances suggests the possibility that the association of channels with transducers of difference thicknesses can lead to an output with reduced amplitude variations on a bandwidth overlapping anti-resonances.

Figure 6.4.a presents a structure of six channels with transducers of identical cross-sections but different thicknesses (70, 72, 74, 76, 78 and 80 μm). All the channels are electrically

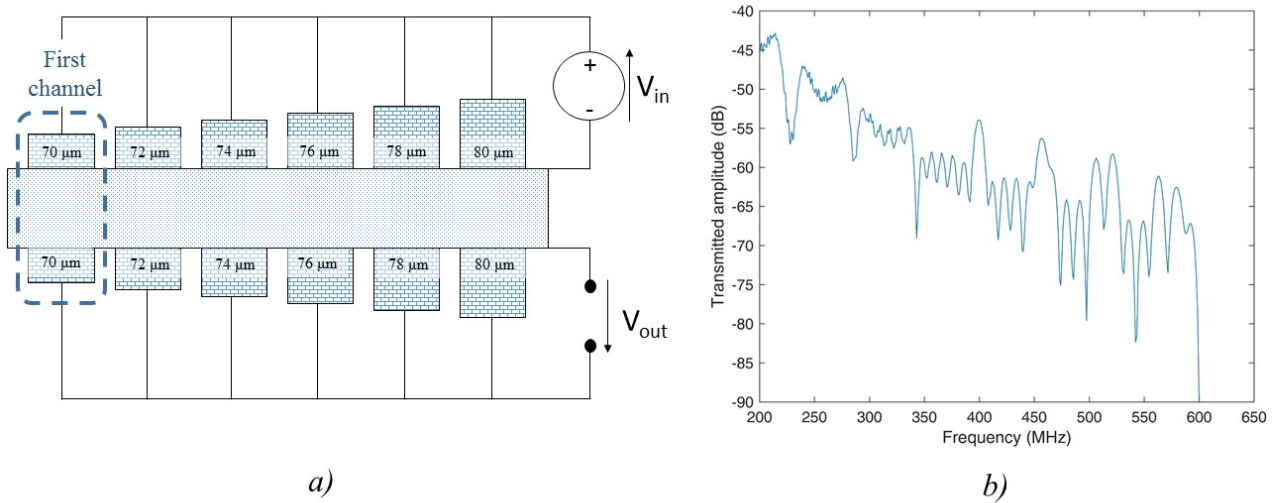


Figure 6.4: (a) Representation of the structure for acoustic data transmission by piezoelectric transduction with six channels of different transducer thicknesses and (b) Associated transmitted power

connected to the same generator and oscilloscope. The corresponding transmitted power is given in Figure 6.4.b (the computation method for the output is presented in the next section). Under this configuration, it is possible to define bandwidths within which the amplitude variations are more limited, but still greater than 3 dB. An increase of the number of channels is consequently necessary to smooth the shape of the obtained output. However, by raising the number of transducers in the array, the overall area filled by the channels would increase. In addition to the increased amount of space necessary to run the transmission operations, the total capacitance of the full structure would rise, therefore removing the benefits of choosing thick transducers for that prospect.

A more compact solution would be to use a single transducer with a varying thickness in the shape of a staircase (Figure 6.5.b). The transducer is divided into N steps, with a thickness varying between L_{min} and L_{max} . The total width of the structure is w and the total thickness variation is $\Delta L = L_{max} - L_{min}$. A similar option consists in flattening the upper

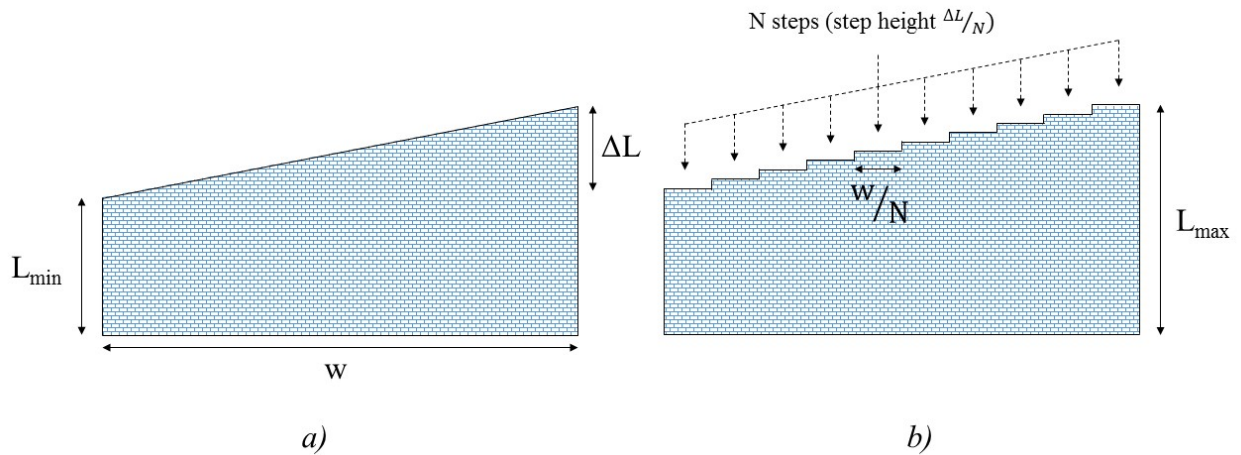


Figure 6.5: a) Angled, b) Staircase-shaped transducer

face of the piezoelectric layer (Figure 6.5.a) in order to obtain an "angled" transducer.

The transmitted power obtained from 2D Finite Elements models (on COMSOL) have been compared for a staircase (14 steps) and an angled transducer ($L_{min} = 70\mu m$, $L_{max} = 80\mu m$) in Figure 6.6. They show the possibility of defining a 100-MHz-bandwidth with limited amplitude fluctuations between 350 and 450 MHz. Approaches relative to the attenuation of the remaining variations will be tackled in the fifth section of this chapter.

6.4 Analytical expression of the output

6.4.1 Extension of the Mason model

An analytical model has been derived to express more efficiently the electro-mechanical behavior of the structures with the angled/staircase transducers. In the case of staircase transducers of N steps (Figure 6.7), the structure can be divided laterally into N frameworks under each step with independent mechanical behaviors, while the front and back electrodes of all the steps are electrically connected together. The Mason model can then be extended

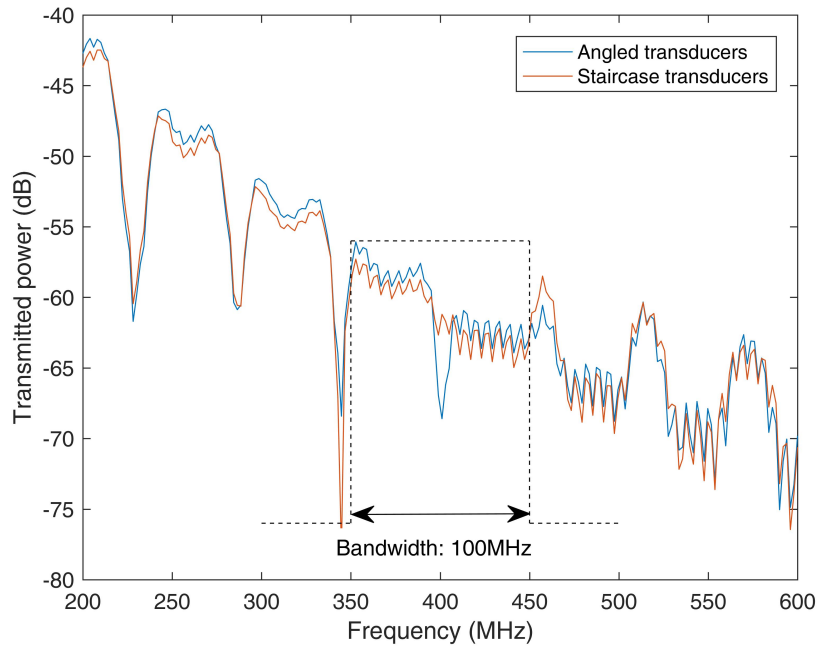


Figure 6.6: Comparison of the theoretical transmitted power for staircase (14 steps) and angled transducers ($L_{min} = 70\mu m$, $L_{max} = 80\mu m$) bonded to a 1-mm-thick aluminum plate with 1-mm-thick loaded epoxy baking layers

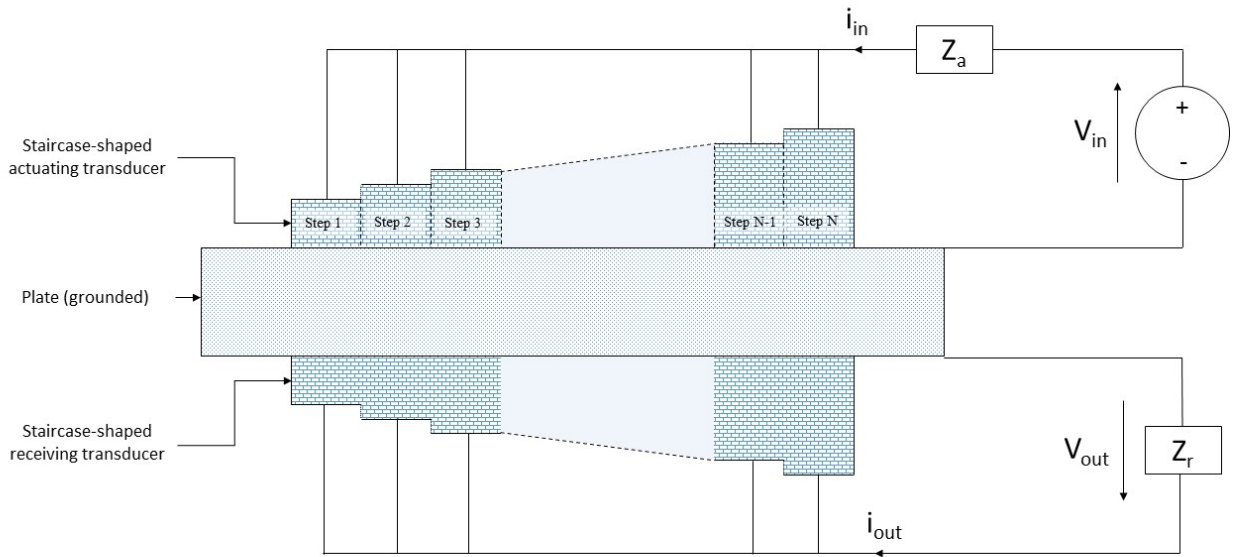


Figure 6.7: Representation of the structure for acoustic data transmission by piezoelectric transduction with staircase-shaped transducers

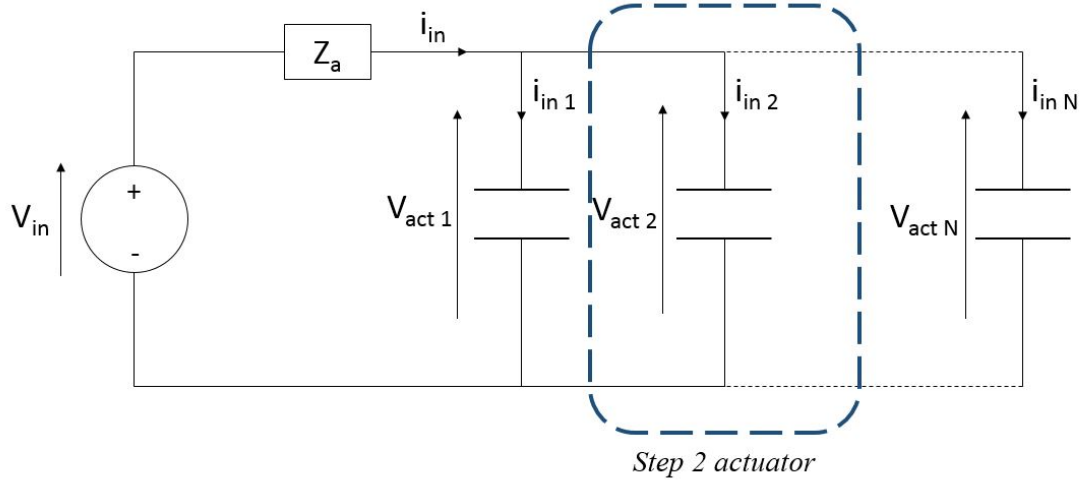


Figure 6.8: Electric representation of the staircase-shaped actuator and the connected circuit

to account for the acoustic transmission in each framework while considering the entire electric circuitry connecting the electrodes. In the case of angled transducers, the structure needs to be discretized into steps to acknowledge the one-dimensional characteristic of the Mason model. The analytical model is therefore equivalent to the one of the staircase transducers. The required number of steps can be defined numerically by increasing it until reaching a convergence in the results.

Two different representations of the transducers have been used to develop this model:

- In the actuator (Figure 6.8), each step receives the same voltage emitted from the generator but share the induced current. Each increment of the staircase is therefore represented by its internal capacitance C_i in parallel with the capacitances of the other steps. The value of C_i is given as:

$$C_i = \frac{\epsilon_{33} A_i}{L_i} \quad (6.3)$$

where A_i and L_i are the cross-section and thickness of the i -th step. The i -th capacitance is fed by the current $i_{in i}$ and withstand a difference of potential $V_{act i}$. The

relations between the different currents and voltages are given as:

$$i_{in} = \sum_{j=1}^N i_{in j} \quad (6.4)$$

$$V_{act 1} = V_{act 2} = \dots = V_{act N} = V_{in} - Z_a i_{in}$$

By combining the two expressions of Equation 6.4, the electric current in the i -th branch of the circuit is given by:

$$i_{in i} = i_{in} \frac{C_i}{\sum_{j \neq i} C_j} \quad (6.5)$$

where $\sum_{j \neq i} C_j$ represent the sum of the capacitance of the other steps. By assuming that the difference of heights between the different steps is much weaker than their average thickness and that the number of steps is sufficient, the expression $\sum_{j \neq i} C_j$ can be approximated by C_{tot} :

$$\sum_{j \neq i} C_j \approx C_{tot} = \frac{\epsilon_{33} A_{tot}}{L_{av}} \quad (6.6)$$

where A_{tot} is the sum of the cross-sections of each step from the transducer and $L_{av} = \frac{L_{min} + L_{max}}{2}$ is the average thickness of the transducer. Therefore, the expression for the current going through the i -th step is:

$$i_{in i} = i_{in} \frac{C_i}{C_{tot}} \quad (6.7)$$

- In the receiver, each step generates electric energy from the piezoelectric effect and is represented as a current source in parallel with its internal capacitance C_i (Figure 6.9). The current leaving the i -th step is denoted as $i_{out i}$.

While the electric potentials on the front and back surfaces are equal for all the stair-

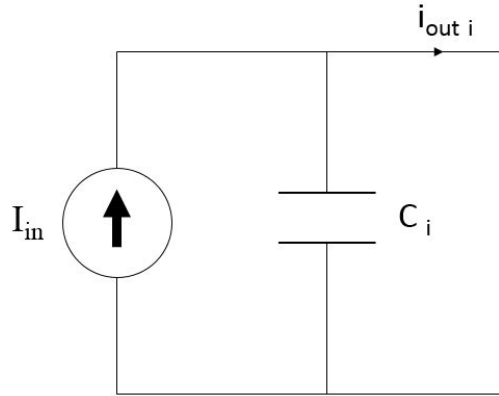


Figure 6.9: Electric representation of one step of the receiving transducer

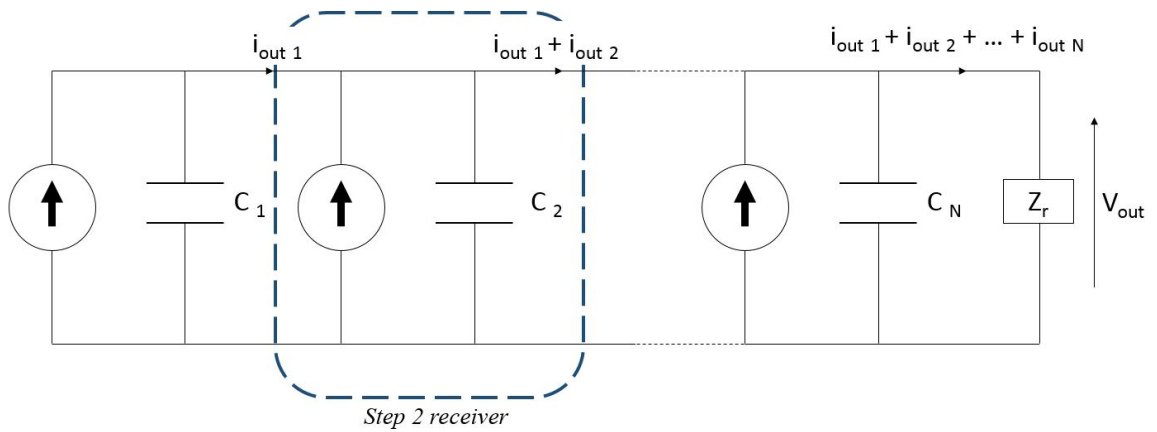


Figure 6.10: Electric representation of the staircase-shaped receiver and the connected load circuit

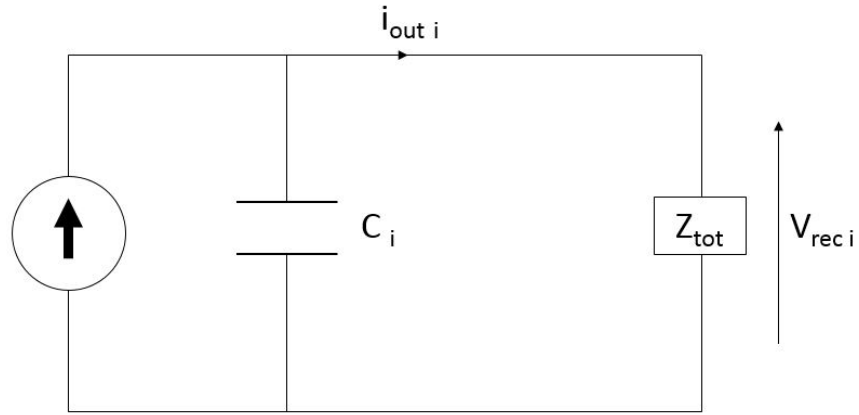


Figure 6.11: Electric representation of the staircase-shaped receiver and the connected load circuit under the assumption that the acoustic transmission is limited to the i -th step

case increments, each step provides the load circuit with a different current which depends on the acoustic transmission happening from the facing actuator step. Consequently, in the receiver, all the steps are set in parallel of each other (Figure 6.10)

For a transducer of constant thickness, Equation 4.45 provided an expression relating the output voltage and current with the input voltage and current. This expression has been used again to relate the output characteristics to their input for each single step of the staircase-shaped structure. In the following calculations, the transmission has been calculated only for the i -th step, before summing the outputs at the last stage.

In the actuator, the input voltage and current in the i -th step are given as:

$$\begin{bmatrix} V_{act\ i} \\ i_{act\ i} \end{bmatrix} = \begin{bmatrix} V_{in} - Z_a i_{in} \\ i_n \frac{C_i}{C_{tot}} \end{bmatrix} \quad (6.8)$$

In the receiver, the only current source is located at the i -th step considering that the only acoustic transmission occurs through this staircase increment. The electric representation of all the other steps can therefore be limited to a capacitance and the equivalent circuit is given in Figure 6.11. Z_{tot} is the equivalent impedance of the load Z_r in parallel with the sum of the internal capacitance of the $(N-1)$ other steps. By injecting the expression 6.6,

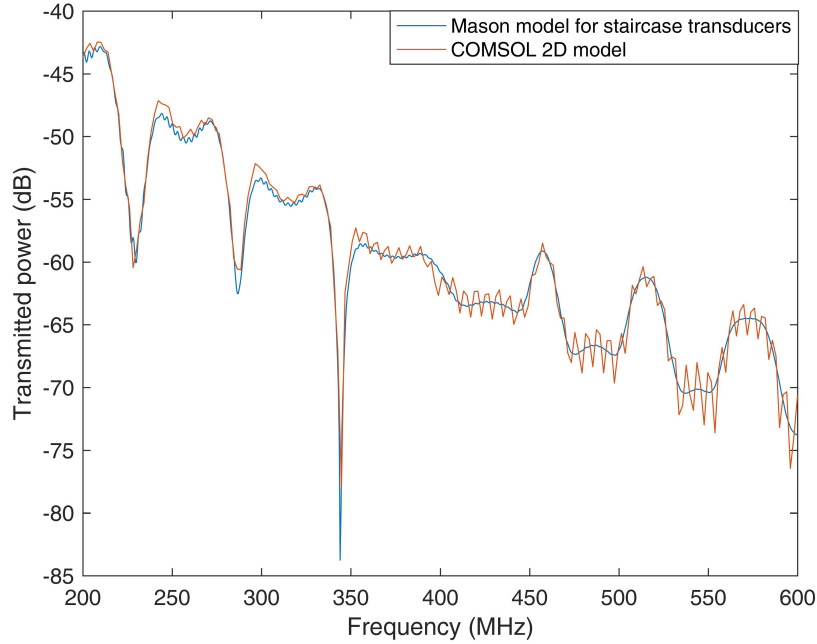


Figure 6.12: Comparison of the transmitted power given by the extension of the Mason for staircase transducers with a FEM COMSOL 2D model for a staircase transducer (thickness ranging between 70 and 80 μm over 14 steps) bonded to a 1-mm-thick aluminum plate

Z_{tot} is given as:

$$Z_{tot} = \frac{Z_r}{1 + jZ_r 2\pi f C_{tot} \frac{N-1}{N}} \quad (6.9)$$

In the receiver, the output voltage and current in the i -th step are therefore given as:

$$\begin{bmatrix} V_{rec\ i} \\ i_{out\ i} \end{bmatrix} = \begin{bmatrix} -Z_{tot} i_{out\ i} \\ i_{out\ i} \end{bmatrix} \quad (6.10)$$

The input/output relation is then given by:

$$\begin{bmatrix} -Z_{tot} i_{out\ i} \\ i_{out\ i} \end{bmatrix} = [T_{tot}^i] \begin{bmatrix} V_{in} - Z_a i_{in} \\ i_n \frac{C_i}{C_{tot}} \end{bmatrix} = \begin{bmatrix} T_{tot11}^i & T_{tot12}^i \\ T_{tot21}^i & T_{tot22}^i \end{bmatrix} \begin{bmatrix} V_{in} - Z_a i_{in} \\ i_n \frac{C_i}{C_{tot}} \end{bmatrix} \quad (6.11)$$

where the expression of $[T_{tot}^i]$ is obtained by using the dimensions of the i -th step in the expression 4.46. By solving the matrix equation 6.11, the following expression of $i_{out\ i}$ is

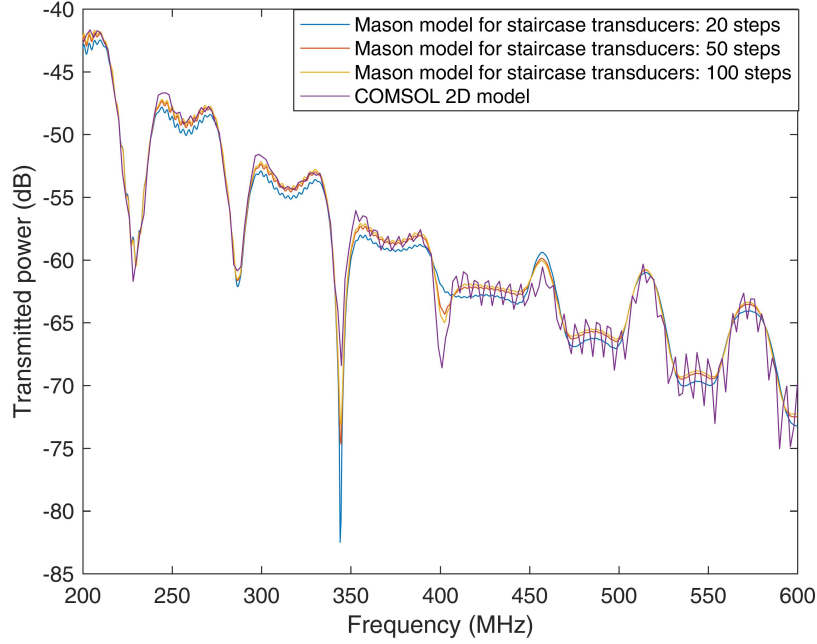


Figure 6.13: Comparison of the transmitted power given by the extension of the Mason for staircase transducers (for 20, 50 and 100 steps) with a FEM COMSOL 2D model for an angled transducer (thickness ranging between 70 and 80 μm) bonded to a 1-mm-thick aluminum plate

obtained:

$$i_{out\ i} = \frac{C_i(T_{11}^i T_{22}^i - T_{12}^i T_{21}^i)}{C_i T_{12}^i - C_{tot} T_{11}^i Z_a + C_i T_{22}^i Z_{tot} - C_{tot} T_{21}^i Z_a Z_{tot}} V_{in} \quad (6.12)$$

By summing the output currents from each branch $i_{out\ i}$ and computing the output voltage through the equivalent impedance Z_t , the output voltage is given as:

$$V_{out} = \sum_{i=1}^N \frac{C_i(T_{11}^i T_{22}^i - T_{12}^i T_{21}^i) Z_t}{C_i T_{12}^i - C_{tot} T_{11}^i Z_a + C_i T_{22}^i Z_{tot} - C_{tot} T_{21}^i Z_a Z_{tot}} V_{in} \quad (6.13)$$

This analytical model has been verified by comparing its results to the ones obtained from a FE 2D model for a staircase transducer (thickness ranging between 70 and 80 μm over 14 steps) bonded to a 1-mm-thick aluminum plate. The Finite Elements computations have been carried out on COMSOL. The results shown in Figure 6.12 show a good agreement and confirm the possibility to suggest a bandwidth with reduced vibrations between 340 and 440 MHz.

The angled transducers are characterized by a continuous increase in thickness and consequently need to be discretized into a staircase-shape to be described by the Mason model. The FE model of an angled transducer (thickness ranging between 70 and 80 μm) bonded to a 1-mm-thick aluminum plate has been compared to the Mason models associated with staircase structures of 20, 50 and 100 steps in Figure 6.13. The analytical results converge beyond 50 steps and are similar to the FE results.

6.4.2 Derivation of an analytical expression through Fourier Transform considerations

The complexity of the modified Mason model prevents it from contributing to a simple analytical expression that could describe the different features seen in Figure 6.12 and how to improve the transmission. A different approach describing the transducers through Fourier Transforms in the spatial domain has therefore been developed.

A simplified representation of a transducer of thickness L in the wave-number domain is given by:

$$G_1(k) = \text{sinc}\left(\frac{kL}{2}\right)e^{\frac{ikL}{2}} \quad (6.14)$$

where $\text{sinc}\left(\frac{kL}{2}\right)$ is the amplitude variation with frequency and $e^{\frac{ikL}{2}}$ describes the phase difference due to the traveling time through the transducer. Its equivalent representation in the spatial domain is obtained by taking the Fourier Transform of $G_1(k)$:

$$\hat{G}_1(x) = \mathcal{F}(G_1(k)) = \frac{\sqrt{2\pi}}{L} (H(x+L) - H(x)) \quad (6.15)$$

where H is the Heaviside step function. Therefore, the representation of an assembly of two transducers (actuator and transducer) in the wave-number ($G_2(k)$) and spatial domain ($\hat{G}_2(x)$) are obtained respectively by applying the self-product and autocorrelation of the

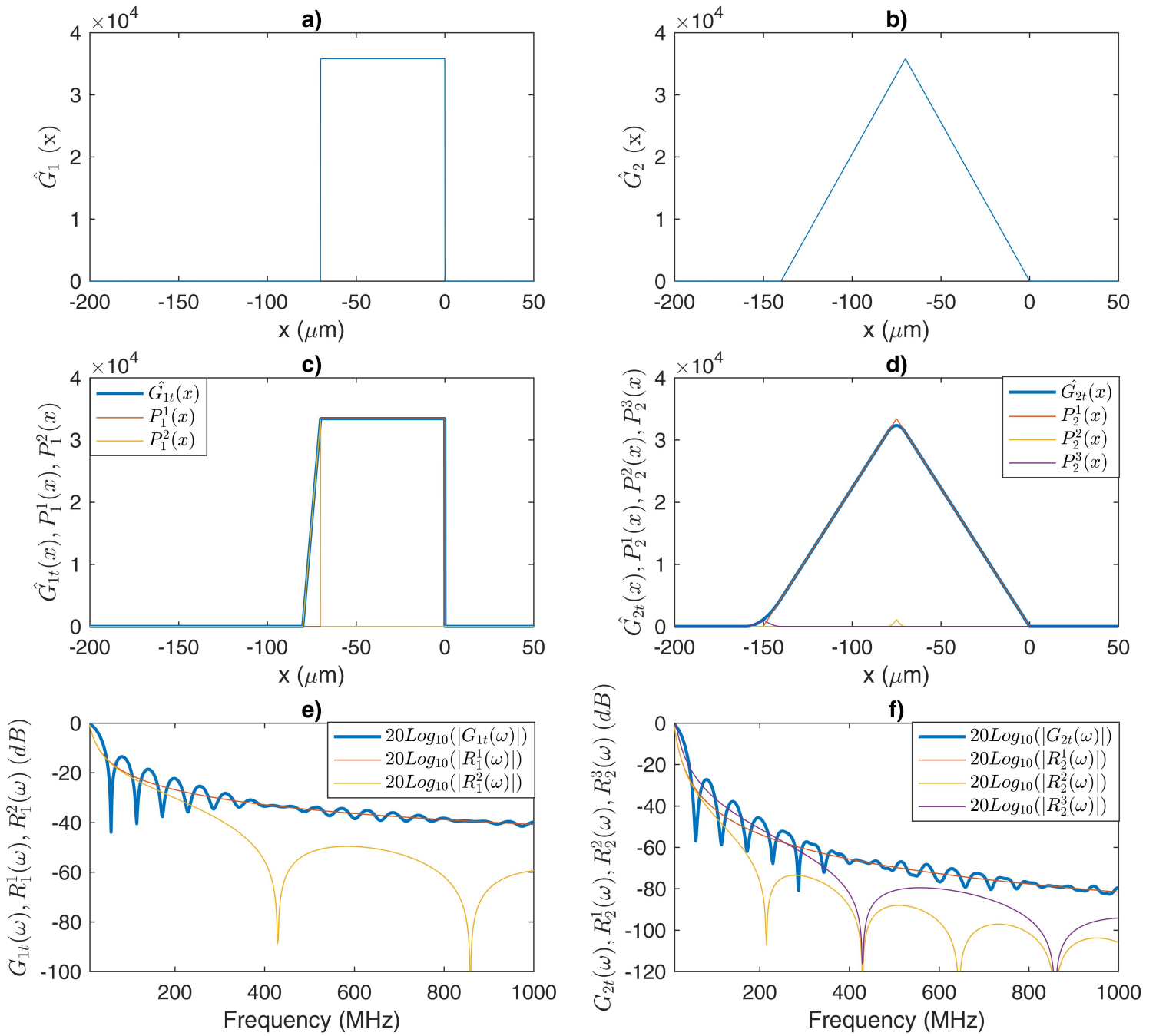


Figure 6.14: Representation of a) $\hat{G}_1(x)$, b) $\hat{G}_2(x)$ for a 70- μm -thick transducer, of c) $\hat{G}_{1t}(x)$, d) $\hat{G}_{2t}(x)$ for transducers with thicknesses ranging between 70 and 80 μm , of e) $G_{1t}(\omega)$, f) $G_{2t}(\omega)$ (in dB) for the same configuration

previous functions:

$$\begin{aligned} G_2(k) &= (G_1(k))^2 = \text{sinc}^2\left(\frac{kL}{2}\right)e^{ikL} \\ \hat{G}_2(x) &= \hat{G}_1(x) \otimes \hat{G}_1(x) = \frac{\sqrt{2\pi}}{L} \Lambda\left(\frac{x+L}{L}\right) \end{aligned} \quad (6.16)$$

where Λ is the triangular function defined as:

$$\Lambda(y) = \begin{cases} 1 - |x| & \text{if } |x| < 1 \\ 0 & \text{otherwise} \end{cases} \quad (6.17)$$

$\hat{G}_1(x)$ and $\hat{G}_2(x)$ are represented in Figures 6.14.a and 6.14.b for $L = 70\mu\text{m}$.

In the case of staircase transducers made of N steps of thicknesses L_i , the design in the spatial domain is given as:

$$\begin{aligned} \hat{G}_{1t}(x) &= \frac{1}{N} \sum_{i=1}^N \frac{\sqrt{2\pi}}{L_i} (H(x + L_i) - H(x)) \\ \hat{G}_{2t}(x) &= \frac{1}{N} \sum_{i=1}^N \frac{\sqrt{2\pi}}{L_i} \Lambda\left(\frac{x + L_i}{L_i}\right) \end{aligned} \quad (6.18)$$

where \hat{G}_{1t} and \hat{G}_{2t} are the design for staircase structures associated respectively with one and two transducers. These expressions can be simplified by assuming that $\Delta L \ll L_{av}$, and therefore considering the height of each Heaviside and triangular functions as constant:

$$\begin{aligned} \hat{G}_{1t}(x) &\approx \frac{1}{N} \sum_{i=1}^N \frac{\sqrt{2\pi}}{L_{av}} (H(x + L_i) - H(x)) \\ \hat{G}_{2t}(x) &\approx \frac{1}{N} \sum_{i=1}^N \frac{\sqrt{2\pi}}{L_{av}} \Lambda\left(\frac{x + L_i}{L_i}\right) \end{aligned} \quad (6.19)$$

When N tends toward infinity, these expressions can be simplified into:

$$\begin{aligned}
\hat{G}_{1t}(x) &= \underbrace{\frac{\sqrt{2\pi}}{L_{av}}(H(x + L_{min}) - H(x))}_{P_1^1(x)} + \underbrace{\frac{\sqrt{2\pi}}{L_{av}} \frac{x + L_{max}}{\Delta L} (H(x + L_{max}) - H(x + L_{min}))}_{P_1^2(x)} \\
\hat{G}_{2t}(x) &= \underbrace{\frac{\sqrt{2\pi}}{L_{av}} \Lambda\left(\frac{x + L_{av}}{L_{av}}\right)}_{P_2^1(x)} - \underbrace{\frac{\sqrt{2\pi}\Delta L}{4L_{av}^2} \Lambda\left(\frac{x + L_{av}}{0.5\Delta L}\right)^2}_{P_2^2(x)} + \underbrace{\frac{\sqrt{2\pi}\Delta L}{4L_{av}^2} \Lambda\left(\frac{x + 2L_{av}}{\Delta L}\right)^2}_{P_2^3(x)}
\end{aligned} \tag{6.20}$$

$\hat{G}_{1t}(x)$ and $\hat{G}_{2t}(x)$, as well as their decompositions, are represented in Figures 6.14.c and 6.14.d for $L_{av} = 75\mu m$ and $\Delta L = 10\mu m$ ($L_{min} = 70\mu m$ and $L_{max} = 80\mu m$).

Their equivalent representation in the wave-number domain is obtained through the Inverse Fourier Transform (IFT):

$$\begin{aligned}
G_{1t}(k) &= \mathcal{F}^{-1}(\hat{G}_{1t}(x)) = -\frac{j}{kL_{av}} + \frac{\exp(jkL_{max}) - \exp(-jkL_{min})}{\Delta L k^2 L_{av}} \\
\hat{G}_{2t}(k) &= \mathcal{F}^{-1}(\hat{G}_{2t}(x)) = -\frac{1}{k^2 L_{av}^2} + \frac{j}{2\Delta L L_{av}^2 k^3} (\exp(2jL_{max}k) - \exp(2jL_{min}k)) - \\
&\quad \frac{2j}{\Delta L L_{av}^2 k^3} (\exp(jL_{max}k) - \exp(jL_{min}k))
\end{aligned} \tag{6.21}$$

By relating the wave numbers to the pulsations through the wave velocity ($k = \frac{\omega}{c}$), expressions describing the behavior of a single transducer ($G_{1t}(\omega)$) and of the association

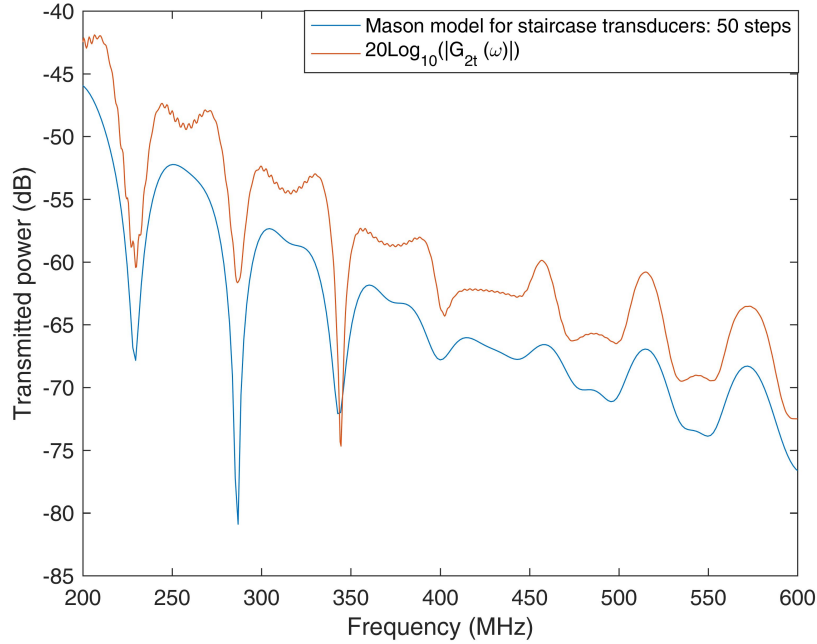


Figure 6.15: Comparison of the transmitted power given by $G_{2t}(\omega)$ with the extension of the Mason for staircase transducers (50 steps) for an angled transducer (thickness ranging between 70 and 80 μm) bonded to a 1-mm-thick aluminum plate

Actuator/Receiver ($G_{2t}(\omega)$) are given as:

$$\begin{aligned}
 G_{1t}(\omega) &= \underbrace{-\frac{jc}{\omega L_{av}}}_{R_1^1(\omega)} + \underbrace{c^2 \frac{\exp(\frac{j\omega L_{max}}{c}) - \exp(\frac{j\omega L_{min}}{c})}{\Delta L \omega^2 L_{av}}}_{R_1^2(\omega)} \\
 G_{2t}(\omega) &= \underbrace{-\frac{c^2}{\omega^2 L_{av}^2}}_{R_2^1(\omega)} + \underbrace{\frac{j c^3}{2 \Delta L L_{av}^2 \omega^3} (\exp(\frac{2j L_{max} \omega}{c}) - \exp(\frac{2j L_{min} \omega}{c}))}_{R_2^2(\omega)} - \\
 &\quad \underbrace{\frac{2j c^3}{\Delta L L_{av}^2 \omega^3} (\exp(\frac{j L_{max} \omega}{c}) - \exp(\frac{j L_{min} \omega}{c}))}_{R_2^3(\omega)}
 \end{aligned} \tag{6.22}$$

The magnitudes of $G_{1t}(\omega)$ and $G_{2t}(\omega)$, as well as the magnitudes of their decompositions, are represented in Figures 6.14.e and 6.14.f for $L_{av} = 75 \mu m$ and $\Delta L = 10 \mu m$.

$G_{2t}(\omega)$ represents the expected output of a communication channel made of two angled transducers around a plate. It has been compared to the Mason model associated with staircase transducers (50 steps) surrounding a 1-mm-thick aluminum plate in Figure 6.15.

Despite some differences due to the different approximations, the shapes of both curves present large similarities. The function $G_{2t}(\omega)$ will then be used to understand the characteristics of the output signal as well as the limitations associated.

It can be noted that:

$$\begin{aligned} \exp\left(\frac{j\omega L_{max}}{c}\right) - \exp\left(\frac{j\omega L_{min}}{c}\right) &= 2i \exp\left(\frac{j\omega L_{av}}{c}\right) \sin\left(\frac{\omega\Delta L}{2c}\right) \\ \exp\left(\frac{2j\omega L_{max}}{c}\right) - \exp\left(\frac{2j\omega L_{min}}{c}\right) &= 2i \exp\left(\frac{2j\omega L_{av}}{c}\right) \sin\left(\frac{\omega\Delta L}{c}\right) \end{aligned} \quad (6.23)$$

which outline oscillations of periodicity $\omega_o = \frac{2\pi c}{L_{av}}$ (resp. $\frac{\pi c}{L_{av}}$) contained in an envelop of periodicity $\omega_e = \frac{4\pi c}{\Delta L}$ (resp. $\frac{2\pi c}{\Delta L}$). As a consequence, the function $G_{2t}(\omega)$ can be split into three sections:

- $R_2^1(\omega)$ depicts a magnitude drop proportional to $\frac{1}{\omega^2}$ as the frequencies increase, associated with a loss of transmission over a growing numbers of harmonics.
- $R_2^3(\omega)$ depicts primary oscillations of periodicity $\frac{2\pi c}{L_{av}}$ that directly stem from the shape of each transducer and derive from the expression $R_1^2(\omega)$.
- $R_2^2(\omega)$ are higher order variations (periodicity $\frac{\pi c}{L_{av}}$) that originate from the association of both transducers.

The magnitude of both $R_2^2(\omega)$ and $R_2^3(\omega)$ drop as the amplitude of their envelop collapses, which happens when:

$$\omega = \frac{2\pi mc}{\Delta L} \quad (m = 1, 2, 3, \dots) \quad (6.24)$$

Therefore, the center of the targeted bandwidth is obtained by taking $m = 1$ and happens at the frequency f_c :

$$f_c = \frac{c}{\Delta L} \quad (6.25)$$

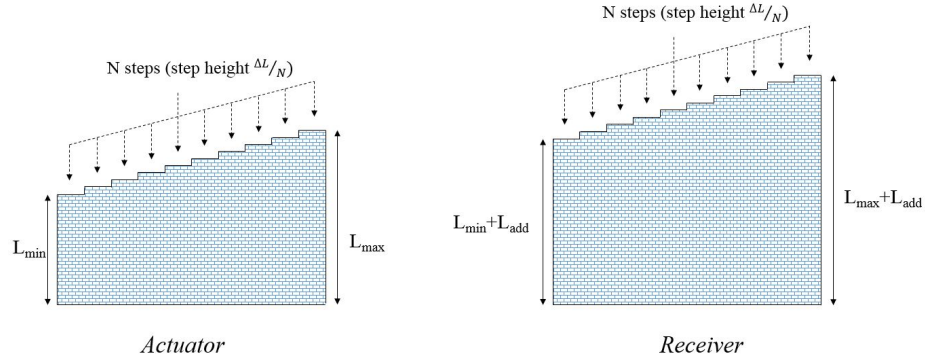


Figure 6.16: Actuator and receiver with a thickness offset L_{add}

6.5 Strategies for bandwidth enhancements

The limitations preventing a flat bandwidth characterized by the amplitude drop $R_2^1(\omega)$ and the fluctuations $R_2^3(\omega)$ are addressed through two distinctive approaches.

6.5.1 Thickness offsetting between the actuator and the receiver

The primary oscillations of periodicity $\frac{2\pi c}{L_{av}}$ were characterized for a single transducer by $R_1^2(\omega)$. By associating a similar actuator and receiver, these variations are added constructively for the combination actuator/receiver as seen in $R_2^3(\omega)$. On the other hand, these oscillations can be added destructively if the characteristics of the actuator and the receiver are in phase opposition.

A different design using an additional thickness L_{add} at the receiver has then been introduced and presented in Figure 6.16. Under this configuration, the design of the actuator remains identical (thickness ranging between L_{min} and L_{max} over N steps) while the thickness of the receiver is increased uniformly by an amount L_{add} (thickness ranging between $L_{min} + L_{add}$ and $L_{max} + L_{add}$ over N steps). The difference between the maximum and minimum thicknesses remains identical and equal to $\Delta L = L_{max} - L_{min}$ for both transducers.

The functions $R_{1_{act}}^2(\omega)$ and $R_{1_{rec}}^2(\omega)$ describing these oscillations for the actuator and

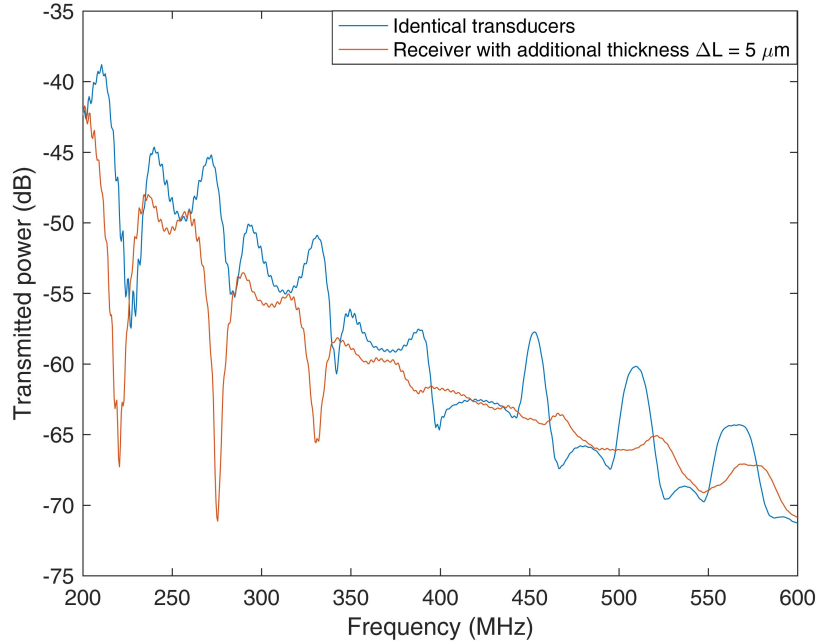


Figure 6.17: Comparison of the transmitted power for a configuration similar staircase actuators and receivers (20 steps, thickness between 70 and 80 μm) and a configuration with a receiver with an additional thickness of 5 μm

the receiver are then given by:

$$R_{1_{act}}^2(\omega) = c^2 \frac{\exp\left(\frac{j\omega L_{max}}{c}\right) - \exp\left(\frac{j\omega L_{min}}{c}\right)}{\Delta L \omega^2 L_{av}} \quad (6.26)$$

$$R_{1_{rec}}^2(\omega) = c^2 \exp\left(\frac{j\omega L_{add}}{c}\right) \frac{\exp\left(\frac{j\omega L_{max}}{c}\right) - \exp\left(\frac{j\omega L_{min}}{c}\right)}{\Delta L \omega^2 (L_{av} + L_{add})}$$

The two functions are characterized by a phase difference of $\exp\left(\frac{j\omega L_{add}}{c}\right)$. They are consequently in phase opposition when:

$$\frac{\omega L_{add}}{c} = \pi \quad (6.27)$$

The objective is to minimize the variations around the frequency f_c described in 6.25. At this pulsation, Equation 6.27 equates to:

$$L_{add} = \frac{\Delta L}{2} \quad (6.28)$$

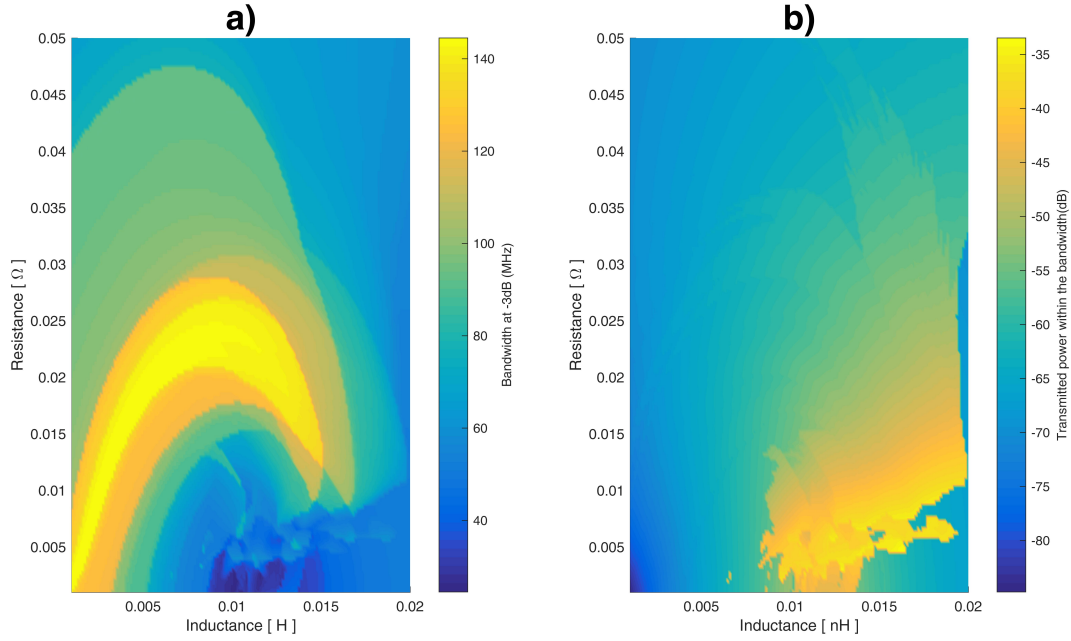


Figure 6.18: Variations of a) the bandwidth at -2dB , b) the transmitted power within the bandwidth, for different values of resistance and inductance in the input circuits

This configuration is outlined in Figure 6.17 where the theoretical outputs (Mason model) for a structure with an identical actuator and receiver has been compared with a structure with an offset thickness $L_{add} = 5\mu m$ at the receiver ($L_{min} = 70\mu m$, $L_{max} = 80\mu m$, $\Delta L = 10\mu m$, and $N = 20$ steps). The fluctuations visible for the configuration with identical transducers have been largely mitigated around the frequency $f_c = \frac{c}{\Delta L} = 430MHz$ with the new design.

6.5.2 Capacitance compensation with electric impedances

The second obstacle that has been addressed is the transmission loss occurring for increasing frequencies, as the resulting negative slope should be compensated in order to obtain a constant transmission over a large bandwidth. This loss is due to the reduction of the electric impedance Z_{trans} associated the capacitance C_0 of the transducers with growing frequencies:

$$Z_{trans} = \frac{1}{jC_0\omega} \quad (6.29)$$

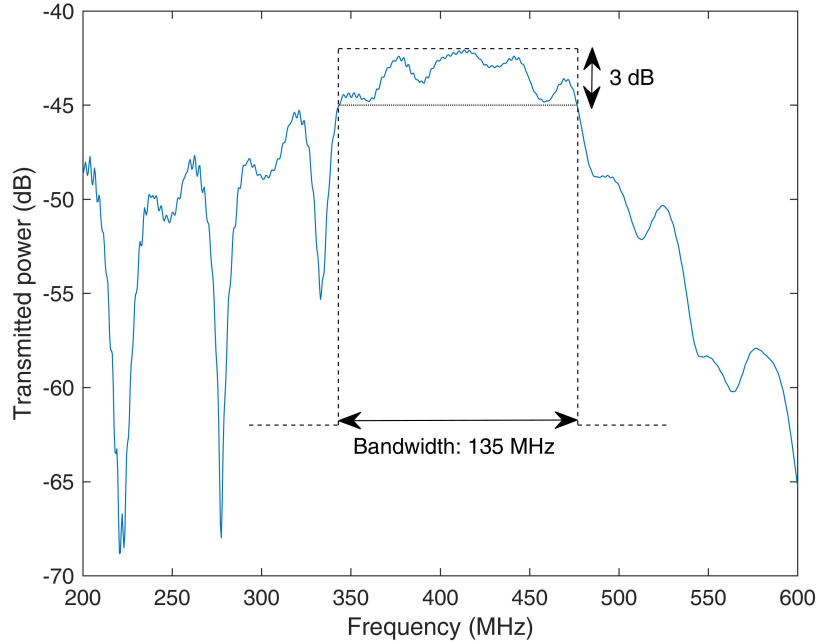


Figure 6.19: Transmitted power for the structure given in Table 6.1

The capacitive impedances can be compensated by resistances/inductances in the circuits connected to the actuator and receiver as shown previously in Figure 4.7. When chosen accordingly, the additional impedances Z_a (in the actuating circuit) and Z_r (in the receiving circuit) can improve the transmission around a given frequency f_{peak} defined by the chosen inductances L :

$$f_{peak} = \frac{1}{2\pi\sqrt{LC_0}} \quad (6.30)$$

Given the similar geometries of the actuator and receiver, both additional impedances Z_a and Z_r will be selected as equal:

$$Z_a = Z_r = R + jL\omega \quad (6.31)$$

The bandwidths at -3 dB obtained for values of R ranging between 0 and 50 $m\Omega$ and values of L ranging between 0 and 0.02 nH have been computed and displayed in a heat map in Figure 6.18.a ($L_{min} = 70\mu m$, $L_{max} = 80\mu m$, $\Delta L = 10\mu m$, $L_{add} = 5\mu m$, 20 steps).

Bandwidths near 140 MHz could be reached for different resistance and inductance values. Besides, the choice of R and L is also led by the intention of improving the magnitude of the transmission within the bandwidth. Figure 6.18.b presents the amplitude of the transmitted power within the bandwidth for the same values of R and L .

The configuration with $L = 0.015nH$ and $R = 13m\Omega$ (transmitted power in Figure 6.19) offers a good compromise between a large bandwidth (135 MHz) and a high transmission within (-45 dB) (structure described in Table 6.1).

Table 6.1: Configuration of the channel with staircase transducers, thickness offsets and electric impedances

	Min. Thickness	Max. Thickness	Material	Resistance	Inductance
Actuator	70 μm	80 μm	PZT-5A	/	/
Receiver	75 μm	85 μm	PZT-5A	/	/
Plate	1 mm		Aluminum	/	/
Actuating circuit	/	/	/	13m Ω	0.015nH
Receiving circuit	/	/	/	13m Ω	0.015nH

6.6 Conclusion

An alternate design has been proposed in this chapter to achieve large bandwidths at -3 dB at high frequencies while working with thick piezoelectric transducers. This new structure has been shaped like a staircase to combine the output of steps of different thicknesses.

The Mason model has been adapted to suit this new configuration and its validity was confirmed through the comparison with Finite Element models. A second simplified analytical model has been derived to produce an explicit expression of the output and provide an insight towards the limitations of such a structure.

These deficiencies have been addressed through two separate approaches altering the thickness of the receiving transducer and adapting the connected electric circuits. Finally, a configuration enabling a bandwidth at -3 dB of 135 MHz has been found.

CHAPTER 7

CONCLUSIONS AND FUTURE WORK

7.1 Summary

This research has been focused on two applications involving piezoelectric transduction for sensing and data transmission purposes.

7.1.1 Acoustic Wave Rosette

A first step in this project has been to manufacture a one-dimensional strain sensor and test it on a loaded beam. The manufacturing process has been decided in conformity with the capabilities of GeorgiaTech cleanroom and a device with an Aluminum Nitride piezoelectric layer upon a flexible glass substrate has been fabricated. With these material characteristics, the device was assumed to provide accurate measurements over a relatively small range of deformations (under $400 \mu\epsilon$) which is consistent with the modest deformations observable on rotorcrafts.

The manufactured device has been characterized by measuring its center frequency at rest and defining the characteristic slope Frequency/Strain under a loaded beam. The quality of the sensor can be evaluated by measuring the slope linearity and its associated R^2 factor. The results have also been compared to theoretical results.

The second step has been to manufacture the two-dimensional Acoustic Wave Rosette and test it. The design has been inspired by a theoretical model and improved by incorporating an analogous actuator in order to target specifically the generation of Rayleigh waves. The manufacturing steps are similar to the previous ones, even if smaller critical distances have made the fabrication more challenging.

The ability of the transducer to filter three different frequencies has been assessed at rest,

before mounting and testing the device on a loaded beam.

7.1.2 Acoustic data transmission through a metallic barrier

The eletro-mechanical behavior of an acoustic channel made of two piezoelectric transducers and different passive layers has been described through an analytical model. It has also been likened with numerical 2D and 3D COMSOL models with finite dimensions in order to show that the boundary effects have a negligible impact on the voltage output out of the anti-resonances. A second validation step has been carried out through experiments. Different experimental results have been obtained from structures with various bonding layers (conductive epoxy, vacuum grease and solders) and positively matched with the expected theoretical outputs.

Different approaches have then been presented to mitigate the variations of the transmitted power over large bandwidths. Epoxy has first been introduced to trap the waves at the surface of the transducers. Its damping effect has been theoretically improved by loading it with tungsten particles, but was not sufficient to decrease the amplitude variations to the targeted value of 2 dB. Additional electroplated layers have been added in order to bring resonances closer to each other and reduce the amplitude variations between them, while electric impedances have been added to the circuits connected to the actuator and the receiver as a damping strategy. At the end, two interesting configurations mixing these three approaches (epoxy backing, electroplated layers and electric impedances) have been derived and enabled bandwidth at -2 dB around 2 MHz (for a carrier frequency of 4 MHz).

A different design shaped like a staircase has been introduced and developed for high-frequencies applications. The advantage of such a structure lies in its capability to define bandwidths with limited amplitude variations that overlap the antiresonance characteristic of each step, therefore enabling to use thick transducers with lower capacitances. Its behavior has been studied through analytical models and two approaches have been introduced to limit the transmission variations within the targeted bandwidth. Finally, a design enabling

a bandwidth at -3 dB of 135 MHz with transducers thicker than $70 \mu m$ has been presented.

7.2 Contributions

7.2.1 Acoustic Wave Rosette

- Definition of the theoretical relation between the applied strains (ε_{xx} , ε_{yy} , ε_{xy}) and the three frequencies filtered by the AWR for a given electrode design
- Manufacturing of a 1D acoustic strain sensor by following microfabrication methods
- Experimental assessment of its 1D strain-sensing capabilities and definition of its characteristic slope Frequency/Strain.
- Manufacturing of a 2D acoustic strain sensor following the AWR design
- Experimental assessment of its capability to filter three distinct frequencies
- Experimental assessment of its 2D strain-sensing capabilities on a loaded beam

7.2.2 Acoustic data transmission through a metallic barrier

- Definition of a reliable one-dimensional analytical model in the frequency domain describing the electro-mechanical behavior of an acoustic data transmission channel, that could positively compare with Finite Elements results
- Experimental validation of the analytical model for structures with various bonding layers
- Definition of different approaches involving backing layers, additional electroplated layers and electric impedances in the circuits connected to the actuator and the receiver, with the objective of limiting the amplitude variations over large bandwidths at low frequencies (< 10 MHz)

- Introduction of staircase-shaped transducers limiting the amplitude variations over large bandwidths for high-frequencies applications (> 100 MHz).

7.3 Future work

7.3.1 Acoustic Wave Rosette

- Theoretical work: The expressions relating the the applied strains ε_{xx} , ε_{yy} and ε_{xy} to the frequency shifts of the three filtered frequencies have been derived in Chapter 2. However, these relations also involve the planar stresses σ_{xx} , σ_{yy} and σ_{xy} , as well as the strain ε_{zz} , therefore making the reciprocal relation more complicated. A further theoretical step then consists in deriving the analytical expression relating the frequency shifts to the applied strains.
- Experimental work: Other strain measurements need to be carried out for more complicated strain states, especially involving shear strains.

7.3.2 Acoustic data transmission through a metallic barrier

- Theoretical work: The design made of staircase-shaped transducers needs to be expanded for low-frequencies (< 10 MHz carrier frequencies). Indeed by combining transducers of very different thicknesses, it should be possible to associate bandwidths centered over different carrier frequencies and therefore extend the possible bandwidths at -2 dB over larger frequency spans.
- Experimental work: The different approaches intending to reduce the amplitude variations at low frequencies (< 10 MHz) need to be validated through experiments. This step involves both deposition stages (electroplated layers, backing layers) as well as the implementation of the appropriate electric circuits. For high frequencies applications (> 100 MHz), the staircase transducers introduced in Chapter 6 need to be manufactured and their wideband capacities need to be tested.

REFERENCES

- [1] B. Drafts, “Acoustic wave technology sensors,” *IEEE Transactions on Microwave Theory and Techniques*, vol. 49, no. 4, pp. 795–802, 2001.
- [2] S. Martin, G. Frye, and K. Wessendorf, “Sensing liquid properties with thickness-shear mode resonators,” *Sensors and Actuators A: Physical*, vol. 44, no. 3, pp. 209–218, 1994.
- [3] S. J. Martin, G. C. Frye, J. J. Spates, and M. A. Butler, “Gas sensing with acoustic devices,” in *1996 IEEE Ultrasonics Symposium. Proceedings*, vol. 1, 1996, 423–434 vol.1.
- [4] M. G. Schweyer, J. A. Hilton, J. E. Munson, J. C. Andle, J. M. Hammond, and R. M. Lec, “A novel monolithic piezoelectric sensor,” in *Proceedings of International Frequency Control Symposium*, 1997, pp. 32–40.
- [5] H. Fritze, “High temperature bulk acoustic wave sensors,” *Measurement Science and Technology*, vol. 22, p. 012 002, Dec. 2010.
- [6] T. Venkatesan and H. Pandya, “Surface acoustic wave devices and sensors -a short review on design and modelling by impulse response,” *Journal of Environmental Nanotechnology*, vol. 2, pp. 81–90, Sep. 2013.
- [7] L. Rayleigh, “On waves propagated along the plane surface of an elastic solid,” *Proceedings of the London Mathematical Society*, vol. s1-17, no. 1, pp. 4–11, 1885. eprint: <https://londmathsoc.onlinelibrary.wiley.com/doi/pdf/10.1112/plms/s1-17.1.4>.
- [8] R. M. White and F. W. Voltmer, “Direct piezoelectric coupling to surface elastic waves,” *Applied Physics Letters*, vol. 7, no. 12, pp. 314–316, 1965. eprint: <https://doi.org/10.1063/1.1754276>.
- [9] A. V. Mamishev, K. Sundara-Rajan, Fumin Yang, Yanqing Du, and M. Zahn, “Interdigital sensors and transducers,” *Proceedings of the IEEE*, vol. 92, no. 5, pp. 808–845, 2004.
- [10] N. Saldanha and D. C. Malocha, “Pseudo-orthogonal frequency coded wireless saw rfid temperature sensor tags,” *IEEE Transactions on Ultrasonics, Ferroelectrics, and Frequency Control*, vol. 59, no. 8, pp. 1750–1758, 2012.

- [11] K. J. Singh, O. Elmazria, F. Sarry, P. Nicolay, K. Ghoumid, B. Belgacem, D. Mercier, and J. Bounouar, "Enhanced sensitivity of saw-based pirani vacuum pressure sensor," *IEEE Sensors Journal*, vol. 11, no. 6, pp. 1458–1464, 2011.
- [12] W.-B. Wang, H. Gu, X.-L. He, W.-P. Xuan, J.-K. Chen, X.-Z. Wang, and J.-K. Luo, "Transparent ZnO/glass surface acoustic wave based high performance ultraviolet light sensors," *Chinese Physics B*, vol. 24, no. 5, p. 057 701, 2015.
- [13] R. Kshetrimayum, R. D. S. Yadava, and R. P. Tandon, "Mass sensitivity analysis and designing of surface acoustic wave resonators for chemical sensors," *Measurement Science and Technology*, vol. 20, no. 5, p. 055 201, 2009.
- [14] Y. Fan, P. Kong, H. Qi, H. Liu, and X. Ji, "A surface acoustic wave response detection method for passive wireless torque sensor," *AIP Advances*, vol. 8, no. 1, p. 015 321, 2018. eprint: <https://doi.org/10.1063/1.5003178>.
- [15] L. Shu, X. Wang, L. Li, D. Yan, L. Peng, L. Fan, and W. Wu, "The investigation of integrated saw strain sensor based on aln/tc4 structure," *Sensors and Actuators A: Physical*, vol. 293, pp. 14 –20, 2019.
- [16] P. Nicolay, H. Chambon, G. Bruckner, C. Gruber, S. Ballandras, E. Courjon, and M. Stadler, "A In/si-based saw pressure sensor," *Sensors*, vol. 18, p. 3482, Oct. 2018.
- [17] Z. Wang, C. Wang, and L. Liu, "Design and analysis of a pzt-based micromachined acoustic sensor with increased sensitivity," *IEEE transactions on ultrasonics, ferroelectrics, and frequency control*, vol. 52, pp. 1840–50, Nov. 2005.
- [18] S. C. Moulzolf, R. Behanan, R. J. Lad, and M. P. da Cunha, "Langasite saw pressure sensor for harsh environments," in *2012 IEEE International Ultrasonics Symposium*, 2012, pp. 1224–1227.
- [19] R. Stoney, D. Geraghty, and G. E. O'Donnell, "Characterization of differentially measured strain using passive wireless surface acoustic wave (saw) strain sensors," *IEEE Sensors Journal*, vol. 14, no. 3, pp. 722–728, 2014.
- [20] Q. Li, J. Liu, B. Yang, L. Lu, Z. Yi, Y. Tian, and J. Liu, "Highly sensitive surface acoustic wave flexible strain sensor," *IEEE Electron Device Letters*, vol. 40, no. 6, pp. 961–964, 2019.
- [21] N. V. Ramachandran, "Development to a flexible surface acoustic wave sensor for strain sensing," 2018.
- [22] J. Chen, X. He, W. Wang, X. Peng, J. Zhou, X.-z. Wang, S. Dong, S. Garner, and P. Cimo, "Bendable transparent zno thin film surface acoustic wave strain sensors on ultra-thin flexible glass substrates," *J. Mater. Chem. C*, vol. 2, Aug. 2014.

- [23] E. Belknap, “Mechanical characterization of saw-based sensors for wireless high temperature strain measurements,” PhD thesis, Ohio State University, 2011.
- [24] W. Wilson and G. ATKINSON, “Characterization of langasite saw devices to determine the temperature and strain coefficients of velocity,” *Sensors and Transducers*, vol. 162, pp. 21–28, Jan. 2014.
- [25] L. Kollar and R. Van Steenkiste, “Calculation of the stresses and strains in embedded fiber optic sensors,” *Journal of Composite Materials*, vol. 32, no. 18, pp. 1647–1679, Jan. 1998.
- [26] C. Hautamaki, S. Zurn, S. C. Mantell, and D. L. Polla, “Experimental evaluation of mems strain sensors embedded in composites,” *Journal of Microelectromechanical Systems*, vol. 8, no. 3, pp. 272–279, 1999.
- [27] W. C. Wilson, D. C. Malocha, N. Kozlovski, D. R. Gallagher, B. Fisher, J. Pavlina, N. Saldanha, D. Puccio, and G. M. Atkinson, “Orthogonal frequency coded saw sensors for aerospace shm applications,” *IEEE Sensors Journal*, vol. 9, no. 11, pp. 1546–1556, 2009.
- [28] M Perry, I McKeeman, M Saafi, and P Niewczas, “Wireless surface acoustic wave sensors for displacement and crack monitoring in concrete structures,” *Smart Materials and Structures*, vol. 25, no. 3, p. 035 035, 2016.
- [29] L. Shu, B. Peng, Z. Yang, R. Wang, S. Deng, and X. Liu, “High-temperature saw wireless strain sensor with langasite,” *Sensors*, vol. 15, pp. 28 531–28 542, Nov. 2015.
- [30] Z. Bao, M. Hara, and H. Kuwano, “Highly sensitive strain sensors using surface acoustic wave on aluminum nitride thin film for wireless sensor networks,” in *2015 Transducers - 2015 18th International Conference on Solid-State Sensors, Actuators and Microsystems (TRANSDUCERS)*, 2015, pp. 1239–1242.
- [31] M. Carrara and M. Ruzzene, “Fourier-based design of acoustic strain rosettes,” vol. 9061, Mar. 2014.
- [32] P. Myler and L. M. Wyatt, “8 - mechanics of solids,” in *Mechanical Engineer’s Reference Book (Twelfth Edition)*, E. H. Smith, Ed., Twelfth Edition, Butterworth-Heinemann, 1994, pp. 8–1 –8–42, ISBN: 978-0-7506-1195-4.
- [33] *Optimum Array Processing*. John Wiley & Sons, 2004.
- [34] D. Kim and M. Philen, “On the beamsteering characteristics of mfc phased arrays for structural health monitoring,” Apr. 2008, ISBN: 978-1-60086-993-8.

- [35] M. G. Holland and L. T. Claiborne, “Practical surface acoustic wave devices,” *Proceedings of the IEEE*, vol. 62, no. 5, pp. 582–611, 1974.
- [36] H. Yatsuda, “Design techniques for saw filters using slanted finger interdigital transducers,” *IEEE Transactions on Ultrasonics, Ferroelectrics, and Frequency Control*, vol. 44, no. 2, pp. 453–459, 1997.
- [37] V. Laude, D. Gérard, N. Khelifaoui, C. Jerez-Hanckes, S. Benchabane, and A. Khelif, “Subwavelength focusing of surface acoustic waves generated by an annular interdigital transducer,” *Applied Physics Letters*, vol. 92, p. 094 104, Mar. 2008.
- [38] Shyh-Jong Chung, Ming-yi Li, S. Kanamaluru, and Kai Chang, “Meander-image-line-feed microstrip antenna array for frequency-swept beam steering,” in *IEEE Antennas and Propagation Society International Symposium. 1996 Digest*, vol. 2, 1996, 1254–1257 vol.2.
- [39] M. Senesi and M. Ruzzene, “A frequency selective acoustic transducer for directional lamb wave sensing,” *The Journal of the Acoustical Society of America*, vol. 130, no. 4, pp. 1899–1907, 2011. eprint: <https://doi.org/10.1121/1.3626165>.
- [40] E. Baravelli and L. D. Marchi, “Experimental demonstration of spiral frequency-steerable acoustic sensors,” *AIP Conference Proceedings*, vol. 1433, no. 1, pp. 129–132, 2012. eprint: <https://aip.scitation.org/doi/pdf/10.1063/1.3703154>.
- [41] M. Carrara and M. Ruzzene, “Frequency wavenumber design of spiral macro fiber composite directional transducers,” in *Smart Structures*, 2015.
- [42] L. Huang, A. P. Hu, A. Swain, S. Kim, and Y. Ren, “An overview of capacitively coupled power transfer — a new contactless power transfer solution,” in *2013 IEEE 8th Conference on Industrial Electronics and Applications (ICIEA)*, 2013, pp. 461–465.
- [43] D. J. Graham, J. A. Neasham, and B. S. Sharif, “Investigation of methods for data communication and power delivery through metals,” *IEEE Transactions on Industrial Electronics*, vol. 58, no. 10, pp. 4972–4980, 2011.
- [44] H. Zangl, A. Fuchs, T. Bretterklieber, M. J. Moser, and G. Holler, “Wireless communication and power supply strategy for sensor applications within closed metal walls,” *IEEE Transactions on Instrumentation and Measurement*, vol. 59, no. 6, pp. 1686–1692, 2010.

- [45] M. Yamakawa, Y. Mizuno, J. Ishida, and H. Koizumi, “Wireless power transmission into a space enclosed by metal walls using magnetic resonance coupling,” *Wireless Engineering and Technology*, vol. 05, pp. 19–24, Jan. 2014.
- [46] D. Graham, J. Neasham, and B. Sharif, “High bit rate communication through metallic structures using electromagnetic acoustic transducers,” Jun. 2009, pp. 1–6.
- [47] V. Petrov, “Modeling of magnetoelectric interaction in magnetostrictive-piezoelectric composites,” *Advances in Condensed Matter Physics*, vol. 2012, Mar. 2012.
- [48] Y. Hu, X. Zhang, J. Yang, and Q. Jiang, “Transmitting electric energy through a metal wall by acoustic waves using piezoelectric transducers,” *IEEE Transactions on Ultrasonics, Ferroelectrics, and Frequency Control*, vol. 50, no. 7, pp. 773–781, 2003.
- [49] D. J. Connor, G. F. Cummings, and M. J. Star, *Acoustic transformer with non-piezoelectric core*, US Patent, US5594705A, Jan. 1997.
- [50] H. A. Sodano, D. J. Inman, and G. Park, “Generation and storage of electricity from power harvesting devices,” *Journal of Intelligent Material Systems and Structures*, vol. 16, pp. 67–75, 2005.
- [51] Z. Yang, J. Yang, and Y. Hu, “Energy trapping in power transmission through an elastic plate by finite piezoelectric transducers,” *IEEE Transactions on Ultrasonics, Ferroelectrics, and Frequency Control*, vol. 55, no. 11, pp. 2493–2501, 2008.
- [52] H. Hu, Y. Hu, and X. Chen, “Wireless energy transmission through a sealed wall using the acoustic-electric interaction of piezoelectric ceramics,” vol. 7493, Jul. 2009.
- [53] D. A. Shoudy, G. J. Saulnier, H. A. Scarton, P. K. Das, S. Roa-Prada, J. D. Ashdown, and A. J. Gavens, “P3f-5 an ultrasonic through-wall communication system with power harvesting,” in *2007 IEEE Ultrasonics Symposium Proceedings*, 2007, pp. 1848–1853.
- [54] T. Murphy, “Ultrasonic digital communication system for a steel wall multipath channel: Methods and results,” PhD thesis, Rensselaer Polytechnic Institute, 2006.
- [55] M. Kluge, T. Becker, J. Schalk, and T. Otterpohl, “Remote acoustic powering and data transmission for sensors inside of conductive envelopes,” in *SENSORS, 2008 IEEE*, 2008, pp. 41–44.
- [56] R. Primerano, M. Kam, and K. Dandekar, “High bit rate ultrasonic communication through metal channels,” in *2009 43rd Annual Conference on Information Sciences and Systems*, 2009, pp. 902–906.

- [57] K. Wanuga, M. Bielinski, R. Primerano, M. Kam, and K. R. Dandekar, "High-data-rate ultrasonic through-metal communication," *IEEE Transactions on Ultrasonics, Ferroelectrics, and Frequency Control*, vol. 59, no. 9, pp. 2051–2053, 2012.
- [58] B. H. DingXin Yang and D. Tian, "The modeling framework for through-metal-wall ultrasonic power transmission channels based on piezoelectric transducers," *Mathematical Problems in Engineering*, vol. 2019, Jun. 2019.
- [59] T. J. Lawry, K. R. Wilt, H. A. Scarton, and G. J. Saulnier, "Analytical modeling of a sandwiched plate piezoelectric transformer-based acoustic-electric transmission channel," *IEEE Transactions on Ultrasonics, Ferroelectrics, and Frequency Control*, vol. 59, no. 11, pp. 2476–2486, 2012.
- [60] K. Wilt, T. Lawry, H. Scarton, S. Roa-Prada, G. Saulnier, J. Ashdown, P. Das, and J. Pinezich, "Mechanical design implications on power transfer through thick metallic barriers using piezoelectric transducers," vol. 13, Jan. 2010.
- [61] K. Wilt, H. Scarton, S. Roa-Prada, G. Saulnier, J. Ashdown, T. Lawry, P. Das, and A. Gavens, "Finite element modeling and simulation of a two-transducer through-wall ultrasonic communication system," vol. 15, Jan. 2009.
- [62] R. Primerano, K. Wanuga, J. Dorn, M. Kam, and K. Dandekar, "Echo-cancellation for ultrasonic data transmission through a metal channel," in *2007 41st Annual Conference on Information Sciences and Systems*, 2007, pp. 841–845.
- [63] M. Bielinski, K. Wanuga, R. Primerano, M. Kam, and K. R. Dandekar, "Application of adaptive ofdm bit loading for high data rate through-metal communication," in *2011 IEEE Global Telecommunications Conference - GLOBECOM 2011*, 2011, pp. 1–5.
- [64] J. Chen, H. Guo, X. He, W. Wang, X. Peng, H. Jin, S. Dong, X. Wang, Y. Xu, S. Lin, and S. Garner, "Development of flexible zno thin film surface acoustic wave strain sensors on ultrathin glass substrates," *Journal of Micromechanics and Microengineering*, vol. 25, p. 115 005, Nov. 2015.
- [65] A. I. Nalamwar and M. Epstein, "Effects of applied strain in zno thin-film saw devices," *IEEE Transactions on Sonics and Ultrasonics*, vol. 23, no. 3, pp. 144–147, 1976.
- [66] A. L. Nalamwar and M. Epstein, "Surface acoustic waves in strained media," *Journal of Applied Physics*, vol. 47, no. 1, pp. 43–48, 1976. eprint: <https://doi.org/10.1063/1.322293>.
- [67] H. Nakahata, A. Hachigo, K. Higaki, S. Fujii, S. Shikata, and N. Fujimori, "Theoretical study on saw characteristics of layered structures including a diamond layer,"

IEEE Transactions on Ultrasonics, Ferroelectrics, and Frequency Control, vol. 42, no. 3, pp. 362–375, 1995.

- [68] R. Cirelli, G. Watson, and O. Nalamasu, “Optical lithography,” in *Encyclopedia of Materials: Science and Technology*, K. J. Buschow, R. W. Cahn, M. C. Flemings, B. Ilshner, E. J. Kramer, S. Mahajan, and P. Veysière, Eds., Oxford: Elsevier, 2001, pp. 6441–6448, ISBN: 978-0-08-043152-9.
- [69] A. Iqbal and F. Mohd-Yasin, “Reactive sputtering of aluminum nitride (002) thin films for piezoelectric applications: A review,” *Sensors*, vol. 18, no. 6, 2018.
- [70] *Microposit s1800 series photoresists*, datasheet, Rohm and Haas, 2006.
- [71] *Microposit mf-300 series developer*, datasheet, Rohm and Haas, 2008.
- [72] L. Rabiner, R. Schafer, and C. Rader, “The chirp z-transform algorithm,” *IEEE Transactions on Audio and Electroacoustics*, vol. 17, no. 2, pp. 86–92, 1969.
- [73] A. Singer, M. Oelze, and A. Podkowa, “Mbps experimental acoustic through-tissue communications: Meat-comms,” Jul. 2016, pp. 1–4.
- [74] L. Cimini, “Analysis and simulation of a digital mobile channel using orthogonal frequency division multiplexing,” *IEEE Transactions on Communications*, vol. 33, no. 7, pp. 665–675, 1985.
- [75] M. D. C. Eames and J. A. Hossack, “Filled and unfilled temperature-dependent epoxy resin blends for lossy transducer substrates,” *IEEE Transactions on Ultrasonics, Ferroelectrics, and Frequency Control*, vol. 56, no. 4, pp. 864–869, 2009.
- [76] H. Wang, T. Ritter, W. Cao, and K. Shung, “Passive materials for high-frequency ultrasound transducers,” *Proc SPIE*, vol. 3664, pp. 35–42, Jun. 1999.